

**Applying Hyperspectral Remote Sensing Techniques for the Detection of Hydrothermal
Alteration Zones and Gossans in Northern Canada**

by

Kati Susanna Laakso

A thesis submitted in partial fulfillment of the requirements for the degree of

Doctor of Philosophy

Department of Earth and Atmospheric Sciences
University of Alberta

© Kati Laakso, 2015

ABSTRACT

This thesis is composed of three chapters assessing the following specific goals: 1) To evaluate the potential of airborne hyperspectral remote sensing data and techniques to delineate the hydrothermal alteration zones of volcanogenic massive sulfide (VMS) systems in areas of abundant lichens on rock outcrops; 2) To assess the potential of hyperspectral remote sensing data and techniques to unmask the hydrothermal alteration intensity variation of VMS systems; 3) To investigate the effect of the rock substrates and lichens on the spectral properties of gossans in the visible-near infrared wavelength region (VNIR, 400-1300 nm); 4) To evaluate the potential of hyperspectral remote sensing data to unmask the mineralogical properties of the rock substrates of gossans in the short-wave infrared wavelength region (SWIR, 1300-2500 nm). First, in Chapter two airborne and ground hyperspectral data from an economically important Izok Lake VMS deposit (Nunavut, northern Canada) are used to test the ability to unmask hydrothermal alteration zones by remote sensing in an area of abundant low-growing ground cover. The results suggest that these zones can be delineated by hyperspectral airborne remote sensing means even if the dense ground cover necessitates the masking out of many pixels in the scene. In Chapter three, the applicability of hyperspectral ground and laboratory remote sensing data are used to estimate the hydrothermal alteration intensity variation of the Izok Lake deposit. The results suggest that there are statistically significant relationships between the spectral properties of the phyllosilicate minerals (white micas and biotite/chlorite) and alteration indices (the Ishikawa and chlorite-carbonate-pyrite index). These relationships can be exploited to investigate the large scale hydrothermal intensity variation of VMS deposits. Furthermore, the

investigations of Chapters two and three suggest that biotite/chlorite can provide a stronger vector toward the massive sulfide lenses of the Izok Lake deposit than white micas. Finally, Chapter four discusses the optical thickness properties of gossans, and the effects of lichens and rock substrates on their spectral properties. These phenomena were investigated by means of laboratory and airborne hyperspectral remote sensing data from the Cape Smith Belt in northern Canada. The results indicate that some gossans are optically thin, enabling the transmission of light into the rock substrate. The implications are twofold. First, the rock substrates can influence the spectral shape of the iron oxide minerals, the main constituents of gossans, in the VNIR wavelength region. Second, the mineralogical properties of the host rock substrates of optically thin gossans can be detected by remote sensing means. This finding can be used for mineral exploration in areas of a known link between specific rock types and ore deposits. Also, our investigation in the Cape Smith Belt suggests that spectral mixing between gossans and lichens can influence the spectral shape of gossans in the VNIR wavelength region. As in case of spectral mixing between gossans and their rock substrates, understanding the effects of such mixing is important because it can affect the ability to characterize the mineralogical properties of gossans by remote sensing. My thesis addresses issues that are critical to the advancement of hyperspectral remote sensing techniques for mineral exploration in the subarctic and Arctic. The investigations discussed in my thesis contribute to the understanding of the applicability of hyperspectral airborne, ground and laboratory remote sensing datasets and techniques to unmask potential ore deposits in northern areas.

ACKNOWLEDGEMENTS

I am greatly indebted to my supervisor, Dr. Benoit Rivard, for giving me an opportunity to learn from his work and experience. His insights into geological hyperspectral remote sensing phenomena have been my constant source of inspiration during the years I have spent working with him.

I would also like to express my deepest gratitude to my committee advisors Dr. Arturo Sánchez-Azofeifa, Dr. John Waldron and Dr. Christopher Herd for their scientific advice.

My work could not have been completed without the financial support of the University of Alberta (2010-2013), Natural Resources Canada (Research Affiliate and the Targeted Geoscience Initiative 4 Programs of the Earth Sciences Sector of Natural Resources Canada, 2011-2014) and the Kone Foundation (2010-2011).

I would also like to thank my co-worker Dr. Jan Peter from Natural Resources Canada for his invaluable guidance on topics related to volcanogenic massive sulfide deposits. Advice given by Dr. Jilu Feng (Department of Earth and Atmospheric Sciences, University of Alberta) was indispensable during the early stages of my PhD. It has also been my pleasure to work with Dr. H. Peter White, Mr. Matthew Maloley and Dr. Jeff Harris from Natural Resources Canada, and Dr. Derek Rogge from German Aerospace Center (DLR). I would like to take the opportunity to thank Minerals and Metals Group Ltd. (MMG) for their field support in 2013, and for their generous sharing of knowledge and data sets. My special thanks go to Ms. Kim Bailey and Ms. Trish Toole from MMG for all their help.

I owe a lot to my former and current colleagues at the Earth Observation Systems Laboratory (EOSL) of the Department of Earth and Atmospheric Sciences. In particular, I

would like to thank Mei Mei Chong, Leila Taheriazad, Chang-Uk Hyun, Sandra Duran, Michelle Tappert, Tali Neta, Iman Entezari, Dominica Harrison, Kayla Stan, Sofia Calvo and Sarah Freitas Magalhães for their support and camaraderie.

I would not have finished my thesis without the support of all my family members and friends.

TABLE OF CONTENTS

CHAPTER 1 - Introduction.....	1
1.1 MOTIVATION FOR RESEARCH.....	1
1.2 GOALS OF THE THESIS AND TESTED HYPOTHESIS	4
1.3 ORGANIZATION OF THE THESIS	7
LITERATURE CITED	10
CHAPTER 2 - Application of airborne, laboratory and field hyperspectral methods to mineral exploration in the Canadian Arctic: recognition and characterization of volcanogenic massive sulfide-associated hydrothermal alteration in the Izok Lake deposit area, Nunavut, Canada.....	16
2.1 INTRODUCTION.....	16
2.2 STUDY AREA.....	19
2.3 SPECTRAL DATASETS	20
2.3.1 Ground site selection and spectral measurements.....	20
2.3.2 Sample suite and laboratory spectral measurements.....	22
2.3.3 Airborne spectral imaging.....	23
2.3.4 Petrography and mineral chemistry.....	23
2.4 SPECTRAL ANALYSIS METHODOLOGIES.....	25
2.4.1 Ground and hand sample spectral processing	25
2.4.2 Airborne spectrometric data processing.....	26
2.5 RESULTS.....	30
2.5.1 Mineralogy	30
2.5.2 Mineral chemistry	30
2.5.3 Ground spectrometry.....	31

2.5.3.1 <i>Frequency and spatial distribution of the Fe-OH absorption feature wavelength positions</i>	31
2.5.3.2 <i>Frequency and spatial distribution of the Al-OH absorption feature wavelength positions</i>	32
2.5.4 Airborne spectrometry.....	34
2.5.4.1 <i>Frequency and spatial distribution of the Al-OH absorption feature wavelength positions</i>	34
2.6 DISCUSSION	35
2.6.1 Validation of the spectrometric datasets	35
2.6.2 Absorption feature wavelength positions of the white micas and chlorite group minerals	37
2.6.3 Absorption feature wavelength trends in the ground spectra.....	37
2.6.4 Absorption feature wavelength trends in the airborne spectrometry	38
2.6.5 Implications for the interpretation of the deposit fluid flow paths.....	41
2.7 SUMMARY AND CONCLUSIONS.....	42
LITERATURE CITED	59
CHAPTER 3 - Short-wave infrared (SWIR) spectral and geochemical characteristics of hydrothermal alteration at the Archean Izok Lake Zn-Cu-Pb-Ag volcanogenic massive sulfide deposit, Nunavut, Canada: application in exploration target vectoring.....	
3.1 INTRODUCTION.....	66
3.2 STUDY AREA.....	70
3.3 SAMPLING AND METHODS	71

3.3.1 Ground spectra site selection and measurement	71
3.3.2 Drill core sampling and laboratory spectral measurements	72
3.3.3 Bulk geochemical analytical techniques	73
3.3.4 Mineralogy and mineral chemistry	75
3.3.5 Lithogeochemical data treatment	75
3.3.6 Mineralogy and mineral chemistry	78
3.4 RESULTS.....	79
3.4.1 Frequency distribution of Al-OH and Fe-OH absorption features.....	79
3.4.2 Evaluation of geochemical indicators of alteration intensity of the drillcore dataset ...	80
3.4.3 Relationships between drill core spectral and geochemical indicators	81
3.4.4 Relationships between ground spectral and geochemical indicators	82
3.4.5 Regional map patterns of the Al-OH and Fe-OH absorption feature positions	83
3.5 DISCUSSION	84
3.5.1 Spectral characteristics of white micas and biotite/chlorite	84
3.5.2 Correlations between the spectral absorption features and the bulk rock compositions.....	86
3.5.3 Implications of the spectral features for deposit genesis.....	89
3.6 SUMMARY AND CONCLUSIONS.....	90
LITERATURE CITED	102
CHAPTER 4 - Enhanced detection of gossans using hyperspectral data: example from the Cape Smith Belt of northern Quebec, Canada.....	110
4.1 INTRODUCTION.....	110
4.2 STUDY AREA.....	113

4.3 DATASETS AND SPECTRAL MEASUREMENTS	114
4.3.1 Sample suite and site selection.....	114
4.3.2 X-ray diffraction.....	114
4.3.3 Laboratory spectral measurements.....	115
4.3.3.1 <i>Measurements with an ASD FieldSpec[®] 3 spectroradiometer</i>	115
4.3.3.2 <i>Measurements with a SisuRock imager</i>	116
4.3.4 Airborne spectral imaging.....	116
4.4 SPECTRAL ANALYSIS METHODOLOGY	117
4.4.1 Processing of the ASD spectrometry	119
4.4.2 Processing of the laboratory spectrometry	119
4.4.3 Processing of the airborne spectrometry	121
4.5 RESULTS.....	123
4.5.1 Ferric absorption for the weathered surfaces of the gossan samples	123
4.5.2 Synthetic spectral mixtures of gossans and non-gossans.....	124
4.5.3 Synthetic spectral mixtures of gossans and lichens	125
4.5.4 Airborne spectrometry.....	126
4.5.4.1 <i>Comparison of gossan image endmembers with laboratory spectra</i>	126
4.5.4.2 <i>Map distribution of gossan image endmembers</i>	127
4.6 DISCUSSION	128
4.6.1 Pitfalls in the use of iron feature characteristics for the spectral identification of gossans	128

4.6.2 Merits of hyperspectral imaging for gossan detection and value for exploration	128
4.7 CONCLUSIONS	129
LITERATURE CITED	144
CHAPTER 5 – Discussion, summary of limitations, future research and conclusions.....	150
5.1 DISCUSSION	150
5.2 SUMMARY OF LIMITATIONS TO RESEARCH PROJECTS	151
5.2.1 Data availability	151
5.2.2 Instrumental limitations.....	151
5.2.3 Logistical aspects of field sampling.....	153
5.3 CONTRIBUTIONS AND IMPLICATIONS FOR FUTURE RESEARCH.....	153
5.3.1 Chapter Two: Application of airborne, laboratory and field hyperspectral methods to mineral exploration in the Canadian Arctic: recognition and characterization of volcanogenic massive sulfide-associated hydrothermal alteration in the Izok Lake deposit area, Nunavut, Canada	154
5.3.2 Chapter Three: Short-wave infrared (SWIR) spectral and geochemical characteristics of hydrothermal alteration zones at the Archean Izok Lake Zn-Cu-Pb-Ag volcanogenic massive sulfide deposit, Nunavut, Canada: application in exploration target vectoring	156
5.3.3 Chapter Four: Enhanced detection of gossans using hyperspectral data: example from the Cape Smith Belt of northern Quebec, Canada	158
5.4. CONCLUSIONS	160
LITERATURE CITED	162
LITERATURE CITED (THESIS)	165
APPENDIX A.....	186

LIST OF TABLES

TABLE 2.1. Thin section samples, their mineralogy and the presence of the Al-OH and Fe-OH absorption features	44
TABLE 2.2. Average compositions of the samples per mineral and the average Al-OH and Fe-OH absorption feature wavelength positions; <i>n</i> =number of analyses per sample; biot.=biotite, chl.=chlorite.....	45
TABLE 3.1. Summary statistics of the Al-OH and Fe-OH absorption features of the ground and drill core spectra.....	92
TABLE 4.1. Minerals identified by XRD (gossan sample set). Columns: A=Amphibole group; B=Carbonate group; C=Chlorite group; D=Cordierite group; E=Epidote group; F=Feldspar group; G=Iron oxide group; H=Mica group; I=Other phyllosilicates; J=Pyroxene group; K=Quartz; L=Serpentine group; M=Sulfide group; Abbreviations: Sed.=sedimentary, Ultram.=ultramafic. Amphibole group minerals: actinolite, fluoromagnesiorichterite and magnesiohornblende. Carbonate group minerals: calcite and dolomite. Chlorite group minerals: clinocllore and chamosite. Epidote group minerals: epidote and clinozoisite. Feldspar group minerals: albite, anorthite, orthoclase and microcline. Iron oxide group minerals: hematite, goethite, lepidocrocite and magnetite. Mica group minerals: muscovite, phengite, phlogopite and margarite. Other phyllosilicates: vermiculite, minnesotaite and stilpnomelane. Pyroxene group minerals: enstatite, diopside. Serpentine group minerals: antigorite, cronstedtite and tremolite. Sulfide group minerals: pyrite, pyrrhotite and marcasite.....	130
TABLE 4.2. The average band position (in nm) of the 0-10 % and 10-20 % band depth ranges per rock type, and the spectral shifts calculated as the difference between these band depths (0-	

10%-10-20%). 132

TABLE 4.3. The results of synthetic mixtures of gossans and non-gossans. The values given in the table are for unmixed and mixed (gossan - non-gossan) ferric/ferrous absorption feature band positions (in nm); diff.=difference, gos.=gossan, n.-gos.=non-gossan, sedim.=sedimentary, ultram.=ultramafic. 133

TABLE 4.4. The results of synthetic mixtures of gossans and lichens. The values given in the table are for unmixed and mixed (rock-lichen) ferric absorption feature band positions (in nm). Lichens do not have a clear absorption feature in the near infrared wavelength region and hence no values are given for pure (100 %) lichens; diff.= difference, gos.=gossan, sedim.=sedimentary, ultram.=ultramafic. 134

TABLE 4.5. The results of the Spectral Angle Mapper (SAM) similarity comparisons between the airborne gossan endmembers (G1-G7) and the iron oxide minerals (goethite, hematite, lepidocrocite and magnetite) of the USGS spectral library (Clark et al., 2007). SAM similarity scores range from 0 (no match) to 1 (a perfect match). 135

LIST OF FIGURES

FIGURE 2.1. Geological map of the study area showing the locations of the ground spectrometry and sample collection sites. Also shown are the geographical locations of samples 51, 53, 54, 55, 56 and 59. The airborne survey covers the whole study area. Lithology and sulfide lenses GIS data from Minerals and Metals Group Ltd (unpubl.). The < 1% Na ₂ O (in rock surface samples) isoline is modified from Morrison (2004). sp.=spectrometry.	46
FIGURE 2.2. A) Typical undisturbed rhyolitic rock outcrop with lichen cover. B) Left half: undisturbed rhyolitic rock outcrop with lichen cover, and right half: spectral measurement being taken with contact probe from pressure-washed, rhyolitic rock outcrop.	47
FIGURE 2.3. Photomicrographs of samples: A) 51; B) 53; C) 54; D) 55; E) 56; F) 59. All photomicrographs in plain polarized light.	48
FIGURE 2.4. A) Bivariate plot of the Fe-OH wavelength position (in nm) versus the Mg/(Mg+Fe) ratio of biotite/chlorite. B) Bivariate plot of the Al-OH wavelength position (in nm) versus the Si/Al ratio of white micas. C) Bivariate plot of the Al-OH wavelength position (in nm) versus the Mg+Fe content of white mica. All graphs are shown with a linear fit line.....	49
FIGURE 2.5. Ground spectrometry; A) histogram of the wavelength range of the Fe-OH absorption features after hull quotient correction; B) 1: spectral measurement 50 (2259 nm), spectrum 2: spectral measurement 282 (2250 nm); C) spectra 1 and 2 after hull quotient correction. Spectra 1 and 2 represent the long (2259 nm) and the short (2250 nm) endmembers of the Fe-OH absorption feature wavelength positions of the ground spectrometry, respectively....	50
FIGURE 2.6. Ground spectrometry; A) spatial distribution map of the Fe-OH wavelength position; B) bivariate plot of the Fe-OH absorption feature wavelength position versus distance to the nearest massive sulfide lens.	51

FIGURE 2.7. Ground spectrometry; A) histogram of the wavelength range of the Al-OH absorption features after hull quotient correction; B) 1: averaged spectral measurements 321-326 (2211 nm), spectrum 2: averaged spectral measurements 193-195 (2195 nm); C) spectra 1 and 2 after hull quotient correction. Spectra 1 and 2 represent the long (2211 nm) and the short (2195 nm) endmembers of the Al-OH absorption feature wavelength positions of the ground spectrometry, respectively..... 52

FIGURE 2.8. A) spatial distribution map of the Al-OH absorption feature wavelength positions extracted from the ground spectrometry; B) spatial distribution map of the 1st and 4th quartile ranges for the Al-OH absorption feature wavelengths extracted from the ground spectrometry..53

FIGURE 2.9. A) frequency distribution histogram of the Al-OH absorption features of the airborne spectrometry; B) frequency distribution histogram of the Al-OH absorption feature wavelengths extracted from ground spectrometry, re-sampled to the sampling interval of the airborne data..... 54

FIGURE 2.10. A) Spatial distribution map of the interpolated Al-OH absorption feature wavelengths extracted from the airborne data; B) spatial distribution map of the 4th quartile of the Al-OH absorption features extracted from the ground spectrometry (2207-2211 nm) and airborne spectrometry (2205-2206 nm). Also shown in figures A and B is an area of altered rock that is characterized by relatively long Al-OH wavelength positions both in the ground and airborne spectra ("area of enhanced alteration"). Rhyolitic rock outcrops, sulfide lenses, and the outline of Izok Lake GIS data are from Minerals and Metals Group Ltd. (unpubl.). 55

FIGURE 2.11. A) Ground and airborne spectra; A) 1: spectral measurement 267 (2208 nm), 2: spectral measurement 37 (2202 nm); B) hull quotient-corrected spectra 1 and 2 of Figure A; C) spectral measurements 267 (2206 nm, spectrum 1) and 37 (2200 nm, spectrum 2) shown in

Figure A, resampled to the sampling interval of the airborne spectra; D) hull quotient-corrected spectra 1 and 2 of Figure C; E) Airborne spectra 1-4, representing the absorption features near 2194 nm (spectrum 1), 2200 nm (spectrum 4), 2206 nm (spectrum 2) and 2212 nm (spectrum 3); F) hull quotient-corrected spectra 1-4 of Figure E. The sampling interval of the spectra is denoted by "x" in Figures B, D and F. 57

FIGURE 3.1. Location map and geological map of the Izok Lake study area showing the locations of the ground spectrometric sites, samples, drill cores and lithochemical samples. The geology and projected location of massive sulphide zones are from Minerals and Metals Group Ltd, unpublished..... 93

FIGURE 3.2. A) Reflectance spectra from drill cores HEN352 ("HEN352-49", spectrum 1) and HEN-400 ("HEN400-0", spectrum 2); B) Selected range plot of hull quotient-corrected spectra 1 (absorption feature wavelength position: 2216 nm) and 2 (absorption feature wavelength position: 2194 nm) shown in A; C) Reflectance spectra from drill cores HEN-188 ("HEN188-16", spectrum 1) and HEN252 ("HEN252-12", spectrum 2); D) Selected range plot of hull quotient-corrected spectra 1 (absorption feature wavelength position: 2259 nm) and 2 (absorption feature wavelength position: 2246 nm) shown in C..... 94

FIGURE 3.3. Frequency distribution histograms of absorption band position for: A) drill core Al-OH absorption; B) drill core Fe-OH absorption; C) ground spectra Al-OH absorption; D) ground spectra Fe-OH absorption. 95

FIGURE 3.4. Bivariate plot of the visually estimated alteration intensity (VEAI) of the drill cores versus A) the calculated chlorite-carbonate-pyrite index (CCPI) (expressed as %) and; B) the calculated Ishikawa index (AI) (expressed as %). 96

FIGURE 3.5. Bivariate plot of the chlorite-carbonate-pyrite index (CCPI, expressed as %)

calculated from the lithogeochemical data for the drill core samples versus A) the Al-OH wavelength positions (in nm) and; B) the Fe-OH wavelength positions (in nm). 97

FIGURE 3.6. A vertical cross section of the lithogeochemical and spectral trends across seven drill cores (HEN-172, HEN-173, HEN-197, HEN-262, HEN-273, HEN-309 and HEN-340). Downhole variation of: A) Cu contents (ppm); B) Zn contents (ppm); C) chlorite-carbonate-pyrite index (CCPI, %) values; D) Al-OH absorption feature wavelength positions (nm); E) Fe-OH absorption feature wavelength positions (nm). The Cu and Zn contents of the drill cores are extracted across all lithologies and the CCPI, Al-OH and Fe-OH values are extracted from the rhyolitic rock sections of the drill cores. Subfigure F: a map view of the locations of the drill cores. 98

FIGURE 3.7. Bivariate plots of: A) the Fe-OH absorption feature wavelengths of the ground spectra versus the Ishikawa index (AI, expressed as %), extracted from the rhyolitic rock sections of the ground samples and; B) the Fe-OH absorption feature wavelengths versus whole rock Na₂O content (expressed as %), extracted from the rhyolitic rock sections of the ground samples. 99

FIGURE 3.8. Colour gradient map of the absorption feature wavelength positions extracted from the drill core and ground spectra for A) Al-OH and B) Fe-OH. C) Color gradient map of the AI calculated from the lithogeochemical data for drill core and ground samples..... 100

FIGURE 3.9. Bivariate plots of the absorption feature wavelength positions of the ground and drill core spectra versus distance from massive sulfide mineralization for A) Al-OH and,B) Fe-OH. 101

FIGURE 4.1. The locations of the samples and the airborne survey in the context of the tectonic elements of the Ungava peninsula. The tectonic units are modified after St-Onge and Lucas

(1993). Inset figure: A focus area for airborne data analysis. 136

FIGURE 4.2. An ultramafic gossan sample: A) a weathered surface; B) a fresh cut surface. ... 137

FIGURE 4.3. The frequency distribution (n=423314) of the ferric iron absorption band position (A) and band depth (B) acquired by means of a sample imagery. 138

FIGURE 4.4. The averaged spectra of the 0-10 % and 10-20 % band depths for sedimentary rocks (A) and the corresponding hull quotient and band center (B); the averaged spectra of the 0-10 % and 10-20 % band depths for mafic and ultramafic rocks (C) and the corresponding hull quotient and band center (D). 139

FIGURE 4.5. Synthetic spectral mixtures of gossan and non-gossans for sedimentary rocks (A) and related hull quotient spectra (B); for mafic rocks (C) and related hull quotient spectra (D); and for ultramafic rocks (E) and related hull quotient spectra (F). 140

FIGURE 4.6. Synthetic spectral mixtures of gossan and lichen for sedimentary gossan (A) and related hull quotient spectra (B); for mafic gossan (C) and related hull quotient spectra (D); and for ultramafic gossan (E) and related hull quotient spectra (F). 141

FIGURE 4.7. A comparison of airborne gossan endmembers (A-G as endmembers G1-G7) with laboratory spectra from samples. Each frame displays the gossan and non-gossan sample spectra of highest similarity score (as measured by SAM). Endmember G6 (Frame F) has no spectrally similar laboratory equivalent. The number refers to the sample number followed in brackets by the SAM similarity score. S=sedimentary sample, UM=ultramafic sample. 142

FIGURE 4.8. A true color composite (R: 641 nm, G: 546 nm, B: 463 nm) of the "focus area" (A) and the spatial distribution of the airborne gossan endmembers (G1-G7) shown in the context of a thematic geological map by Rogge et al. (2014) (B). The letters A-G refer to clusters of different airborne gossan endmembers. A: clusters of endmembers G1, G3 and G4 associated

with sediments that lie between the mafic and ultramafic units; B: endmember G4 occurrences along river beds; C: endmember G1 and G4 occurrences at the base of ultramafic units; D: sediments associated with the endmember G6; E: occurrences of the endmember G7 associated with the pyroxenite/peridotite rock outcrops; F: restrictive occurrences of the endmember G5 within mafics rocks; G: rock outcrops associated with the endmember G2, primarily along the perimeter of ultramafics with some occurrences along a river bed..... 143

CHAPTER 1 - Introduction

1.1 MOTIVATION FOR RESEARCH

Remote sensing is based on measuring reflected or emitted light from the surface of the Earth. Remote sensing techniques have been used to estimate the mineralogical properties of rocks ever since the first spaceborne multispectral datasets became available in the 1970's (Abrams et al. 1977, Rowan et al. 1977, Goetz and Rowan 1981). These initial, largely qualitative efforts of image interpretation gradually became more quantitative at the onset of hyperspectral sensors in the 1980's. Since then, the ever increasing spatial and spectral resolution of the spectrometers has led to the development of a range of techniques to extract geological information from remote sensing data. This is enabled by the large number of contiguous and narrow bands acquired by hyperspectral sensors, as opposed to only a few wide bands acquired by multispectral sensors.

Airborne and spaceborne remote sensing techniques are particularly useful in areas of difficult access, such as the subarctic and the Arctic. Despite the lack of infrastructure and the inhospitable climate, demand for raw materials has led to intense mineral exploration in these high latitude regions (Mager 2009). The Arctic is environmentally fragile and as a consequence has been observed to be warming at about twice the rate of the rest of the world in response to global climate change (Winton 2006). This development is associated with the expected recession of Arctic sea ice (Granier et al. 2006), which can open new opportunities for marine transportation of raw materials.

Although many parts of the Arctic and the subarctic are north of the treeline making them

ideal for remote sensing studies, these areas are also characterized by an abundant low-growing ground cover (e.g. mosses and lichens), persistent clouds and low sun angles (Longton 1988, Intrieri et al. 2002, Shupe and Intrieri 2004). While some of these problems can be mitigated by means of careful timing of data acquisition and sophisticated data processing algorithms (Stow et al. 2004), lichens can compromise the ability to detect the spectral properties of rocks (Rivard and Arvidson 1992). Lichens are the dominant autotrophs of many Arctic and subarctic ecosystems (Longton 1988) due to their capability to withstand extreme conditions, including cosmic radiation in space (Sancho et al. 2007). In addition to being extremely resilient, lichens are optically thick, and hence prevent the transmission of light into the rock substrate (Bechtel et al. 2002). Circumventing this problem, most previous remote sensing studies have been conducted in arid, low latitude regions with little or no vegetation (Van der Meer et al. 2012).

Several authors have used Landsat multispectral data to map lithologies in subarctic and Arctic areas (see e.g. Harding et al. 1989, Mustard 1994, Schetselaar and de Kemp 2000, Schetselaar and Ryan 2009, Leverington and Moon 2012). These studies show that although some success has been obtained by applying multispectral remote sensing data to differentiate lithologic variations in northern areas, the spatial and spectral resolution of these datasets poses limitations on their use. Contrary to this, Staenz et al. (2000), Harris et al. (2005), Harris et al. (2006), Leverington (2010) and Rivard et al. (2010) have applied hyperspectral data to discriminate rock types in high latitude regions. The above mentioned studies suggest that the large amount of data produced by hyperspectral sensors enable more accurate mapping of rocks than multispectral data. Moreover, the higher spectral resolution and sampling interval of hyperspectral data is particularly important for distinguishing spectrally similar rocks.

Furthermore, the above mentioned studies indicate that in many northern areas there is enough exposure to detect the spectral properties of rocks despite the problem lichens and other tundra vegetation pose for remote sensing studies. Nevertheless, the ability to detect chemical compositional changes of minerals, associated with hydrothermal alteration, has not been demonstrated thus far in these environments. Detecting such alteration footprints is potentially more challenging than discriminating different rock units, because hydrothermal alteration induces subtle changes in the spectral shape of specific minerals (e.g. white micas), and these changes can be difficult to detect by remote sensing means.

Remote sensing techniques can be successfully applied to detect minerals, because these basic building blocks of rocks have characteristic spectral signatures. The processes that determine these signatures can be classified into two groups: electronic transitions short of 1200 nm, and molecular vibrations long of 1200 nm (Hunt and Ashley 1979).

Electronic processes can be classified into electronic transitions, charge transfers, color centers and conduction band transitions (Hunt 1977). The first two are most relevant to mineralogical applications of remote sensing (Goetz et al. 2009). Electronic transitions (crystal field effects) are induced by the interactions of transition metals (e.g. Fe) and the negatively charged dipolar groups that cause the *d* subshells of the transition element ions to be perturbed. As a result, the energy levels of the *d* orbitals are split and a transition of an electron from a lower energy level to a higher energy level is triggered (Burns 1993). Charge transfers (or: the inter-element electron transition) result from a relocation of an electron to a neighbouring ion in the crystal structure. Absorptions caused by charge transfers are strong and extend from the ultraviolet wavelength region (10-400 nm) into the visible wavelength region (400-700 nm) and

beyond (Burns 1993, Cornell and Schwertmann 2003).

Useful geological information can also be extracted from the overtones and combination tones of the fundamental OH-stretching modes that appear long of 1200 nm (Hunt 1979). These absorption features are caused by the vibrational processes that are triggered when the frequency of electromagnetic radiation matches the vibrational energy of a molecule, setting its atomic units into motion (Nielsen 1951, Hunt 1979).

1.2 GOALS OF THE THESIS AND TESTED HYPOTHESIS

In this context, my research begins with an investigation on the usability of airborne hyperspectral data for delineating hydrothermal alteration zones in a subarctic area of abundant lichens on rock outcrops. I then proceed to investigate the applicability of hyperspectral remote sensing data for estimating hydrothermal alteration intensity variation using a volcanogenic massive sulfide (VMS) deposit as a test environment. Finally, I study the optical thickness properties of gossans and the effects of the rock substrates and lichens on their spectral properties. These investigations were conducted in two economically important areas: Izok Lake in Nunavut, Canada and the Cape Smith Belt in northern Quebec, Canada. The Izok Lake Zn-Cu-Pb-Ag VMS deposit is one of the largest undeveloped Zn-Cu deposits in North America, and the Cape Smith Belt hosts the fourth most productive cluster of magmatic Ni-Cu deposits in Canada (Morrison 2004, Lydon 2007). VMS deposits are major sources of base and precious metals (Galley et al. 2007) in addition to being associated with early life forms (Rasmussen 2000), and hence increasing knowledge on these hydrothermal environments can bring new insights into the origins of life.

Most previous studies to have applied hyperspectral remote sensing data to delineate hydrothermal alteration zones of VMS deposits have been conducted in low latitude regions (see e.g. Herrmann et al. 2001, Van Ruitenbeek et al. 2006, Van der Meer 2012, Van Ruitenbeek et al. 2012) and the influence of lichens on the ability to detect these alteration zones by remote sensing means has been poorly addressed. However, VMS deposits also occur in northern areas (Lydon 2007) that are in general characterized by an abundant lichen cover on rock outcrops.

Gossans result from the weathering and leaching of sulfide deposits. Gossans are visible indicators of ore deposits due to their distinct, earthy colors. Iron oxide minerals, the main constituents of gossans, have a pronounced absorption feature near 900 nm (the "ferric absorption feature"). In the past, the wavelength position of this absorption feature has been used to infer the mineralogical composition of the iron oxide minerals (see e.g. Scheinost et al. 1998). This absorption feature was also used by Conradsen and Harpøth (1984) and Bedini (2011) to delineate rocks rich in iron oxides in central East Greenland. However, the area used in these studies is well exposed, overcoming the problem of lichens, discussed above. On the contrary, Rogge et al. (2014) used hyperspectral airborne data to detect gossans and other rock types in the Cape Smith Belt that is characterized by an abundant lichen cover on many rock outcrops. These studies show that gossans can be detected by remote sensing means in high latitudes. Despite these promising results, the ability to detect different rock substrates (sedimentary, mafic and ultramafic) underneath gossans by remote sensing means is poorly constrained, irrespective of its potential to focus exploration efforts on the most promising rock outcrops or lithologies. The ability to detect both gossans and their underlying rock substrates is particularly relevant when there is a known link between ore deposits and specific rock types. Moreover, the effects of

lichens on the spectral shape of the ferric absorption feature are not well established in spite of the prevalence of lichens in subarctic and Arctic areas.

The main goal of my thesis is to investigate the potential and limitations of hyperspectral remote sensing techniques for mineral exploration in the Arctic and subarctic. This involves exploring and evaluating the following scientific hypothesis:

a) The spatial dimensions of hydrothermal alteration zones and gossans can be delineated by airborne hyperspectral remote sensing even in areas of abundant lichen cover on rock outcrops. This can be achieved by removing pixels associated with lichens and using the remaining pixels to extract the spectral characteristics of the white micas, biotite/chlorite group minerals and the iron oxide minerals.

b) Hyperspectral remote sensing data can be used to assess the large scale hydrothermal alteration intensity variation trends of VMS deposits by comparing the spectral properties of the phyllosilicate minerals to alteration indices extracted from the bulk rock chemistry. In practice, this can be achieved by comparing the wavelength positions of the Al-OH and Fe-OH absorption features attributed to white micas and biotite/chlorite group minerals to the chosen alteration indices, such as the Ishikawa index (Ishikawa et al. 1976) and the chlorite-carbonate-pyrite index (Large et al. 2001).

c) Some gossans are optically thin, which enables light to penetrate the rock substrate. While this can make the detection of the mineralogy of the underlying rock substrate possible by remote sensing means, it can also cause the spectral features of the oxidized surfaces of gossans and their underlying rock substrates to be spectrally mixed.

d) Lichens can influence the spectral shape of gossans as a result of spectral mixing.

In the context of the goals and hypothesis mentioned above, the specific goals of my work are:

1) To evaluate the potential of airborne hyperspectral remote sensing data and techniques to delineate the hydrothermal alteration zones and gossans of different rock types in areas of abundant lichens on rock outcrops.

2) To assess the potential of hyperspectral remote sensing data and techniques for unmasking the large scale hydrothermal alteration intensity trends of a volcanogenic massive sulfide (VMS) deposit.

3) To investigate the optical thickness properties of gossans in the short-wave infrared region (SWIR, 1300-2500 nm).

4) To investigate the effect of the rock substrates and lichens on the spectral properties of gossans in the visible-near infrared wavelength region (VNIR, 400-1300 nm).

1.3 ORGANIZATION OF THE THESIS

In the three chapters outlined below, I present investigations aimed to satisfy the goals and objectives of a doctoral dissertation.

Chapter two discusses the use of hyperspectral remote sensing data for the detection of hydrothermal alteration zones of volcanogenic massive sulfide deposits. This chapter is in press as K. Laakso, B. Rivard, J. Peter, H.P. White, M. Maloley, J. Harris and D. Rogge, "Application of airborne, laboratory and field hyperspectral methods to mineral exploration in the Canadian

Arctic: recognition and characterization of volcanogenic massive sulfide-associated hydrothermal alteration in the Izok Lake deposit area, Nunavut, Canada", *Economic Geology*. Dr. Jan Peter (Geological Survey of Canada), Mr. Matthew Maloley (Canada Center for Remote Sensing) and Dr. Jeff Harris (Geological Survey of Canada) contributed to ground spectrometry and sample collection during field work in 2011, in addition to manuscript edits. Dr. H.P. White (Canada Center for Remote Sensing) gave comments on the first draft of the manuscript. Dr. Benoit Rivard was the supervisory author and was involved with manuscript composition. The author of this thesis conducted field work in 2013 together with Dr. Jan Peter.

Chapter three investigates the usability of hyperspectral remote sensing data for the detection of hydrothermal alteration intensity variation of VMS deposits. This chapter has been written as a manuscript to be submitted for publication. As in Chapter two, Dr. Benoit Rivard was the supervisory author and was involved with manuscript composition. Dr. Jan Peter played an instrumental role in field work.

Chapter four comes logically after the first two chapters because in this chapter the spectral properties of gossans, the weathering surfaces of sulfide deposits, are discussed. Dr. Derek Rogge (German Aerospace Center, Germany) contributed to the data analysis, all the sample collection during field work in 2009 and 2010 in addition to sample preparation for X-Ray Diffraction analysis discussed in Chapter four. Dr. Rogge also gave comments on the first draft of the manuscript, that make up the contents of Chapter four, and that will later be submitted for publication. As in Chapters two and three, Dr. Benoit Rivard was the supervisory author and was involved with manuscript composition.

If not mentioned above, this thesis is an original work by Kati Laakso. No part of this thesis has been previously published.

LITERATURE CITED

- Abrams, M., Ashley, R., Rowan, L., Goetz, A. and Kahle, A., 1977. Mapping of hydrothermal alteration in the Cuprite mining district, Nevada, using aircraft scanner images for the spectral region 0.46 to 2.46 μm . *Geology* 5: 713–718.
- Bechtel, R., Rivard, B. and Sánchez-Azofeifa, A., 2002. Spectral properties of foliose and crustose lichens based on laboratory experiments. *Remote Sensing of Environment* 82: 389–396.
- Bedini, E., 2011. Mineral mapping in the Kap Simpson complex, central East Greenland, using HyMap and ASTER remote sensing data. *Advances in Space Research* 47: 60-73.
- Burns, R.G., 1993. *Mineralogical applications of crystal field theory*. 2nd edition. Cambridge University Press, Cambridge, UK.
- Conradsen, K. and Harpøth, O., 1984. Use of Landsat multispectral scanner data for detection and reconnaissance mapping of iron oxide staining in mineral exploration. Central East Greenland. *Economic Geology* 79: 1229–1244.
- Cornell, R.M. and Schwertmann, U., 2003. *The iron oxides: Structure, properties, reactions, occurrences and uses*. 2nd edition. Wiley-VCH GmbH & Co., Weiheim, Germany.
- Galley, A.G., Hannington, M.D. and Jonasson, I.R., 2007. Volcanogenic massive sulphide deposits. In: Goodfellow, W.D. (ed.): *Mineral deposits of Canada: A synthesis of major deposit-types, district metallogeny, the evolution of geological provinces, and exploration methods*. Special Publication No. 5, Geological Association of Canada, Ottawa, Canada: 141-161.

- Goetz, A.F.H., Curtiss, B. and Shiley, D.A., 2009. Rapid gangue mineral concentration measurement over conveyors by NIR reflectance spectroscopy. *Minerals Engineering* 22: 490-499.
- Goetz, A.F.H. and Rowan, L.C., 1981. Geologic remote sensing. *Science* 211: 781–791.
- Granier, C., Niemeier, U., Jungclaus, J.H., Emmons, L., Hess, P., Lamarque, J.-F., Walters, S. and Brasseur, G.P., 2006. Ozone pollution from future ship traffic in the Arctic northern passages, *Geophysical Research Letters* 33: L13807, doi:10.1029/2006GL026180.
- Harding, D.J., Wirth, K.R. and Bird, J.M., 1989. Spectral mapping of Alaskan ophiolites using Landsat thematic mapper data. *Remote Sensing of Environment* 28: 219-232.
- Harris, J.R., Ponomarev, P., Shang, J. and Rogge, D., 2006. Noise reduction and best band selection techniques for improving classification results using hyperspectral data: application to lithological mapping in Canada's Arctic. *Canadian Journal of Remote Sensing* 32: 341-354.
- Harris, J.R., Rogge, D., Hitchcock, R., Ijewliw, O. and Wright, D., 2005. Mapping lithology in Canada's Arctic: application of hyperspectral data using the minimum noise fraction transformation and matched filtering. *Canadian Journal of Earth Sciences* 42: 2173-2193.
- Herrmann, W., Blake, M., Doyle, M., Huston, D., Kamprad, J., Merry, N. and Pontual, S., 2001. Short wavelength infrared (SWIR) spectral analysis of hydrothermal alteration zones associated with base metal sulfide deposits at Rosebery and Western Tharsis, Tasmania, and Highway-Reward, Queensland. *Economic Geology* 96: 939–955.
- Hunt, G.R., 1977. Spectral signatures of particulate minerals in the visible and near infrared. *Geophysics* 42: 501-513.

- Hunt, G.R., 1979. Near-infrared (1.3-2.4 μm) spectra of alteration minerals—Potential for use in remote sensing. *Geophysics* 44: 1974–1986.
- Hunt, G.R. and Ashley, R.P., 1979. Spectra of altered rocks in the visible and near infrared. *Economic Geology* 74: 1613–1629.
- Intrieri, J.M., Shupe, M.D., Uttal, T. and B.J. McCarty., 2002. An annual cycle of Arctic cloud characteristics observed by radar and lidar at SHEBA. *Journal of Geophysical Research* 107: SHE 5-1 – SHE 5-15.
- Ishikawa, Y., Sawaguchi, T., Iwaya, S.-i. and Horiuchi, M., 1976. Delineation of prospecting targets for Kuroko deposits based on modes of volcanism of underlying dacite and alteration haloes. *Mining Geology* 26: 105–117.
- Large, R.R., Gemmell, J.B., Paulick, H. and Huston, D.L., 2001. The alteration box plot: A simple approach to understanding the relationship between alteration mineralogy and litho geochemistry associated with volcanic-hosted massive sulfide deposits. *Economic Geology* 96: 957–971.
- Leverington, D.W., 2010. Discrimination of sedimentary lithologies using Hyperion and Landsat Thematic Mapper data: a case study at Melville Island, Canadian High Arctic. *International Journal of Remote Sensing* 31: 233-260.
- Leverington, D.W. and Moon, W.M., 2012. Landsat-TM-based discrimination of lithological units associated with the Purtunig ophiolite, Quebec, Canada. *Remote Sensing* 4: 1208-1231.
- Longton, R.E., 1988. *Biology of polar bryophytes and lichens*. Cambridge University Press, Cambridge, UK.

- Lydon, J.W., 2007. An overview of the economic and geological contexts of Canada's major mineral deposit types. In: Goodfellow, W.D. (ed.); Mineral Deposits of Canada. A synthesis of major deposit-types, district metallogeny, the evolution of geological provinces, and exploration methods. Special Publication No. 5, Geological Association of Canada, Ottawa, Canada: 3–48.
- Mager, D., 2009. Climate change, conflicts and cooperation in the Arctic: Easier access to hydrocarbons and mineral resources? *The International Journal of Marine and Coastal Law* 24: 347–354.
- Morrison, I.R., 2004. Geology of the Izok massive sulfide deposit, Nunavut Territory, Canada. *Exploration and Mining Geology* 13: 25–36.
- Mustard, J.F., 1994. Lithologic mapping of gabbro and peridotite sills in the Cape Smith fold and thrust belt with thematic mapper and airborne radar data. *Canadian Journal of Remote Sensing* 20: 222-232.
- Nielsen, H.H., 1951. The vibration-rotation energies of molecules. *Reviews of Modern Physics* 23: 90–136.
- Rasmussen, B., 2000. Filamentous microfossils in a 3,235-million-year-old volcanogenic massive sulphide deposit. *Nature* 405: 676-679.
- Rivard, B. and Arvidson, R.E., 1992. Utility of imaging spectrometry for lithologic mapping in Greenland. *Photogrammetric Engineering & Remote Sensing* 58: 945–949.
- Rivard, B., Rogge, D., Jeng, J., Grant, B. and Pardy, J., 2010. Hyperspectral sensing in support of mineral exploration in the Arctic: Example from the Cape Smith nickel belt, Canada. *Proceedings of the 'Hyperspectral 2010 Workshop', Frascati, Italy.*

- Rogge, D., Rivard, B., Segl, K., Grant, B. and Feng, J., 2014. Mapping of Ni-Cu-PGE ore hosting ultramafic rocks using airborne and simulated EnMap hyperspectral imagery, Nunavik, Canada. *Remote Sensing of Environment* 152: 302-317.
- Rowan, L.C., Goetz, A.F.H. and Ashley, R.P., 1977. Discrimination of hydrothermally altered and unaltered rocks in visible and near infrared multispectral images. *Geophysics* 42: 522–535.
- Sancho, L.G., de la Torre, R., Horneck, G., Ascaso, C., de los Rios, A., Pintado, A., Wierzchos, J. and Schuster, M., 2007. Lichens survive in space: Results from the 2005 LICHENS Experiment. *Astrobiology* 7: 443-454.
- Scheinost, A.C., Chavernas, A., Barrón, V. and Torrent, J., 1998. Use and limitations of second-derivative diffuse reflectance spectroscopy in the visible to near-infrared range to identify and quantify Fe oxide minerals in soils. *Clays and Clay Minerals* 46: 528–536.
- Schetselaar, E. and de Kemp, E., 2000. Image classification from Landsat TM, airborne magnetics and DEM data for mapping Paleoproterozoic bedrock units, Baffin Island, Nunavut, Canada. *International Archives of Photogrammetry and Remote Sensing*, Vol. XXXIII, Part B7: 1325-1332.
- Schetselaar, E.M., Ryan, J.J., 2009. Remote predictive mapping of the Boothia mainland area, Nunavut, Canada: an iterative approach using Landsat ETM, aeromagnetic, and geological field data. *Canadian Journal of Remote Sensing* 35: S72-S94.
- Shupe, M.D. and Intrieri, J.M., 2004. Cloud radiative forcing of the Arctic surface: The influence of cloud properties, surface albedo, and solar zenith angle. *Journal of Climate* 17: 616-628.
- Staeenz, K., Nadeau, C., Secker, J. and Budkewitsch, P., 2000. Spectral unmixing applied to vegetated environments in the Canadian Arctic for mineral mapping. *Proceedings of the*

International Archives of Photogrammetry and Remote Sensing, Vol. XXXIII, Part B7: 1464-1471.

Stow, D.A., Hope, A., McGuire, D., Verbyla, D., Gamon, J., Huemmrich, F., Houston, S., Racine, C., Sturm, M., Tape, K., Hinzman, L., Yoshikawa, K., Tweedie, C., Noyle, B., Silapaswan, C., Douglas, D., Griffith, B., Jia, G., Epstein, H., Walker, D., Daeschner, S., Petersen, A., Zhou, L. and Myneni, R., 2004. Remote sensing of vegetation and land-cover change in Arctic Tundra Ecosystems. *Remote Sensing of Environment* 89: 281–308.

Van der Meer, F.D., van der Werff, H.M.A., van Ruitenbeek, F.J.A., Hecker, C.A., Bakker, W.H., van der Meijde, M., Carranza, E.J.M., de Smeth, J.B. and Woldai, T., 2012. Multi- and hyperspectral geologic remote sensing: A review. *International Journal of Applied Earth Observation and Geoinformation* 14: 112–128.

Van Ruitenbeek, F.J.A., Cudahy, T.J., van der Meer, F.D. and Hale, M., 2012. Characterization of the hydrothermal systems associated with Archean VMS-mineralization at Panorama, Western Australia, using hyperspectral, geochemical and geothermometric data. *Ore Geology Reviews* 45: 33–46.

Van Ruitenbeek, F.J.A., Debba, P., van der Meer, F. D., Cudahy, T., van der Meijde, M. and Hale, M., 2006. Mapping white micas and their absorption wavelengths using hyperspectral band ratios. *Remote Sensing of Environment* 102: 211–222.

Winton, M., 2006. Amplified Arctic climate change: What does surface albedo feedback have to do with it? *Geophysical Research Letters* 33: L03701, doi:10.1029/2005GL025244.

CHAPTER 2 - Application of airborne, laboratory and field hyperspectral methods to mineral exploration in the Canadian Arctic: recognition and characterization of volcanogenic massive sulfide-associated hydrothermal alteration in the Izok Lake deposit area, Nunavut, Canada

2.1 INTRODUCTION

Volcanogenic massive sulfide (VMS) deposits are economically important sources of Zn, Cu, Pb, Ag, and Au (Galley et al. 2007). These deposits form from hydrothermal fluids (downdrawn and modified seawater) that are heated by magmas and circulate in the subsurface, dissolve metals and other solutes in the rocks along the flow path, and vent at the seafloor. The varying temperature and chemical gradients of the fluids along their circulation path result in a range of chemical, mineralogical and textural compositional changes in the host rocks. The extent and magnitude of these changes are determined by physico-chemical factors such as the temperature, pH, water/rock ratios, f_{O_2} (oxygen fugacity), f_{S_2} (sulfur fugacity), as well as the composition of the hydrothermal fluids and the host rocks.

The mineralogical assemblages that develop through hydrothermal alteration in different VMS deposits vary, but phyllosilicate minerals such as chlorite and sericite (fine-grained micaceous minerals, Eberl et al. 1987) are typically present. The phyllosilicates that form through hydrothermal alteration can have variable chemical compositions (e.g., muscovite, paragonite, phengite, celadonite, Fe-chlorite and Mg-chlorite) within a VMS system due to different physico-chemical conditions in different parts of the system. High temperatures are favorable for the formation of Al-rich muscovite and Fe-rich chlorite and biotite (Miyashiro and Shido 1985,

Cathelineau 1988, Duke 1994). Factors such as the chemical composition of the hydrothermal fluids and the host rocks may simultaneously influence the composition of the developing mineral assemblages (Kranidiotis and MacLean 1987, Cathelineau 1988, Van Ruitenbeek et al. 2005). The chemical composition of the phyllosilicate minerals may change through several substitutions such as simple Mg-Fe substitution, Fe³⁺-Al substitution or Tschermak substitution, in which octahedral Mg and Fe substitute for Al concurrently with tetrahedral Si for Al (Miyashiro and Shido 1985, Guidotti and Sassi 1998, Yang et al. 2011).

The short-wave infrared (SWIR, 1300-2500 nm) spectrometric response of the phyllosilicate minerals is sensitive to the cation substitutions discussed above. These substitutions can be observed as spectral shifts within the Al-OH and Fe-OH absorption features near 2200 nm and 2250 nm, respectively (Clark et al. 2007). The wavelength position of the Al-OH absorption feature, present in dioctahedral muscovite, shifts systematically toward shorter wavelengths as the Al content of the octahedral sites increases, and the opposite effect, or a systematic shift toward longer wavelengths, takes place when the relative proportion of octahedral Mg and Fe increase (Post and Noble 1993, Duke 1994). These dioctahedral minerals form a solid solution series between paragonite, muscovite and celadonite (Velde 1965, Li et al. 1994) and are commonly termed white micas. Intermediate in composition between muscovite and aluminoceladonite/celadonite are the phengitic micas (Rieder et al. 1998). Similar to white micas, the Fe-OH absorption feature that is present in biotite and chlorite (Scott and Yang 1997), shifts toward shorter wavelengths with increasing Mg content, and toward longer wavelengths with increasing Fe content (Bassett 1960, McLeod et al. 1987).

Previously, the wavelength positions of the Al-OH and Fe-OH absorption features extracted from laboratory hyperspectral data were used to delineate the alteration zones of the Myra Falls VMS deposit in British Columbia (Jones et al. 2005) and the Boco VMS Prospect in Tasmania, Australia (Herrmann et al. 2009). Van Ruitenbeek et al. (2006) mapped the Al-OH absorption feature wavelength positions of the Panorama VMS district, Soansville greenstone belt, Pilbara region, Australia, by using spectral ratios extracted from hyperspectral airborne data. These studies show that the spectral shifts of the Al-OH and Fe-OH absorption feature wavelength positions can be detected by hyperspectral remote sensing in VMS deposit environments and that these shifts are associated with chemical compositional variations of the phyllosilicate minerals. However, the application of hyperspectral airborne data for mapping the Al-OH and Fe-OH absorption feature wavelength positions of phyllosilicate minerals has not previously been demonstrated in high latitude environments that typically have abundant lichen cover on rock outcrops. Lichens are the dominant autotrophs of many subpolar ecosystems due to their ability to withstand extreme environmental conditions (Longton 1988, Purvis 2000). Lichens are also optically thick, and hence can hinder the detection of spectral features of rock substrates (e.g., Ager and Milton 1987, Rivard and Arvidson 1992, Bechtel et al. 2002).

The present study was conducted in the Point Lake greenstone belt, in the area that hosts the Izok Lake (65° 38'N, 112 48'W in Nunavut, Canada) Zn-Cu-Pb-Ag VMS deposit. The objective was to determine if the distribution of hydrothermally altered rocks associated with the deposit could be mapped using hyperspectral remote sensing data and processing methods, in the presence of abundant lichens on the rock outcrops. This objective was addressed by examining the Al-OH and Fe-OH absorption feature wavelengths positions of white micas and

biotite/chlorite. These absorption feature wavelength positions were examined using various levels of spectroscopic data that were related to the mineralogy of the study area and distance from mineralization.

2.2 STUDY AREA

The study area is in the Kitikmeot region of Nunavut, northern Canada (Fig. 2.1). The area comprises 15.5 km² of gently rolling bedrock hills that are interrupted by more prominent ridges. It also hosts numerous ponds and lakes. The nearest weather station to provide long-term climatological data is located in Lupin (weather station "Lupin A", 65°45' N , 111°15' W), 72 km NE of Izok Lake. According to this weather station, the daily average temperature is -10.9 °C between 1982 and 2006 (Government of Canada 2014). The Kitikmeot region is characterized by Arctic tundra vegetation that is dominated by shrubs, sedges, grasses and flowering herbs (Laidler et al. 2008). Lichens are abundant on many outcrops in the Izok Lake area, and typically cover 75-100% of the rock surfaces.

The study area is underlain by the Point Lake Formation of the Yellowknife Supergroup, which is part of the Slave structural province (Bostock 1980). The massive sulfide lenses of the Izok Lake deposit are predominantly hosted by Archean (2.6 Ga; Mortensen et al. 1988) rhyolitic rocks and, to a lesser extent, by intermediate to mafic metavolcanic and metasedimentary rocks. These rhyolitic rocks contain white mica, biotite and chlorite some of which formed as the result of hydrothermal alteration that occurred during massive sulfide emplacement (Morrison 2004). The original alteration minerals have been metamorphosed to pyroxene hornfels facies conditions that have induced both textural and mineralogical changes. Porphyroblastic textures predominate

and minerals such as anthophyllite and cordierite occur in places (Morrison 2004). Despite metamorphism, the primary alteration assemblages are largely preserved in the stratigraphic hanging wall and footwall of the deposit, and this serves as the rationale for evaluating the application of hyperspectral methods for detecting this hydrothermal alteration in the exploration for VMS mineralization.

2.3 SPECTRAL DATASETS

2.3.1 Ground site selection and spectral measurements

Several sub-areas were selected strategically within the study area for the acquisition of ground spectrometry with the aim of recognizing and delineating any hydrothermal alteration zones associated with the Izok Lake deposit. These sites encompass the intensely altered areas proximal to mineralization, and less altered areas distal from the massive sulfides. An estimate of the intensity of alteration throughout the study area was obtained by using the bulk rock Na_2O isopleth map of Morrison (2004; Fig. 2.1). Sodium depletion results from the breakdown of sodic plagioclase during hydrothermal alteration, and is a reliable indicator of hydrothermal alteration intensity. Areas of both intense and weak alteration were targeted to reveal possible trends in the chemical compositions of the phyllosilicate minerals by collection and analysis of 285 spectra from the areas of intense alteration and 170 spectra from less intensely altered areas. In total, 455 spectral measurements were collected from 108 rhyolitic rock outcrops over two field seasons (2010 and 2013). At each measurement site, one to eight spectral measurements, each with a 1 cm diameter circular footprint, were collected from the lichen-free and weathered surfaces of each rock outcrop. These measurements were collected randomly from an area of approximately

0.25 m² per rock outcrop. All the measurements were collected from the horizontal surfaces of the rock outcrops to ensure optimal comparability of the ground and airborne spectra. In the field, visual inspection of the rock outcrops, combined with knowledge of the geology of the study area (see Fig. 2.1), were used to ensure that spectral measurements were obtained only from rhyolitic rock outcrops. Some of the rhyolitic outcrops were stripped of lichens and surficial material by Minerals and Metals Group (MMG; the owner of the deposit) personnel with the use of a pressure washer, and these rock outcrops were preferred for spectral measurements over non-pressure washed outcrops because they are devoid of lichens (Fig. 2.2). The solution used for pressure washing was water from the lakes of the study area. Undisturbed, natural (i.e. non-pressure washed), rhyolitic outcrops have variable lichen cover that ranges from sparse (covering 0-25% of the surface area) to abundant (covering 75-100% of the surface area).

All spectral measurements were made with a PANalytical Boulder Inc. (formerly ASD Inc.) FieldSpec[®] 3 (hereafter referred to as ASD) spectrometer that records spectra in the 350-2500 nm wavelength range with a spectral resolution of 10 nm and a sampling interval of 1 nm in the SWIR wavelength region. All measurements were obtained using a contact probe that has an internal illumination source that ensures consistent illumination conditions during data acquisition. Radiance values were converted to reflectance values by means of a Spectralon[™] reflectance panel (i.e. the "white reference", SRT-99-100, Labsphere, Inc., North Sutton, NH, USA), a commercially available plate made of polytetrafluoroethylene (Bruegge et al. 1993). These relative reflectance values were converted to absolute reflectance values by multiplying the relative reflectance value of each wavelength with the reflectance factor obtained from the calibration certificate of the Spectralon[™] panel. This correction was conducted in accordance

with the procedure suggested by Clark et al. (2002). The correction is necessary because the SpectralonTM panel has an absorption feature near 2130 nm (Clark et al. 2002). Dark current and white reference measurements were repeated every ten minutes during data acquisition in order to ensure consistency in the spectral measurements. The geographic coordinates of the rock outcrops were recorded using a handheld GPS, and all spectral measurements were acquired within a five metre radius from the X,Y co-ordinates recorded using the GPS. Each spectrum acquired in the field consists of 60 individual measurements taken consecutively and averaged by the ASD instrument.

2.3.2 Sample suite and laboratory spectral measurements

A hand specimen sample was collected from each of 60 rock outcrops that represent 65% of the 108 rhyolitic rock outcrops visited during the field works in 2010 and 2013. The aim was to collect samples both from the intensely altered and less altered parts of the study area. The bulk rock Na₂O content isopleth map of Morrison (2004, Fig. 2.1) was used to guide the selection of the ground spectrometry sample locations; 39 samples were collected from the intensely altered areas, and 21 samples were collected from the less/least intensely altered parts of the study area. All samples collected have at least one weathered surface and sparsely lichen covered outcrops were preferentially sampled.

One to six spectral measurements were obtained in the laboratory from the weathered, lichen-free surfaces of each sample using an ASD FieldSpec[®] 3. If there were no weathered surfaces available, measurements were made on fresh surfaces. Reflectance spectra were acquired

following the method described for ground spectrometry, except that each spectrum acquired in the laboratory is the average of 25 individual consecutive measurements.

2.3.3 Airborne spectral imaging

Airborne hyperspectral data were collected over a 94 km² area comprising 58 flightlines within the Point Lake greenstone belt and centered on the Izok Lake deposit area during the period August 2-21, 2010. The data were acquired by SpecTIR LLC of Reno, Nevada using the ProSpecTIR[®] (AISA dual) sensor at a one metre spatial resolution. This sensor collects data in a nominal spectral resolution of 5 nm between 390 to 2500 nm. These data were resampled to a 6.3 nm interval, resulting in 360 channels.

The airborne dataset was pre-processed by SpecTIR by first converting the radiance data to reflectance data using the ATCOR-4[®] software package and MODTRAN[®] 4 atmospheric lookup tables (Richter and Schläpfer 2002). Next, the dataset was geocorrected using the data extracted from a three-axis gyroscope attitude INS (Inertial Navigation System) that was positioned with a 12-channel GPS system and boresight calibration data. The data quality was confirmed by the Canada Centre for Remote Sensing using the Imaging Spectrometer Data Analysis System (ISDAS) package as outlined in Hitchcock and White (2007).

2.3.4 Petrography and mineral chemistry

Polished thin sections (PTS) were prepared from thirteen hand samples collected from outcrops during ground spectrometry collection (27, 29, 31, 34, 35, 37, 47, 51, 53, 54, 55, 56 and 59). These samples were chosen because their spectra have either an Al-OH or an Fe-OH absorption feature, which indicates the presence of white mica, biotite and chlorite. The PTS of

samples 51, 53, 54, 55, 56 and 59 (geographic locations shown in Fig. 2.1) were examined under a Nikon Labophot2[®] polarizing light microscope and the presence or absence of biotite, chlorite and muscovite was recorded at over 500 random spots within each PTS.

Next, seven samples (27, 29, 31, 34, 35, 37, 47) were selected for electron microprobe analysis (EMPA) based on the short, intermediate and long wavelength positions of their Al-OH and Fe-OH absorption features. Between 4 and 7 areas were selected within each PTS for analysis of white mica, biotite and chlorite. The PTS were carbon-coated and analyzed using a JEOL 8230 SuperProbe[®] electron microprobe operating at 20kV and using a beam current of 20 nA. Mineral formulae were calculated on the basis of 22 oxygens for micas (white micas and biotite) and 28 oxygens for chlorite. The results were compared to the spectral characteristics of these minerals by calculating the Pearson correlation coefficient between the Al-OH and Fe-OH wavelength positions and the Al, Fe, Mg and Si contents of white micas, biotite and chlorite, as determined by EMPA. These cations were chosen because their relative proportions in the octahedral sites of the phyllosilicate minerals determine the wavelength positions of the Al-OH and Fe-OH absorption features (Bassett 1960, McLeod et al. 1987, Duke 1994). In practice, we used the average compositions of these cations within each mineral (white mica and biotite/chlorite) for each sample (PTS). These average mineral cation compositions were then compared to the average Al-OH and Fe-OH absorption feature wavelength positions of the same samples from which the PTS were prepared. Sample 29 does not display clear Al-OH absorption features, and hence the average Al-OH absorption feature wavelength position of this sample is not compared to its chemical composition.

2.4 SPECTRAL ANALYSIS METHODOLOGIES

2.4.1 Ground and hand sample spectral processing

Of the 455 spectral measurements acquired in the field, forty were discarded because of low signal-to-noise ratios or failed readings. The Al-OH and Fe-OH absorption feature wavelength positions of the remaining spectra were manually extracted after hull quotient correction to discern the spectral shifts associated with the areas of hydrothermal altered rock. Hull quotient correction is conducted to reduce the effects of the background spectral slope when the absorption feature wavelength is to be accurately recorded (Clark and Roush 1984). In practice, the hull quotient correction (continuum removal) is conducted by fitting straight-line segments (convex hull points) over the shoulders (maxima) of an absorption feature, and dividing the reflectance values of the absorption feature by these convex hull points. The resulting hull quotient values are normalized to a 0-1 scale hence removing the effects of albedo variance in the spectrum. An average wavelength position was then computed from the spectral measurements. In practice, this was achieved by conducting continuum removal and recording the minimum (the smallest hull quotient value) of each spectrum. These values were next averaged per rock outcrop. This averaging resulted in 98 Al-OH and 85 Fe-OH absorption feature wavelength position observations. In the case of the hand specimen samples, from one to six measurements per sample of the Al-OH and Fe-OH absorption feature wavelength positions were averaged.

A continuous, gradational surface was created for the Al-OH and Fe-OH wavelength positions in order to visualize the spatial trends of the ground spectra. This was accomplished by using the nearest ten wavelength positions within a 200 m radius to calculate the contents of each

pixel in the surface via the IDW (Inverse Distance Weighting) interpolation tools of the ArcGIS software package (Cressman 1959, Shepard 1968, Philip and Watson 1982, ESRI 2011). The diameter of the interpolated surface around each ground spectral observations (200 m) was chosen based on the spatial distribution of the Al-OH and Fe-OH wavelength position observations. More specifically, this diameter was estimated using the average and maximum distances of each Al-OH (average: 87 m, maximum: 383 m) and Fe-OH (average: 105 m, maximum: 1333 m) absorption feature field measurement to the nearest field measurement. The 200 m radius was estimated based on these average and maximum distances to minimize extrapolation and to create a realistic representation of the spatial trends of the absorption feature wavelength positions in the study area. The resulting surface was normalized and divided into four quartiles to highlight the spatial distribution of the shortest and longest quartile (25%) of the Al-OH and Fe-OH wavelength positions.

In a separate analysis, the Al-OH and Fe-OH wavelength positions were examined in the context of the location of the rhyolitic rock outcrops relative to the nearest massive sulfide lens. This was carried out to reveal the possible spatial trends of the wavelength positions within the study area with respect to the ore zones. Only the intensely altered areas (as defined by the Na₂O isopleth maps of Morrison (2004; see Fig. 2.1) were included in this analysis and hence areas distal to the massive sulfide lenses (within 5800-6800 m) were omitted.

2.4.2 Airborne spectrometric data processing

Airborne data collected over the study area were used to map the spatial distribution of the Al-OH wavelength positions of the rhyolitic rocks in the study area. The spatial distribution

of the Fe-OH absorption feature wavelengths was investigated, but these absorption features were left out of the analysis because this specific absorption feature was not readily identified in the airborne spectrometry. More specifically, the Fe-OH absorption features were estimated to be too weak to be reliably detectable by remote sensing means. As a first pre-processing step, the full airborne dataset was clipped to correspond to the estimated dimensions (1.9 km²) of the rhyolitic rock outcrops in the study area map provided by MMG. Next, the image was processed in three steps: i) pixels attributed to vegetation were removed, ii) spectral unmixing was performed to remove pixels most impacted by the effects of lichens, and iii) the wavelength position of the Al-OH absorption absorption feature in all remaining pixels was determined.

The chlorophyll index developed by Gitelson and Merzlyak (1994, Normalized Difference Vegetation Index NDVI₇₀₅) was used to identify pixels attributed to photosynthetic vegetation. This index uses wavelengths 705 nm and 750 nm in the visible and near-infrared wavelength regions, along the "red edge" spectral feature of vegetation to detect attributes such as the chlorophyll content (Sims and Gamon 2002). Next, a threshold value of 0.2 was applied to the NDVI₇₀₅ results to mask out pixels associated with vegetation. This threshold was chosen based on the results of Gitelson and Merzlyak (1994), who attributed NDVI₇₀₅ values greater than 0.2 with increasing chlorophyll content of vegetation. The masked pixels comprise 80% of the total number of pixels covering rhyolitic rock outcrops ($n=75499$).

Spectral endmembers were extracted from the remaining airborne pixels by means of the Spatial-Spectral Endmember Extraction (SSEE) tool of Rogge et al. (2007). SSEE comprises three steps where the image is first divided into equal sized non-overlapping subset regions where a set of eigenvectors that explain most of the spectral variance is calculated for each subset. Then

the image data are projected onto the local eigenvectors compiled from all subset regions and the pixels occupying either extreme of the vectors are retained as candidate endmembers. Lastly, within a given spatial window, the candidate pixels are averaged with all other pixels that are spectrally similar. One hundred and thirty seven endmembers were obtained through this endmember extraction process, of which 22 were chosen to represent rocks, vegetation and lichens, or any mixtures thereof. This endmember spectral database of 22 endmembers served as input for the linear spectral unmixing computer calculations (Adams et al. 1993, Boardman 1993, Settle and Drake 1993). The resulting 22 abundance fraction images were analyzed and attributed to lichen, vegetation, or lichen-rock or vegetation-rock mixtures, based on their spectral characteristics. A single lichen-coated endmember image was chosen to represent pixels of rhyolitic rock outcrops that have a minimal lichen cover, and a threshold of 0.6 (fractional abundances of 60 % or higher) was applied to this endmember image to retain rhyolitic rock outcrop pixels with sparse vegetation and lowest degree of lichen cover. After this procedure, 1% of the original number of pixels associated with the rhyolitic rock outcrops remained in the dataset.

Next, the wavelength position of the Al-OH absorption feature was calculated after hull removal from the 2188-2212 nm wavelength range. This absorption feature wavelength position range was chosen because it encompasses the wavelength range of absorption features present in the ground spectra (see below). Upon analysis of the airborne spectra, the 2212 nm wavelength position was masked out because it was deemed to be associated with lichens and other vegetation rather than rock outcrops. Similarly, the 2194 nm Al-OH wavelength in the airborne spectrometry was left out of further analysis because the spectral shape of the absorption features

in this wavelength range are strongly influenced by lichens and do not represent rhyolitic rock outcrops. The basis for masking out these absorption features is the near absence of an absorption feature at 2194 nm and 2212 nm in ground spectra, whereas these absorption features are ubiquitously present in the airborne spectrometry, suggesting association with other elements than rhyolitic rocks. It is also notable that the necessity to further mask out pixels suggests that the abundant lichen cover on the rock outcrops of the study area prevented a complete separation of lichens and rock surfaces through spectral unmixing. One factor that may have contributed to this result is the spectral variation of vegetation with varying nitrogen, cellulose and lignin contents. The spectral shape of plants varies as a function of these chemical elements and compounds (Kokaly et al. 2009), which can increase the spectral diversity and make endmember extraction more challenging.

At this stage, 261 pixels remained, representing 0.3% of the original amount of pixels associated with the rhyolitic rock outcrops. The inverse distance weighting (IDW) interpolation tools (Cressman 1959, Shepard 1968, Philip and Watson 1982) were then used to create a continuous surface of the Al-OH absorption feature wavelength positions of these pixels by employing the nearest 15 Al-OH absorption feature wavelengths to calculate the contents of each pixel in the interpolated surface. The interpolated surface was cropped to a 200 m buffer around each observation in order to minimize the effects of extrapolation to areas of no observations.

The results were then validated against ground spectrometry. The averaged spectra of all the rock outcrops measured in the field were then re-sampled to the sampling interval of the ground spectrometry (1 nm in the SWIR wavelength region) to the sampling interval of the airborne spectrometry (6.3 nm). Each Al-OH absorption feature wavelength position ($n=261$) in

the airborne spectrometric dataset was then linked with its geographically nearest Al-OH absorption feature wavelength position ($n=98$), extracted from the ground spectrometry. These observations were then compared, and the accuracy of the airborne Al-OH absorption feature wavelength position was assessed based on how well each observation corresponded to the spatially nearest ground spectral observation. More specifically, the accuracy was assessed based on the difference (in nm) between the Al-OH absorption feature wavelength positions of the airborne and ground spectral datasets.

2.5 RESULTS

2.5.1 Mineralogy

All samples examined under the microscope (51, 53, 54, 55, 56 and 59) are fine-grained (average 0.2 mm), and some display mineralogical banding. White micas are present in four samples, biotite in five samples and chlorite in one sample (Figs. 2.3A-F, Table 2.1). White micas are responsible for the Al-OH absorption features, and biotite or chlorite are associated with the Fe-OH absorption features of the samples. However, this match is not perfect, as sample 53 does not reveal white micas in the thin section investigated despite the presence of an Al-OH absorption feature. In all likelihood the spatial distribution of white micas is inhomogeneous in sample 53.

2.5.2 Mineral chemistry

Table 2.2 summarizes the mineral compositions for white micas, chlorite, and biotite, as determined by EMPA for the seven samples (PTS) and the average Al-OH and Fe-OH wavelength positions obtained from the corresponding hand specimen. Analysis of the EMPA

data revealed a strong correlation between the Fe-OH wavelength position and the Mg/(Mg+Fe) ratio of biotite/chlorite (Pearson's $r=-0.893$, $n=7$, $p=0.007$, 99% confidence level, two-tailed) (Fig. 2.4A). Similarly, correlation analysis shows a strong, statistically significant correlation between the Al-OH wavelength positions and the Si/Al ratio of white micas (Pearson's $r=0.861$, $n=6$, $p=0.028$, 95% confidence level, two-tailed, Fig. 2.4B). Furthermore, a strong correlation (Pearson's $r=0.849$, $n=6$, $p=0.032$, 95% confidence level, two-tailed) exists between the Al-OH wavelength position and the Mg+Fe content of white micas (Fig. 2.4C). Ratios that measure the amount of Na (sodic content) in the mineral lattice of white micas are not applied in this analysis, because the shortest wavelength position of the white micas is at relatively long wavelengths (2198 nm), indicating that none of the samples are truly sodic (i.e. paragonitic).

These relationships between the average Al-OH and Fe-OH wavelength positions, and the chemical composition of the samples indicate that the absorption feature wavelength positions vary systematically with the chemical composition of muscovite and biotite/chlorite. More specifically, the Al-OH wavelength position of the white micas decreases with increasing Al content (measured by the Si/Al ratio) and increases with increasing Mg+Fe content. Similarly, the Fe-OH wavelength position of biotite/chlorite decreases with increasing Mg/(Mg+Fe) ratio (increasing Mg content).

2.5.3 Ground spectrometry

2.5.3.1 Frequency and spatial distribution of the Fe-OH absorption feature wavelength positions

The Fe-OH absorption is present in spectra from 85 of the rhyolitic rock outcrops, (79%, $n=108$). The frequency distribution of these wavelength positions is shown in Figure 2.5A, and

ranges from 2249 nm to 2259 nm (mean=2254 nm, mode=2255 nm, std. dev.=2.078). This broad wavelength range and the presence of values on the extremes of the wavelength positions are illustrated in Figures 2.5B,C. The Shapiro-Wilk normality test shows that the wavelength positions are normally distributed ($p=0.703$) and there are no outliers in the dataset.

The broad wavelength range of the Fe-OH absorption feature wavelengths is also evident in their spatial distribution, shown in Figure 2.6A. Furthermore, the Fe-OH absorption feature wavelengths form two distinct spatial groups that are apparent upon comparison of the average Fe-OH wavelength position of the proximal (398-3146 m from the massive sulfides) and distal (5782-6812 m from the massive sulfides) areas. The proximal area ("area 1" in Fig. 2.6A) of 73 measured rock outcrops has an average Fe-OH absorption feature wavelength position at 2254 nm (std. dev.=1.831), whereas the distal area ("area 2" in Fig. 2.6A) comprised of 12 rhyolitic rock outcrops, has an average Fe-OH wavelength position at 2251 nm (std. dev.=1.215). This trend toward shorter Fe-OH absorption feature wavelength positions is also apparent in the bivariate plot of the Fe-OH absorption feature wavelength positions versus distance from 3146 m to the nearest massive sulfide lens (Fig. 2.6B). Furthermore, there is a statistically significant inverse correlation between the Fe-OH wavelength position and the distance to the massive sulfide lenses (Pearson's $r=-0.324$, $p=0.005$, $n=73$), at the 99% confidence level.

2.5.3.2 Frequency and spatial distribution of the Al-OH absorption feature wavelength positions

An Al-OH absorption feature is present in 98 (91%) spectra from rhyolitic rock outcrops, indicating that the minerals responsible for this spectral feature are abundant throughout the study area. The average wavelengths of the absorption features in these outcrops varies between 2194

nm and 2211 nm (mean=2203 nm, mode=2202 nm, std. dev.=3.084; Fig. 2.7A). The wide range of the absorption feature wavelengths results from spectral shifts, illustrated in Figures 2.7B,C. According to the Shapiro-Wilk normality test, the frequency distribution of the absorption feature wavelength positions is normally distributed ($p=0.063$, $n=98$); furthermore, according to an outlier test, the wavelength positions less than or equal to 2195 nm and greater than or equal to 2210.5 nm are outliers. However, after careful visual inspection of the associated spectra, these wavelength positions were deemed not to be outliers, and for this reason were not removed from the dataset. The extreme Al-OH wavelength positions likely indicate the presence of sodic and phengitic muscovite that have characteristic spectral shifts toward shorter and longer wavelengths, respectively (Duke 1994).

There is no statistically significant Pearson correlation between the averaged Al-OH absorption feature wavelengths of the rhyolitic rock outcrops and the distance to the nearest massive sulfide. However, there is a slight shift toward longer wavelengths in the proximal areas (327-2679 m from the massive sulfides) as opposed to the distal areas (5782-6812 m from the massive sulfides). In the proximal areas ("area 1" in Fig. 2.8A) the average Al-OH absorption feature wavelength of the rhyolitic rock outcrops is 2203 nm ($n=85$, std. dev.=2.983), whereas in the distal areas ("area 2" in Fig. 2.8A) the corresponding average wavelength position is 2201 nm ($n=13$, std. dev.=3.165), but this is a displacement essentially of only one band. Visual inspection of the results (Fig. 2.8A), shows that the massive sulfide lenses are surrounded by relatively high Al-OH absorption feature wavelengths, so that the highest values are located northwest of the massive sulfide lenses. This is also evidenced by a cluster of the upper quartile (highest 25%) Al-OH absorption feature wavelength positions in the vicinity of Izok Lake (Fig. 2.8B). Despite this

apparent trend in the Al-OH absorption feature wavelength positions in the study area, relatively long wavelength positions occur both in the proximal and distal areas, indicating that the Al-OH absorption feature wavelength positions do not vary systematically with distance from the massive sulfide lenses.

2.5.4 Airborne spectrometry

2.5.4.1 Frequency and spatial distribution of the Al-OH absorption feature wavelength positions

The frequency distribution of the Al-OH absorption feature wavelength positions of the airborne data ($n=261$) define two groups: one at 2200 nm and the other at 2206 nm (Fig. 2.9A). The mode and median of the airborne data are both at 2200 nm, and these coincide with the mode and median of the ground spectrometry, that has been re-sampled to the sampling interval of the airborne spectrometry (Fig. 2.9B). Although the values for both the airborne spectrometry and the re-sampled ground spectrometry are identical, the Al-OH wavelength range of the former is relatively narrow compared to that of the latter (2194-2212 nm, Figs. 2.9A,B), indicating that the entire wavelength position range of the Al-OH absorption feature is not detected in the airborne spectrometric dataset. This conclusion is also suggested by the relatively low accuracy of the airborne spectrometry as measured by the difference between the ground and airborne spectra. Sixty five percent of the Al-OH absorption feature wavelength positions in the airborne data ($n=169$) are within three nanometers of their spatially nearest airborne spectrometric value. Within this 65% of observations, there is a strong, statistically significant positive Pearson correlation ($r=0.917$, $p=0.000$, $n=169$, 99% confidence level, one-tailed), between the ground and airborne spectra. The average airborne Al-OH absorption feature wavelength positions in the

proximal ("area 1" in Fig. 2.10A, $n=182$) and distal ("area 2" in Fig. 2.10A, $n=9$) areas, are both 2201 nm, indicating that there is no systematic trend in the airborne Al-OH wavelength positions with distance to the massive sulfide lenses. Despite this, there is a zone of relatively long Al-OH absorption feature wavelength positions in the airborne spectrometry in the vicinity of the massive sulfide lenses. This area, located 800-1900 m west of the sulfide lenses, and shown as an "area of enhanced alteration" in Figures 2.10A,B, coincides spatially with several 4th quartile (the highest 25% of the ground observations at wavelengths between 2207-2211 nm) areas in the ground spectrometry, shown in Figure 2.10B. There are also indications of a spatial continuity of long Al-OH absorption feature wavelengths 1500 m north and 1000 m south of the massive sulfide lenses. Based on the Al-OH absorption features extracted from the airborne spectrometry alone, the areal extent of this alteration zone is $\approx 8.67 \text{ km}^2$.

2.6 DISCUSSION

2.6.1 Validation of the spectrometric datasets

The mineralogical composition of the samples was determined by optical microscopic study of PTS. The presence or absence of the Al-OH and Fe-OH absorption features was compared to the petrographic data for the corresponding PTS. The results indicate that the Al-OH absorption feature is associated with white micas and the Fe-OH absorption feature is associated with biotite and chlorite. However, there is incomplete correspondence between the presence of Al-OH absorption features and the presence of white micas, as an Al-OH absorption feature was detected in sample 53, despite the absence of muscovite in the PTS for this sample (Table 2.1). This is likely due to the inhomogeneous distribution of white mica in sample 53. The discrepancy

between the sizes of the thin sections (26 X 46 mm) and the areas used for making spectral measurements from the samples (on average 100 cm²) entails that there will only be a perfect correlation between the two in samples with homogeneously distributed minerals.

The spectral results were further validated by comparing the spectral shifts of the Al-OH and Fe-OH absorption features to the chemical compositions of biotite, chlorite and white micas in the corresponding samples. The results, shown in Figure 2.4 and listed in Table 2.2, indicate that there is a strong positive correlation between the Si/Al content of white micas and the average Al-OH absorption feature wavelength position. Furthermore, there is a correlation of similar magnitude and direction between the average Al-OH wavelength position of a sample and the Mg+Fe content of its white micas. In contrast, a strong inverse correlation exists between the average Fe-OH wavelength position and the Mg/(Mg+Fe) content of biotite/chlorite within the same sample. These results indicate that the increasing Al content of white micas and the increasing Mg content of biotite/chlorite are associated with the shifts toward shorter wavelengths of the Al-OH and Fe-OH absorption features, respectively. The inverse is true for the increasing Mg,Fe content of the white micas, and Fe content of biotite and chlorite, which is associated with the shifting toward longer wavelengths of the Al-OH and Fe-OH absorption feature wavelength positions. Our findings are consistent with the results of previous studies of Bassett (1960), McLeod et al. (1987), Post and Noble (1993) and Duke (1994) who have documented similar spectral shifts in association with the chemical compositional variation of biotite, chlorite and muscovite.

2.6.2 Absorption feature wavelength positions of the white micas and chlorite group minerals

There is considerable variation in the Al-OH and Fe-OH absorption feature wavelength positions of white mica and biotite/chlorite in the Izok Lake area. These variations likely result from hydrothermal alteration processes active at the time of the massive sulfide formation. The Al-OH wavelength range demonstrated by the ground spectrometry (2194-2211 nm) indicates that the chemical composition of white micas ranges from paragonitic (short wavelength positions near 2195 nm) to muscovitic (wavelength positions near 2200 nm) to slightly phengitic (wavelength position near 2210 nm). Similarly, the chemical compositions of chlorite group minerals range from Mg-rich to Mg-Fe-rich, based on the Fe-OH wavelength positions extracted from the ground dataset. This Mg-rich and Mg-Fe rich chlorite classification is in accordance with the results by Yang and Huntington (1996), who documented Mg-rich chlorite associated with the Fe-OH absorption features between 2252 and 2254 nm, and Mg-Fe chlorite associated with the Fe-OH absorption feature wavelengths between 2256 and 2262 nm. The observed Al-OH and Fe-OH absorption feature wavelength distributions also suggest that the chemical compositional changes within biotite, chlorite and muscovite result in broad and continuous wavelength position data distributions that should be analyzed by means of high spectral resolution datasets with narrow bandpass sampling intervals.

2.6.3 Absorption feature wavelength trends in the ground spectra

The spectral shifts of the Fe-OH absorption features in the ground data were studied by plotting the absorption feature wavelength positions against their distances to the known massive

sulfide lenses (Fig. 2.6B). This bivariate plot, and an interpolated surface (Fig. 2.6A), created from the Fe-OH absorption feature wavelength positions, reveal systematic trends in the Fe-OH absorption feature wavelength positions with distance to the known massive sulfide lenses. This trend is manifested as a shift toward longer Fe-OH absorption feature wavelengths in the area proximal to the massive sulfide lenses (within 300-3100 m), and a shift toward shorter wavelengths in the areas distal from the massive sulfide lenses (within 5800-6800 m). The implication is that altered rocks proximal to the Izok Lake massive sulfide lenses contain Mg-Fe biotite/chlorite, and the distal areas contain Mg-rich biotite/chlorite. Contrary to the observed spatial variability of the Fe-OH absorption feature wavelength, no spatial variability of the Al-OH absorption feature wavelength with respect to distance from massive sulfide lenses was discerned. However, an area of relatively long Al-OH wavelength positions, revealed by an interpolated surface, occurs in the vicinity of the massive sulfide lenses, coinciding with the area of Mg-Fe biotite/chlorite. The long Al-OH wavelength positions of this area (up to 2211 nm) indicate the presence of slightly phengitic muscovite.

2.6.4 Absorption feature wavelength trends in the airborne spectrometry

In order to place the spectral shifts of the Al-OH wavelength positions in the ground spectrometry into a regional context, these data were scaled up to the airborne spectrometry. A comparison between the airborne and ground spectra reveals a detection accuracy of 65%, when each accurately detected airborne Al-OH absorption feature wavelength position was determined to lie within three nanometers from the Al-OH absorption feature wavelength position of the spatially nearest ground spectrum. Problems in the detection of the spectral properties of rock outcrops in the study area, indicated by this relatively low accuracy of the airborne spectrometry,

may result from multiple factors, including the abundant vegetation and lichen cover that necessitated the masking out of 99% of the pixels associated with the rhyolitic rock outcrops in the airborne dataset.

One factor that affects the ability to detect the spectral features of rocks is the sampling interval of the dataset. This is demonstrated in Figure 2.11 that shows the Al-OH absorption feature wavelength positions of the ground spectra (sampling interval: 1 nm; Figs. 2.11A,B) and ground spectra resampled to the sampling interval of the airborne spectra (sampling interval: 6.3 nm; Figs. 2.11C,D). As the sampling interval is decreased from 1 nm to 6.3 nm, the Al-OH absorption feature wavelength positions shift from 2202 nm to 2200 nm (spectrum 2, Figs. 2.11B,D) and from 2208 nm to 2206 nm (spectrum 1, Figs. 2.11B,D). Moreover, as expected the signal-to-noise ratio of the airborne spectral dataset is lower than that of the ground spectral dataset. This is evident in Figures 2.11E,F that show four representative single pixel spectra extracted from the rhyolitic rock outcrops of the airborne spectral dataset. Spectra 2 and 4 have an absorption near 2206 nm and 2200 nm, respectively, whereas spectra 1 and 3 have an absorption near 2194 nm and 2212 nm, respectively. Spectra with an absorption feature near 2200 nm and 2206 nm, extracted from the rhyolitic rock outcrops of the study area, were interpreted to be associated with white micas. When comparing spectra 2 and 4 with spectra 1 and 3 it becomes evident that the absorption of spectra 2 and 4 is slightly broader. However, the overall spectral shape of all the spectra in Figure 2.11E is similar and all have an absorption feature near 2100 nm, indicating spectral mixing between rocks and lichens. Thus, the main reason for masking out the absorption features shorter than 2200 nm and longer than 2206 nm was the discrepancy between the data distributions of the Al-OH absorption feature wavelength

positions of the ground spectra and the airborne data when the full spectral range of the Al-OH absorption features of the ground spectra (2194-2211 nm, Fig. 2.7A) were taken into account.

The problems in detecting the spectral properties of the rock outcrops may be exacerbated by the relatively small proportion of sodic and phengitic micas in the study area, as determined by the distribution of the Al-OH absorption feature wavelengths in the ground spectrometry (Fig. 2.7A). Lesser abundances of minerals result in shallower absorption feature depths (Clark 1999), and for this reason detecting minerals present in lower abundances (e.g. phengitic muscovite in the Izok Lake area) is more challenging than detection of more abundant minerals that have clearly expressed absorption features.

The abundance of biotite and chlorite may also play a role in the detection of their absorption features in the airborne spectrometry. An Fe-OH absorption feature associated with these minerals is present in only 79% of the ground spectra, whereas an Al-OH absorption feature attributed to white micas occurs in 91% of the ground spectra. The higher detection percentage of the Al-OH absorption feature suggests that white micas are more uniformly distributed in the study area than biotite/chlorite. Moreover, the average Fe-OH absorption feature band depth of the ground spectra is 3.3%, whereas the average Al-OH absorption feature band depth of the ground spectra is 20% (scale: 0-100%). The depth of an absorption is related to the abundance of the absorber (Clark 1999) and hence the discrepancy between the Al-OH and Fe-OH absorption band depths indicates that the minerals inducing the former absorption feature are more abundant than the minerals inducing the latter absorption feature. This more uneven distribution and lesser abundance of biotite/chlorite (as opposed to white micas) is the likely determining factor for the lack of detection of biotite/chlorite in the airborne spectra. Other factors, such as the quality of

preprocessing (e.g. atmospheric correction), S/N (signal-to-noise) ratio, sampling interval and band pass of the spectral data can also influence the ability to detect spectral features (Swayze et al. 2003).

Although the detection accuracy of the airborne spectrometry is relatively low, the ability to detect an area of phengitic muscovite using both the ground and airborne datasets independently demonstrates the efficacy of airborne spectrometry for the recognition and delineation of zones of hydrothermally altered rocks in outcrops in the Izok Lake area.

2.6.5 Implications for the interpretation of the deposit fluid flow paths

An area of altered rocks with relatively long Al-OH absorption feature wavelengths of the ground and airborne spectra (Figs. 2.10A,B) was identified in the vicinity of the massive sulfide lenses of the Izok Lake deposit. This area contains phengitic muscovite and intermediate to Fe-rich chlorite, both of which formed at high temperature (200-350°C; Hulen and Nielson 1986; Cathelineau 1988). In addition to temperature, another influence on the chemical composition of white micas and chlorite group minerals is the chemical composition of the hydrothermal fluids (Cathelineau 1988). Elevated Mg^{2+} and Fe^{2+} (relative to Al^{3+}) contents of the hydrothermal fluid favor the formation of phengite (Yang et al. 2011). Thus, the area of altered rocks with long Al-OH absorption feature wavelengths may reflect interaction with high-temperature, metal-rich, and moderately acidic hydrothermal fluids (Lentz and Goodfellow 1993), possibly within or at the margin of a fluid discharge zone.

The chemical composition of chlorite is controlled largely by bulk rock compositions (Inui and Toriumi 2004), and a shift toward more Fe-rich biotite/chlorite in this area corroborates

this interpretation, as a characteristic feature of focused fluid discharge sites is their Fe-rich bulk compositions (e.g., Barrett and MacLean 1994). The area of long Al-OH absorption feature wavelengths partly coincides with an area of the intense hanging wall alteration discussed by Morrison (2004) that he interpreted to be an area of sub-seafloor replacement.

2.7 SUMMARY AND CONCLUSIONS

Our ground hyperspectral results indicate that there is a systematic trend in the Fe-OH absorption feature wavelength position of biotite/chlorite with distance from the VMS deposit. No such trend was identified in the Al-OH feature of white micas, but a spatial pattern of relatively long Al-OH absorption feature wavelength positions was observed in the vicinity of Izok Lake using ground and airborne hyperspectral sensors. This area coincides with relatively long Fe-OH absorption feature positions, detected by means of a ground ASD spectrometer. These findings indicate that hydrothermal alteration zones can be detected by hyperspectral remote sensing, despite the presence of abundant lichen cover in the study area.

The large ranges in the Al-OH and Fe-OH absorption feature wavelengths of muscovite and biotite/chlorite in the Izok Lake area reflect large chemical compositional variations in these minerals. Unlike the white micas that display more spatial variation in their Al-OH wavelength positions, the Fe-OH wavelength positions of biotite/chlorite display consistent and systematic spatial shifts toward longer wavelengths in areas proximal to the massive sulfide mineralization and a shift toward shorter wavelengths in areas distal to the massive sulfides. These shifts indicate that biotite/chlorite becomes more Fe-rich in the vicinity of the ore deposit and more Mg-rich in the distal areas. Unfortunately, the Fe-OH absorption feature associated with

biotite/chlorite could not be detected in the airborne spectrometry, and hence the large-scale trends of the chemical composition of these phyllosilicate minerals remain unconstrained. However, an alteration halo comprising phengitic white micas was detected and delineated using both the ground and airborne spectral datasets. Based on ground spectrometry, this phengitic alteration halo coincides with a zone of Mg-Fe biotite/chlorite proximal to the massive sulfide lenses. This fluid upflow alteration zone extends ≈ 1000 m south, 1500 m north and 1900 m west of the Izok Lake deposit. Despite the low detection accuracy of the airborne data, the ability to identify this hydrothermal alteration zone using airborne hyperspectral remote sensing data shows that this method has great promise in identifying and delineating zones of chlorite and white mica hydrothermally altered rock that may be associated with VMS and other hydrothermal mineral deposits (e.g., orogenic gold) in regions that have considerable lichen cover. This lends support for the development of future airborne and spaceborne hyperspectral sensors of higher signal-to-noise ratios and spectral resolutions that would allow for better spectral unmixing and separation of cellulose and non-photosynthetic vegetation materials from white mica minerals indicative of VMS environments.

Our study also highlights the importance of careful selection of wavelengths for image analysis in environments where the spectral signatures are strongly influenced by spectral mixing. Two absorption feature wavelength positions (2194 nm and 2212 nm) were discarded from the airborne dataset due to the effects of spectral mixing of rocks and vegetation that could not be completely eliminated through spectral unmixing and band ratio analysis of vegetation (NDVI). This step proved essential for obtaining relatively accurate results from the airborne data, regardless of the loss of significant portions of the data.

TABLE 2.1. Thin section samples, their mineralogy and the presence of the Al-OH and Fe-OH absorption features.

Sample no.	Biotite	chlorite	Muscovite	Al-OH	Fe-OH
51	X		X	X	X
53	X			X	X
54	X		X	X	X
55	X		X	X	X
56		X			X
59	X		X	X	X

TABLE 2.2. Average compositions of the samples per mineral and the average Al-OH and Fe-OH absorption feature wavelength positions; *n*=number of analyses per sample; biot.=biotite, chl.=chlorite.

Sample no.	Al-OH (nm)	Fe-OH (nm)	Miner.	Al ₂ O ₃ (wt%)	BaO (wt%)	CaO (wt%)	Cl (wt%)	F (wt%)	FeO (wt%)	K ₂ O (wt%)	MgO (wt%)	MnO (wt%)	Na ₂ O (wt%)	SiO ₂ (wt%)	TiO ₂ (wt%)	V ₂ O ₃ (wt%)	Total
27 (<i>n</i> =70)	2198	2254	M.	35.21	0.11	0.00	0.01	0.11	1.94	9.33	1.31	0.01	0.95	46.58	0.26	0.02	95.84
			B./C.	21.12	0.01	0.00	0.03	0.35	16.59	4.47	15.87	0.16	0.11	31.43	0.51	0.01	90.66
29 (<i>n</i> =45)		2250	M.	29.23	0.24	1.32	0.00	0.24	1.96	9.82	2.83	0.02	0.68	48.72	0.47	0.02	95.55
			B./C.	18.15	0.09	1.11	0.01	0.69	13.94	4.78	16.57	0.10	0.35	35.26	0.87	0.02	91.94
31 (<i>n</i> =38)	2199	2251	M.	34.26	0.24	0.00	0.01	0.10	2.10	10.00	1.30	0.01	0.74	46.17	0.21	0.02	95.16
			B./C.	20.45	0.06	0.00	0.05	0.83	10.51	8.51	14.69	0.08	0.15	37.61	0.74	0.02	93.70
34 (<i>n</i> =46)	2209	2258	M.	31.21	0.32	0.00	0.00	0.22	4.33	10.71	1.53	0.06	0.20	47.03	0.43	0.02	96.06
			B./C.	18.24	0.06	0.01	0.03	0.22	26.51	5.61	7.84	0.68	0.10	31.31	0.96	0.01	91.58
35 (<i>n</i> =59)	2208	2256	M.	30.47	0.27	0.30	0.01	0.23	3.76	10.29	1.50	0.04	0.50	46.99	0.17	0.01	94.55
			B./C.	17.63	0.09	1.35	0.07	0.55	22.71	6.82	6.57	0.37	0.10	36.77	0.78	0.02	93.82
37 (<i>n</i> =55)	2202	2256	M.	31.96	0.08	0.00	0.00	0.10	2.95	11.35	0.44	0.02	0.39	47.37	0.25	0.01	94.92
			B./C.	18.73	0.02	0.00	0.06	0.19	26.57	6.83	5.24	0.40	0.08	33.33	0.96	0.01	92.42
47 (<i>n</i> =37)	2198	2252	M.	35.04	0.05	0.00	0.00	0.04	0.88	10.91	1.00	0.01	0.37	46.13	0.15	0.01	94.59
			B./C.	20.56	0.01	0.00	0.02	0.29	11.68	7.69	16.39	0.05	0.08	35.38	0.53	0.01	92.69

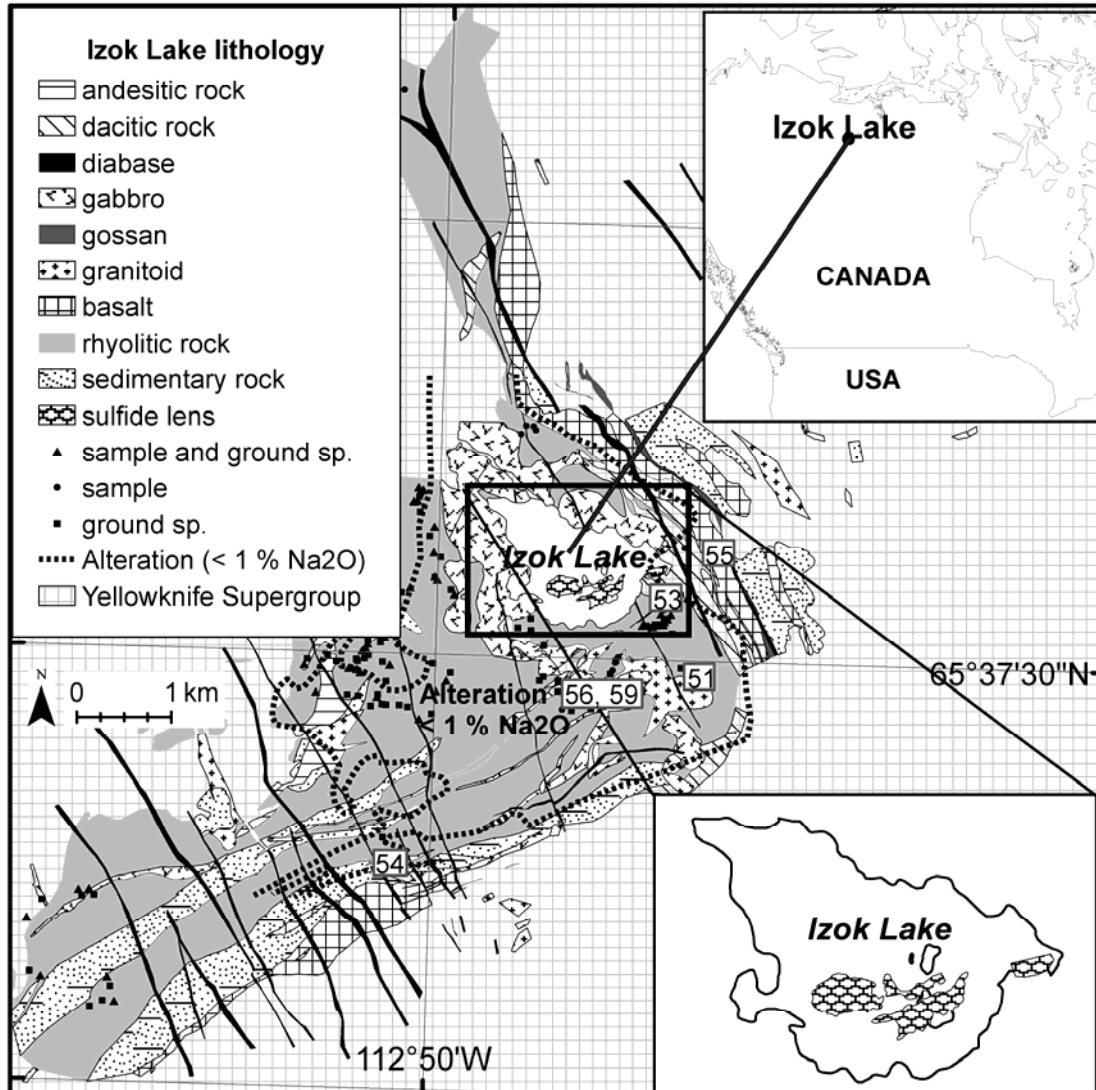


FIGURE 2.1. Geological map of the study area showing the locations of the ground spectrometry and sample collection sites. Also shown are the geographical locations of samples 51, 53, 54, 55, 56 and 59. The airborne survey covers the whole study area. Lithology and sulfide lenses GIS data from Minerals and Metals Group Ltd (unpubl.). The < 1% Na₂O (in rock surface samples) isoline is modified from Morrison (2004). sp.=spectrometry.

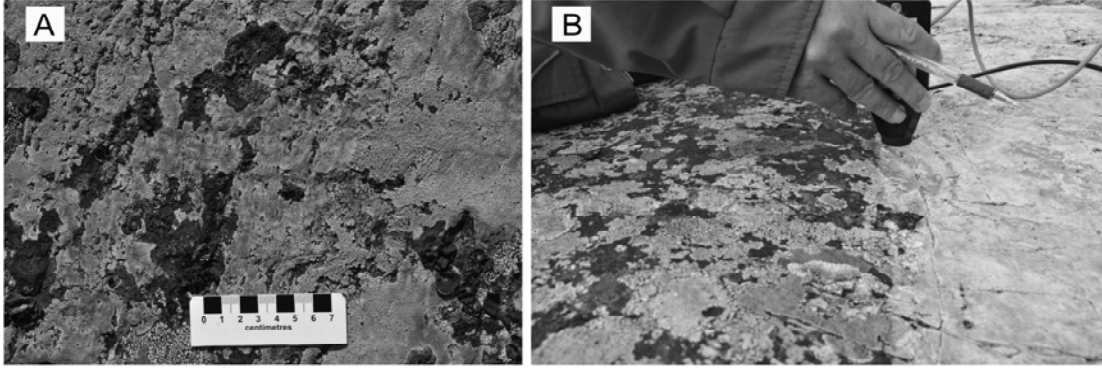


FIGURE 2.2. A) Typical undisturbed rhyolitic rock outcrop with lichen cover. B) Left half: undisturbed rhyolitic rock outcrop with lichen cover, and right half: spectral measurement being taken with contact probe from pressure-washed, rhyolitic rock outcrop.

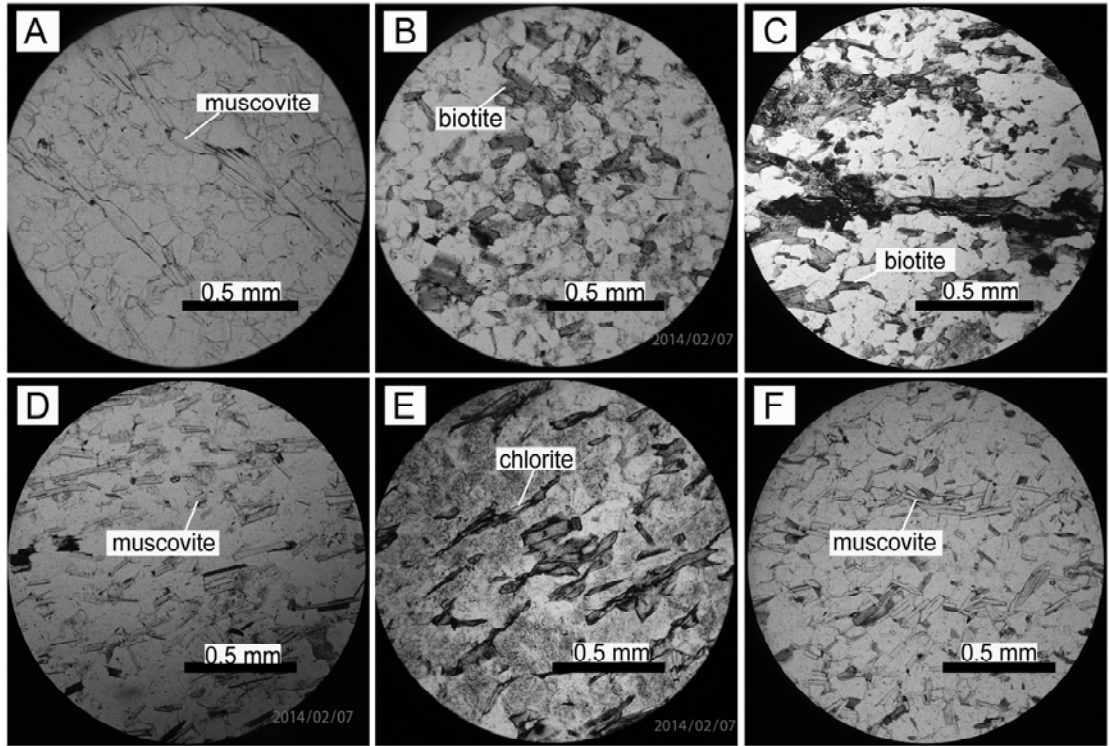


FIGURE 2.3. Photomicrographs of samples: A) 51; B) 53; C) 54; D) 55; E) 56; F) 59. All photomicrographs in plain polarized light.

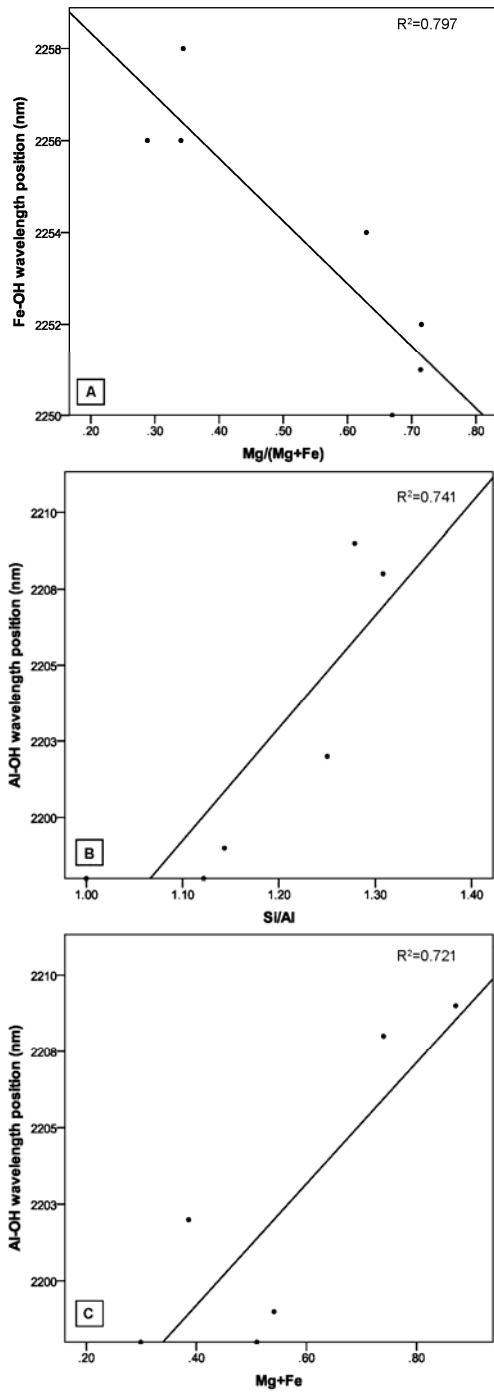


FIGURE 2.4. A) Bivariate plot of the Fe-OH wavelength position (in nm) versus the Mg/(Mg+Fe) ratio of biotite/chlorite. B) Bivariate plot of the Al-OH wavelength position (in nm) versus the Si/Al ratio of white micas. C) Bivariate plot of the Al-OH wavelength position (in nm) versus the Mg+Fe content of white mica. All graphs are shown with a linear fit line.

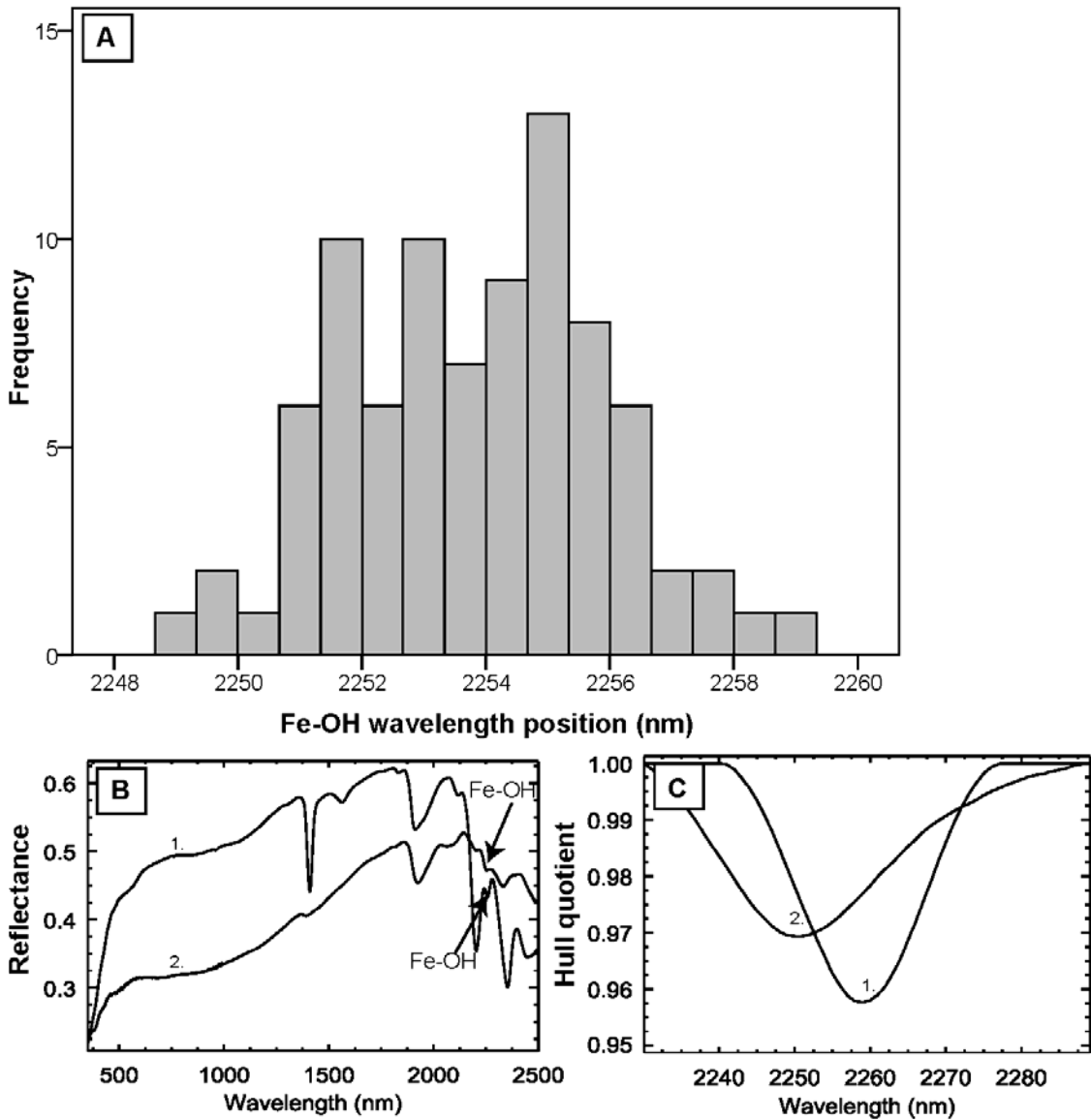


FIGURE 2.5. Ground spectrometry; A) histogram of the wavelength range of the Fe-OH absorption features after hull quotient correction; B) 1: spectral measurement 50 (2259 nm), spectrum 2: spectral measurement 282 (2250 nm); C) spectra 1 and 2 after hull quotient correction. Spectra 1 and 2 represent the long (2259 nm) and the short (2250 nm) endmembers of the Fe-OH absorption feature wavelength positions of the ground spectrometry, respectively.

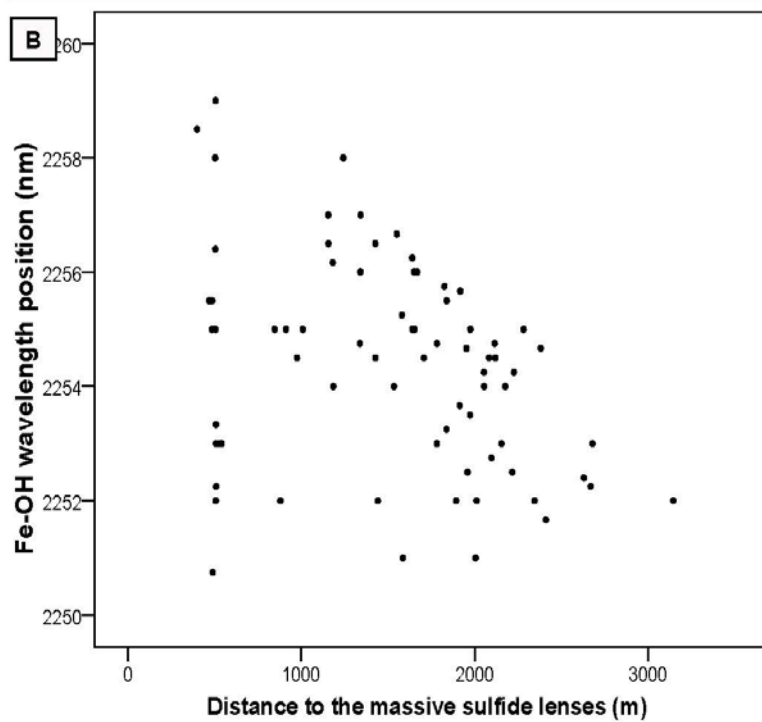
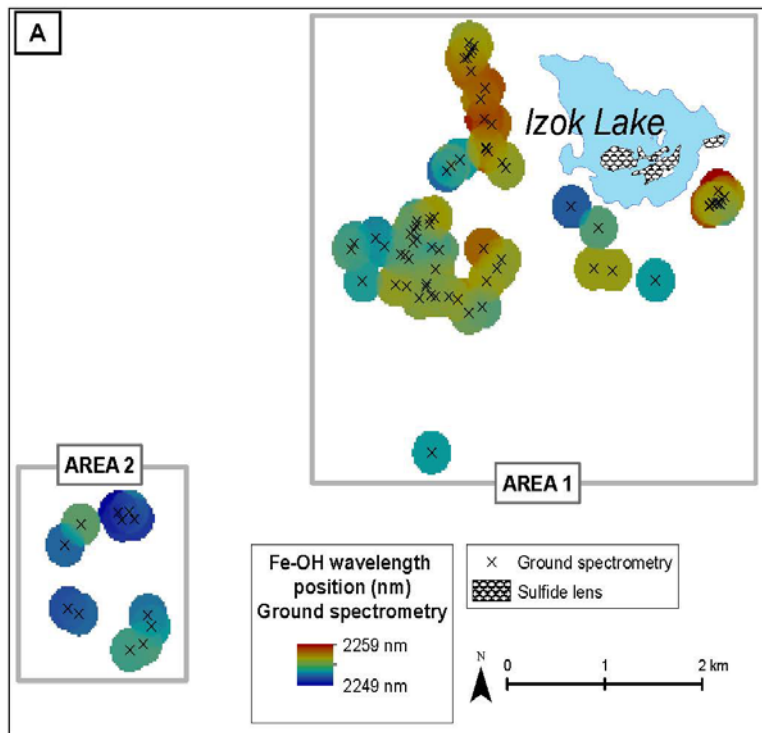


FIGURE 2.6. Ground spectrometry; A) spatial distribution map of the Fe-OH wavelength position; B) bivariate plot of the Fe-OH absorption feature wavelength position versus distance to the nearest massive sulfide lens.

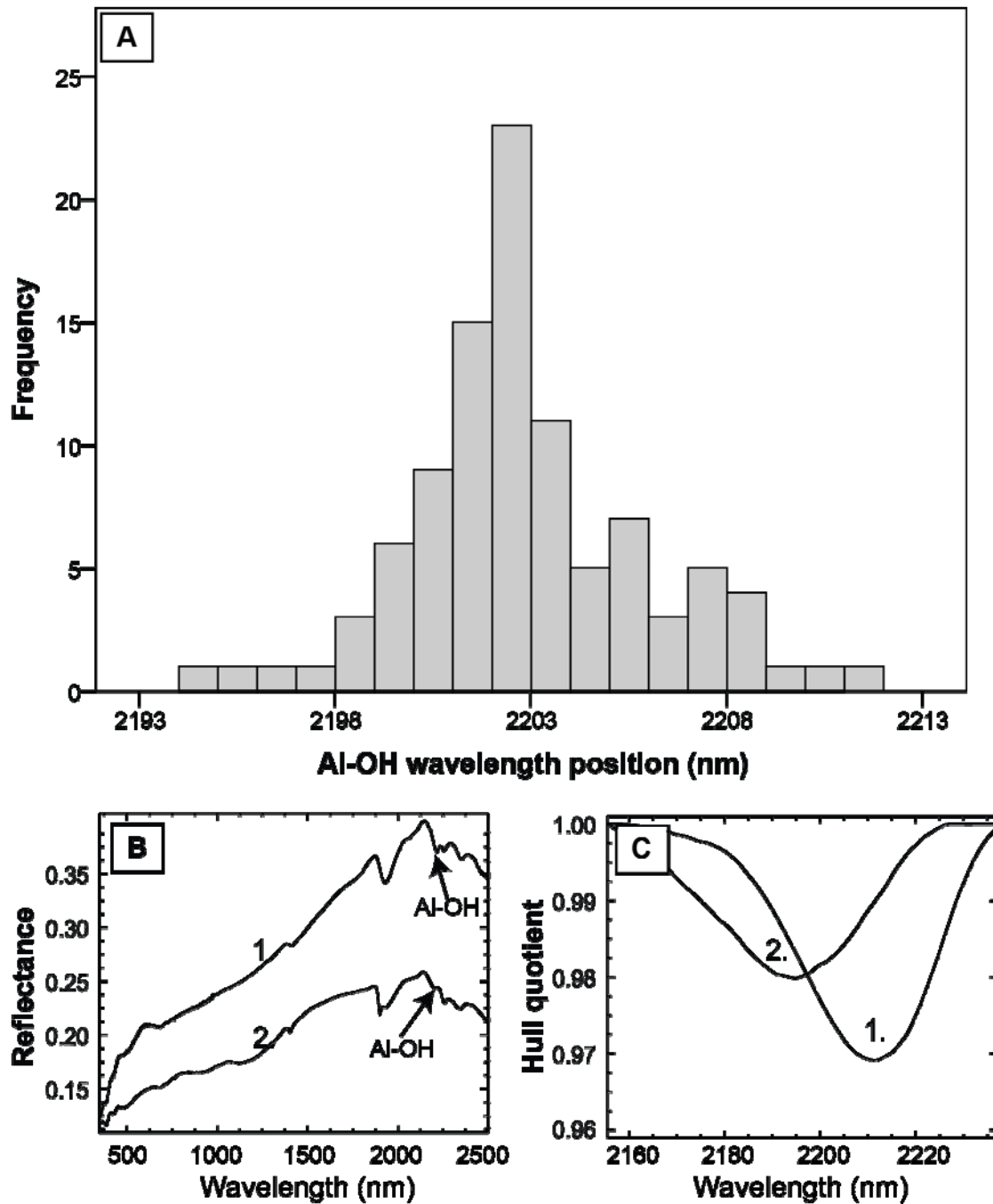


FIGURE 2.7. Ground spectrometry; A) histogram of the wavelength range of the Al-OH absorption features after hull quotient correction; B) 1: averaged spectral measurements 321-326 (2211 nm), spectrum 2: averaged spectral measurements 193-195 (2195 nm); C) spectra 1 and 2 after hull quotient correction. Spectra 1 and 2 represent the long (2211 nm) and the short (2195 nm) endmembers of the Al-OH absorption feature wavelength positions of the ground spectrometry, respectively.

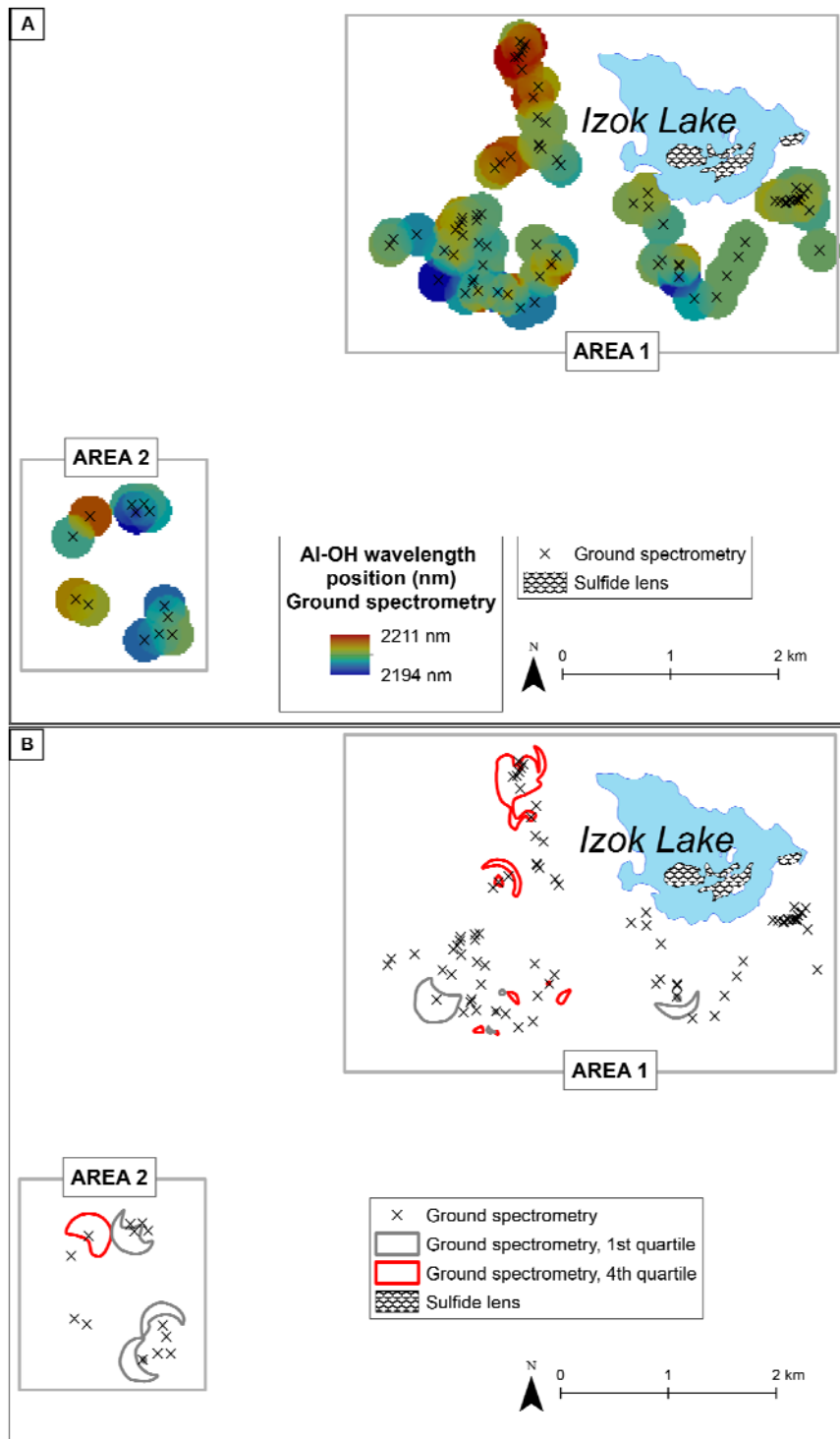


FIGURE 2.8. A) spatial distribution map of the Al-OH absorption feature wavelength positions extracted from the ground spectrometry; B) spatial distribution map of the 1st and 4th quartile ranges for the Al-OH absorption feature wavelengths extracted from the ground spectrometry.

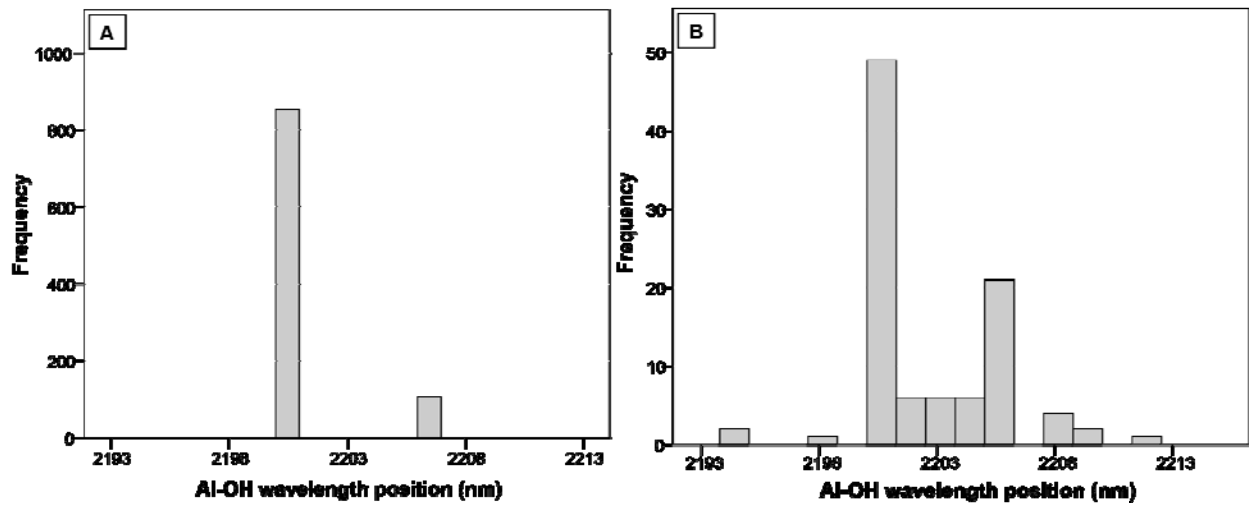


FIGURE 2.9. A) frequency distribution histogram of the Al-OH absorption features of the airborne spectrometry; B) frequency distribution histogram of the Al-OH absorption feature wavelengths extracted from ground spectrometry, re-sampled to the sampling interval of the airborne data.

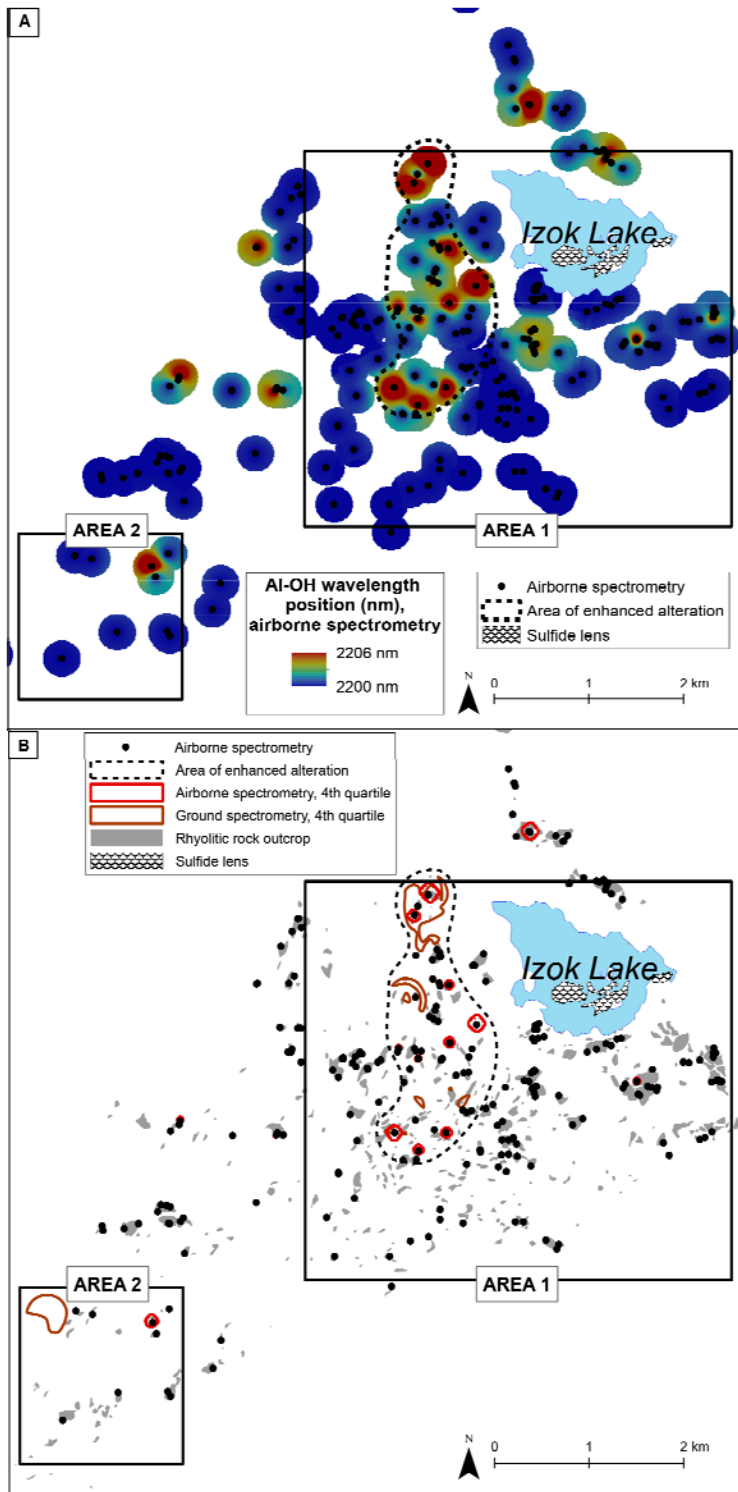


FIGURE 2.10. A) Spatial distribution map of the interpolated Al-OH absorption feature wavelengths extracted from the airborne data; B) spatial distribution map of the 4th quartile of the Al-OH absorption

features extracted from the ground spectrometry (2207-2211 nm) and airborne spectrometry (2205-2206 nm). Also shown in figures A and B is an area of altered rock that is characterized by relatively long Al-OH wavelength positions both in the ground and airborne spectra ("area of enhanced alteration"). Rhyolitic rock outcrops, sulfide lenses, and the outline of Izok Lake GIS data are from Minerals and Metals Group Ltd. (unpubl.).

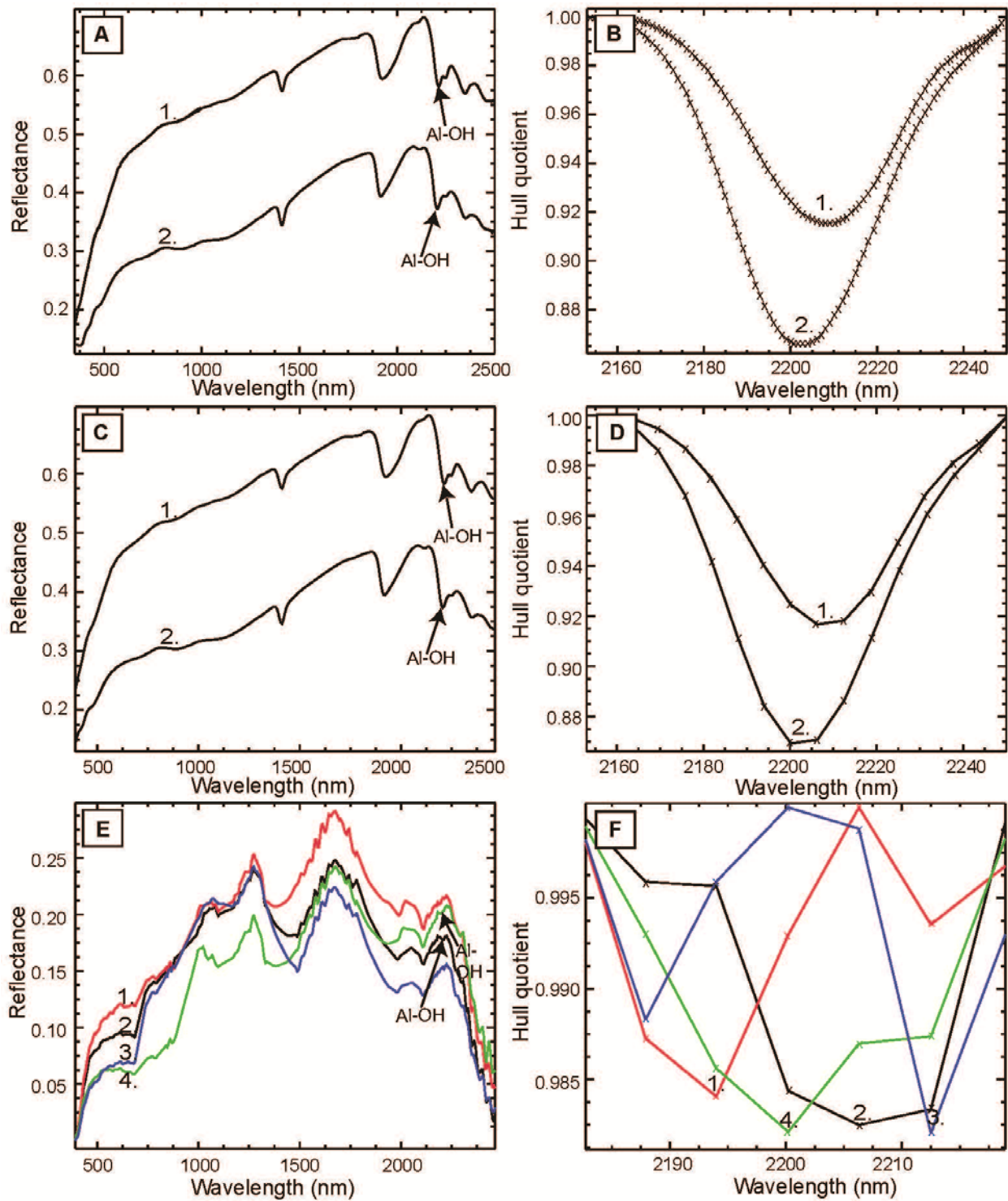


FIGURE 2.11. A) Ground and airborne spectra; A) 1: spectral measurement 267 (2208 nm), 2: spectral measurement 37 (2202 nm); B) hull quotient-corrected spectra 1 and 2 of Figure A; C)

spectral measurements 267 (2206 nm, spectrum 1) and 37 (2200 nm, spectrum 2) shown in Figure A, resampled to the sampling interval of the airborne spectra; D) hull quotient-corrected spectra 1 and 2 of Figure C; E) Airborne spectra 1-4, representing the absorption features near 2194 nm (spectrum 1), 2200 nm (spectrum 4), 2206 nm (spectrum 2) and 2212 nm (spectrum 3); F) hull quotient-corrected spectra 1-4 of Figure E. The sampling interval of the spectra is denoted by "x" in Figures B, D and F.

LITERATURE CITED

- Adams, J. B., Smith, M. O. and Gillespie, A. R., 1993. Imaging spectroscopy: Interpretation based on spectral mixture analysis. In Pieters, C.M. and Englert, P.A., (eds.): Remote geochemical analysis: Elemental and mineralogical composition. Cambridge University Press, Cambridge, UK: 145–166.
- Ager, C. M. and Milton, N. M., 1987. Spectral reflectance of lichens and their effects on the reflectance of rock substrates. *Geophysics* 52: 898–906.
- Barrett, T.J. and MacLean, W.H., 1994. Mass changes in hydrothermal alteration zones associated with VMS deposits of the Noranda area. *Exploration and Mining Geology* 3: 131–160.
- Bassett, W.A., 1960. Role of hydroxyl orientation in mica alteration. *Bulletin of the Geological Society of America* 71: 449–456.
- Bechtel, R., Rivard, B., and Sánchez-Azofeifa, A., 2002. Spectral properties of foliose and crustose lichens based on laboratory experiments. *Remote Sensing of Environment* 82: 389-396.
- Boardman, J.W., 1993. Automating spectral unmixing of AVIRIS data using convex geometry concepts. Summaries of the fourth annual JPL (Jet Propulsion Laboratory) airborne geoscience workshop, JPL publication 93-26, AVIRIS Workshop, v. 1, Washington, USA: 11–14.
- Bostock, H.H., 1980. Geology of the Itchen Lake area, district of Mackenzie. Geological Survey of Canada, Memoir 391, Canadian Government Publishing Centre, Québec.

- Bruegge, C.J., Stiegman, A.E., Rainen, R.A. and Springsteen, A.W., 1993. Use of Spectralon as a diffuse reflectance standard for in-flight calibration of earth-orbiting sensors. *Optical Engineering* 32: 805-814.
- Cathelineau, M., 1988. Cation site occupancy in chlorites and illites as a function of temperature. *Clay Minerals* 23: 471–485.
- Clark, R.N., 1999. Chapter 1: Spectroscopy of rocks and minerals, and principles of spectroscopy. In: Rencz, A.N., (ed.): *Manual of Remote Sensing* 3: 3–58. New York, USA, Wiley.
- Clark, R.N. and Roush, T.L., 1984. Reflectance spectroscopy: quantitative analysis techniques for remote sensing applications. *Journal of Geophysical Research* 89: 6329–6340.
- Clark, R.N., Swayze, G.A., Livo, K.E., Kokaly, R.F., King, T.V.V., Dalton, J.B., Vance, J.S., Rockwell, B.W., Hoefen, T. and McDougal, R.R., 2002. Surface reflectance calibration of terrestrial imaging spectroscopy data. A tutorial using AVIRIS. *Proceedings of the 10th Airborne Earth Science Workshop*, JPL Publication 02-1.
- Clark, R.N., Swayze, G.A., Wise, R., Livo, E., Hoefen, T., Kokaly, R. and Sutley, S.J., 2007. USGS digital spectral library splib06a: U.S. Geological Survey, Digital Data Series 231 (<http://speclab.cr.usgs.gov/spectral.lib06>).
- Cressman, G.P., 1959. An operational objective analysis system. *Monthly Weather Review* 87: 367-374.
- Duke, E.F., 1994. Near infrared spectra of muscovite, Tschermak substitution, and metamorphic reaction progress: Implications for remote sensing. *Geology* 22: 621–624.

- Eberl, D.D., Środoń, J., Lee, M., Nadeau, P.H. and Northrop, H.R., 1987. Sericite from the Silverton caldera, Colorado: Correlation among structure, composition, origin, and particle thickness. *American Mineralogist* 72: 914-934.
- ESRI, 2011. ArcGIS Desktop. Release 10. Redlands, CA: Environmental Systems Research Institute.
- Galley, A., Hannington, M. and Jonasson, I., 2007. Volcanogenic Massive Sulphide Deposits. In Goodfellow, W.D., (ed.): *Mineral Deposits of Canada. A synthesis of major deposit-types, district metallogeny, the evolution of geological provinces, and exploration methods: Geological Association of Canada, Mineral Deposits Division, Special publication 5*: 141–161.
- Gitelson, A. and Merzlyak, M.N., 1994. Spectral reflectance changes associated with autumn senescence of *Aesculus hippocastanum* L. and *Acer platanoides* L. leaves. Spectral features and relation to chlorophyll estimation. *Journal of Plant Physiology* 143: 286–292.
- Government of Canada, 2014. Calculation of the 1971 to 2000 climate normals for Canada. Available at: http://climate.weather.gc.ca/climate_normals/.
- Guidotti, C.V. and Sassi, F.P., 1998. Petrogenetic significance of Na-K white mica mineralogy: Recent advances for metamorphic rocks. *European Journal of Mineralogy* 10: 815–854.
- Herrmann, W., Green, G., Barton, M. and Davidson, G., 2009. Lithochemical and stable isotopic insights into submarine genesis of pyrophyllite-altered facies at the Boco Prospect, Western Tasmania. *Economic Geology* 104: 775–792.
- Hitchcock, R. and White, H.P., 2007. Processing EO-1 Hyperion data using ISDAS, Geomatics, Canada, Technical Note 2, 30 p.

- Hulen, J.B. and Nielson, D.L., 1986. Hydrothermal alteration in the Baca geothermal system, Redondo Dome, Valles Caldera, New Mexico. *Journal of Geophysical Research* 91: 1867–1886.
- Inui, M. and Toriumi, M., 2004. A theoretical study on the formation of growth zoning in garnet consuming chlorite. *Journal of Petrology* 45: 1369–1392.
- Jones, S., Herrmann, W. and Gemmell, J.B., 2005. Short wavelength infrared spectral characteristics of the HW horizon: Implications for exploration in the Myra Falls Volcanic-Hosted Massive Sulfide Camp, Vancouver Island, British Columbia, Canada. *Economic Geology* 100: 273–294.
- Kokaly, R.F., Asner, G.P., Ollinger, S.V., Martin, M.E. and Wessman, C.A., 2009. Characterizing canopy biochemistry from imaging spectroscopy and its application to ecosystem studies. *Remote Sensing of Environment* 113: S78-S91.
- Kranidiotis, P. and MacLean, W., 1987. Systematics of chlorite alteration at the Phelps Dodge massive sulfide deposit, Matagami, Quebec. *Economic Geology* 82: 1898–1911.
- Laidler, G.J., Treitz, P.M. and Atkinson, D.M., 2008. Remote sensing of Arctic vegetation: Relations between the NDVI, spatial resolution and vegetation cover on Boothia Peninsula, Nunavut. *Arctic* 61: 1–13.
- Lentz, D.R. and Goodfellow, W.D., 1993. Petrology and mass-balance constraints on the origin of quartz-augen schist associated with the Brunswick massive sulfide deposits, Bathurst, New Brunswick. *The Canadian Mineralogist* 31: 877-903.
- Li, G., Peacor, D.R., Merriman, R.J. and Roberts, B., 1994. The diagenetic to low-grade metamorphic evolution of matrix white micas in the system muscovite-paragonite in a mudrock from Central Wales. *Clays and Clay Minerals* 42: 369-381.

- Longton, R.E., 1988. *Biology of polar bryophytes and lichens*. Cambridge University Press, Cambridge.
- McLeod, R.L., Gabell, A.R., Green, A.A. and Gardavsky, V., 1987. Chlorite infrared spectral data as proximity indicators of volcanogenic massive sulphide mineralization: Pacific Rim Congress (The Geology, Structure, Mineralisation and Economy of the Pacific Rim), Gold Coast, Australia: 321–324.
- Miyashiro, A. and Shido, F., 1985. Tschermak substitution in low- and middle-grade pelitic schists. *Journal of Petrology* 26: 449–487.
- Morrison, I.R., 2004. Geology of the Izok massive sulfide deposit, Nunavut Territory, Canada. *Exploration and Mining Geology* 13: 25–36.
- Mortensen, J.K., Thorpe, R.I., Padgham, W.A., King, J.E. and Davis, W.J., 1988. U-Pb zircon ages for felsic volcanism in Slave Province, N.W.T.. In: *Radiogenic Age and Isotopic Studies*, report 2. Geological Survey of Canada, Paper 88-2: 85–95.
- Philip, G.M. and Watson, D.F., 1982. A precise method for determining contoured surfaces. *Australian Petroleum Exploration Association Journal* 22: 205-212.
- Post, J.L. and Noble, P.N., 1993. The near-infrared combination band frequencies of dioctahedral smectites, micas, and illites. *Clays and Clay Minerals* 41: 639–644.
- Purvis, W., 2000. *Lichens (Smithsonian's Natural World Series)*. Smithsonian Institution Press, Washington, USA.
- Richter, R. and Schläpfer, D., 2002. Geo-atmospheric processing of airborne imaging spectrometry data. Part 2: Atmospheric/topographic correction. *International Journal of Remote Sensing* 23: 2631-2649.

- Rieder, M., Cavazzini, G., D'Yakonov, Y.S., Frank-Kamenetskii, V.A., Gottardi, G., Guggenheim, S., Koval, P.V., Müller, G., Neiva, A.M.R., Radoslovich, E.W., Robert, J.-L., Sassi, F.P., Takeda, H., Weiss, Z. and Wones, D.R., 1998. Nomenclature of the micas. *The Canadian Mineralogist* 36: 41-48.
- Rivard, B. and Arvidson, R.E., 1992. Utility of imaging spectrometry for lithologic mapping in Greenland. *Photogrammetric Engineering & Remote Sensing* 58: 945–949.
- Rogge, D.M., Rivard, B., Zhang, J., Sanchez, A., Harris, J. and Feng, J., 2007. Integration of spatial-spectral information for the improved extraction of endmembers. *Remote Sensing of Environment* 110: 287–303.
- Scott, K.M. and Yang, K., 1997. Spectral reflectance studies of white micas. Exploration and mining report 439R. CSIRO Division of Exploration and Mining, Australia.
- Settle, J.J. and Drake, N.A., 1993. Linear mixing and the estimation of ground cover proportions. *International Journal of Remote Sensing* 14: 1159-1177.
- Shepard, D., 1968. A two-dimensional interpolation function for irregularly-spaced data. *Proceedings of the 1968 ACM (Association for Computing Machinery) National Conference, New York, USA*: 517–524.
- Sims, D.A. and Gamon, J.A., 2002. Relationships between leaf pigment content and spectral reflectance across a wide range of species, leaf structures and developmental stages. *Remote Sensing of Environment* 81: 337–354.
- Swayze, G.A., Clark, R.N., Goetz, A.F.H., Chrien, T.G. and Gorelick, N.S., 2003. Effects of spectrometer band pass, sampling, and signal-to-noise ratio on spectral identification using the Tetracorder algorithm. *Journal of Geophysical Research* 108, doi: 10.1029/2002JE001975.

- Van Ruitenbeek, F.J.A., Cudahy, T., Hale, M. and van der Meer, F.D., 2005. Tracing fluid pathways in fossil hydrothermal systems with near-infrared spectroscopy. *Geology* 33: 597–600.
- Van Ruitenbeek, F.J.A., Debba, P., van der Meer, F. M., Cudahy, T., van der Meijde, M. and Hale, M., 2006. Mapping white micas and their absorption wavelengths using hyperspectral band ratios. *Remote Sensing of Environment* 102: 211–222.
- Velde, B., 1965. Phengite micas: Synthesis, stability, and natural occurrence. *American Journal of Science* 263: 886-913.
- Yang, K. and Huntington, J.F., 1996. Spectral signatures of hydrothermal alteration in the metasediments at Dead Bullock Soak, Tatami desert, Northern Territory: Exploration and mining report 270R. CSIRO Division of Exploration and Mining, New South Wales, Australia.
- Yang, K., Huntington, J.F., Gemmell, J.B. and Scott, K.M., 2011. Variations in composition and abundance of white mica in the hydrothermal alteration system at Hellyer, Tasmania, as revealed by infrared reflectance spectroscopy: *Journal of Geochemical Exploration* 108: 143–156.

CHAPTER 3 - Short-wave infrared (SWIR) spectral and geochemical characteristics of hydrothermal alteration at the Archean Izok Lake Zn-Cu-Pb-Ag volcanogenic massive sulfide deposit, Nunavut, Canada: application in exploration target vectoring

3.1 INTRODUCTION

The genetic model for volcanogenic massive sulfide (VMS) deposits is one of the best constrained of all ore deposit types, and has been developed over the last five decades. The model has been substantially refined by the discovery and study of modern seafloor massive sulfide deposits. VMS deposits develop in various tectonic settings where there is rifting and high heat flow that initiate hydrothermal circulation of seawater through rock strata in the subsurface (Galley et al. 2007). The processes by which host rocks to VMS deposits are altered are reasonably well constrained, based on theoretical and experimental studies on ancient and modern deposit studies (e.g. Large 1977, Seyfried et al. 1988, Gemmell and Large 1992, Galley 1993, Goodfellow and Peter 1994, Ohmoto 1996). At the onset of VMS deposit formation, cold seawater is drawn into the upper parts of the crust, which results in the establishment of a convective cell of circulating hydrothermal fluids. As the fluid temperature increases and pH concomitantly decreases, metals are leached from the host rocks. The dissolved metals are transported upward and precipitated at or near the seafloor when the hydrothermal fluids mix with cold seawater. A key geochemical reaction along the fluid flow path is the breakdown of feldspars through interactions with the acidic hydrothermal fluids, and the subsequent formation

of white micas and chlorite (Barrett and MacLean 1994). Here, white micas refer to dioctahedral phyllosilicate minerals that display a solid solution between paragonite-muscovite and muscovite-phengite (Velde 1965). Many VMS systems (i.e. the entire footprint of the deposit, including subtle textural, geochemical, mineralogical, and mineral chemical features imparted on the host rocks) have two distinct alteration styles: 1) primarily chlorite-altered, typically centered on the core of the fluid upflow zone, and 2) sericite-altered, typically outboard of (peripheral to) the chlorite-altered zone (Franklin 1986).

Although the most intense hydrothermal alteration (high temperatures of 300-400 °C and high water/rock ratios; Barrett and MacLean 1994) is commonly manifest within the core of the paleofluid upflow zone, more subtle (less intense) alteration effects occur outboard of this, and their recognition can aid in vectoring toward mineralization in an exploration program. Vectoring methods include the recognition and quantification of the enrichment and depletion of selected elements, such as Na, Ca and K (Stephens et al. 1984). Bulk rock sodium depletion is documented in the vicinity of practically all VMS deposits (Franklin 1997), and several studies (see Franklin et al. 1975 and references therein) have mapped the spatial variability of this depletion to serve as a proxy for alteration intensity variability throughout a study area. Alteration indices, such as the commonly used Ishikawa alteration index (hereafter referred to AI; Ishikawa et al. 1976) and the chlorite-carbonate-pyrite index (CCPI; Large et al. 2001), offer a more sophisticated way of quantifying alteration intensity by tracking multiple geochemical and mineralogical parameters; both are defined below. The AI simultaneously measures the depletion (Na_2O and CaO) and enrichment (MgO and K_2O) of alkaline-earth and alkali metal oxides that are indicative of the formation of white mica and chlorite. One disadvantage of the AI is that it

does not consider carbonate alteration, which can be significant in some VMS deposits (Large et al. 2001). To overcome this limitation, Large et al. (2001) devised the chlorite-carbonate-pyrite index (CCPI) that quantifies the abundance of chlorite through FeO and MgO enrichment and Na₂O and K₂O depletion. Both the AI and the CCPI range between 0 and 100%, such that the maximum value represents complete replacement of feldspar and volcanic glass by white micas, chlorite, or both.

Conventional methods of determining the chemical compositions of rocks and minerals are time-consuming, laborious and costly (e.g. whole rock and electron microprobe analysis). A rapid and non-destructive alternative to these methods is optical remote sensing. Many phyllosilicate minerals are infrared-active, and can be identified using their characteristic absorption features in the short-wave infrared wavelength region. More specifically, muscovite has a pronounced Al-OH absorption feature near 2200 nm, and chlorite group minerals have an Fe-OH absorption feature near 2260 nm (Hunt and Salisbury 1970). The Fe-OH absorption feature is also present in biotite (Post and Noble 1993), which can develop under regional metamorphism or hydrothermal circulation (Pirajno 2009). The wavelength position of these absorption features are documented to shift as a function of compositional changes that take place under changing chemical and temperature gradients within a VMS system (Herrmann et al. 2001, Jones et al. 2005). High temperatures favor a simultaneous decrease in the Mg and Fe content and an increase in the Al content of white mica (Duke 1994). Moreover, the Fe contents of chlorite and biotite can increase with formation at higher temperatures (Miyashiro and Shido 1985, Cathelineau 1988). However, other factors such as pressure, hydrothermal fluid chemistry, water/rock ratios and the composition of the host rocks can all simultaneously influence the

chemical composition of the phyllosilicate minerals (Velde 1967, Kranidiotis and MacLean 1987). The chemical compositional changes that take place as a result of these processes are reflected in the wavelength position of the Al-OH absorption feature, which shifts toward shorter wavelengths as the Al content of the octahedral sites of the mineral increase, and the opposite effect, or a shift toward longer wavelengths, takes place when the Mg and Fe contents of the octahedral sites increases (Post and Noble 1993, Duke 1994). Similarly, the hydroxyl absorption features of biotite and chlorite shifts toward shorter wavelengths with increasing Mg, and toward longer wavelengths with increasing Fe (Bassett 1960, McLeod et al. 1987).

The chemical compositions of the phyllosilicate alteration minerals are partly controlled by the physicochemical parameters of the altering fluid. However, because multiple factors can simultaneously influence the chemical composition of the alteration minerals, and these factors vary in different parts of a single deposit and across different deposits, a range of mineral compositions are possible. Some studies document compositional trends (within upflow alteration zones) that can be contradictory to the generalized ideal model of Fe-rich compositions in the proximal upflow zone. For example, although Fe-rich chlorite has been documented in the vicinity of massive sulfide lenses (e.g., Plimer and de Carvalho 1982, MacLean and Hoy 1991, Çağatay 1993, Leistel et al. 1998), other studies have documented Mg-chlorite in these areas (e.g., Nesbitt 1982, Costa et al. 1983, Date et al. 1983, Urabe et al. 1983, McLeod et al. 1987, Schmidt 1988, Sánchez-España et al. 2000, Paulick et al. 2001, Hannington et al. 2003, Biel et al. 2010). Regardless of the chemical composition of chlorite, altered rocks in the proximal fluid upflow areas can have white micas that are either predominantly Al-rich (e.g., Urabe et al. 1983, Jones et al. 2005, Herrmann et al. 2009) or Al-poor (e.g., Plimer and de Carvalho 1982, MacLean

and Hoy 1991, Biel et al. 2010). For these reasons, it is difficult to estimate the hydrothermal alteration intensities of hydrothermal alteration in and around a VMS deposit based solely on the chemical composition of its phyllosilicate minerals.

Many studies have documented the lithogeochemical variability of the host rocks of VMS deposits, and during the last few decades, optical spectroscopy has been increasingly used to infer the mineralogical and mineral chemical properties of alteration and gangue minerals in different metallic mineral deposit types. Nevertheless, most of the studies related to VMS deposits have not linked spectral characteristics with lithogeochemical, mineralogical or mineral chemical data.

Herein, we investigate the relationship between bulk rock compositions and the spectral properties of the phyllosilicate minerals (biotite, chlorite and white mica) collected from outcrops and drill cores in the hydrothermal alteration zones of the Izok Lake Zn-Cu-Pb-Ag VMS deposit, Nunavut, Canada, one of the largest undeveloped Zn-Cu deposits in North America, with the aim of developing methodologies that can be used to vector toward concealed mineralization here and elsewhere. This is a continuation to the investigation of Chapter 1 that examined the detection of hydrothermally altered rocks at Izok Lake using airborne hyperspectral and ground spectrometric data from outcrops.

3.2 STUDY AREA

Izok Lake (65°38'N, 112°48'W, Figure 1) is a Zn-Cu-Pb-Ag VMS deposit located in the Kitikmeot region of Nunavut, Canada. The total resource presently stands at 14.4 million tonnes grading 2.52% Cu, 12.94% Zn and 71 g/t Ag (MMG Ltd. 2011). The Izok Lake deposit is within the Point Lake formation, a succession of felsic and mafic metavolcanic rocks that belong to the

Yellowknife supergroup of the Slave structural province. The deposit is comprised of five polymetallic, massive to semi-massive lenses of sphalerite, pyrite, chalcopyrite and galena hosted by Archean (2.6 Ga) rhyolitic rocks that are regionally metamorphosed to pyroxene hornfels grade (Mortensen et al. 1988, Morrison and Balint 1993). These rhyolitic rocks are the immediate footwall host to most of the massive sulfide mineralization, and are variably (in places intensely) altered (Morrison 2004), and for this reason, all of our spectral measurements and geochemical data are focused exclusively on the rhyolitic rocks. The hydrothermal alteration is manifested by an inner core of chlorite alteration that is surrounded by a broad zone of sericite alteration (Morrison 2004). The inner alteration zone is characterized by Mg-enrichment and the mineral assemblage chlorite-biotite-cordierite (Money and Heslop 1976). The immediate hangingwall rocks (rhyolite, with andesite in some places) are sodium-depleted and contain widespread muscovite, biotite and sillimanite (Morrison 2004). These hydrothermally altered units are overprinted by younger Ca-metasomatism, which is evidenced by a wide range of CaO contents that span from trace amounts to over 11 wt% (Morrison 2004).

3.3 SAMPLING AND METHODS

3.3.1 Ground spectra site selection and measurement

The hydrothermal alteration zones were delineated on surface by collecting 455 spectral measurements and 60 samples (Fig. 3.1) from the rhyolitic rock outcrops of the study area during fieldwork conducted in summer 2010 and 2013. All measurements were obtained using a contact probe that has an internal illumination source that ensures consistent illumination conditions during data acquisition. This probe was attached to a PANalytical Boulder Inc. FieldSpec

(abbreviated hereafter as "ASD") 3 spectrometer that records spectra in the 350-2500 nm wavelength range with a spectral resolution of 10 nm and a sampling interval of 1 nm in the short-wave infrared (SWIR; 1300-3000 nm) wavelength region. The rationale for site selection and further technical description of data acquisition are provided in Chapter 2. The raw at-sensor radiance values were then converted to surface reflectance values by means of a SpectralonTM reflectance panel (i.e. the "white reference", SRT-99-100, Labsphere, Inc., North Sutton, NH, USA), a commercially available plate made of polytetrafluoroethylene (Bruegge et al. 1993). These relative reflectance values were converted to absolute reflectance values by multiplying the relative reflectance value of each wavelength with the reflectance factor obtained from the calibration certificate of the SpectralonTM panel. This correction was conducted in accordance with the procedure suggested by Clark et al. (2002).

3.3.2 Drill core sampling and laboratory spectral measurements

In order to establish the character and extent of the hydrothermal alteration zones of the Izok Lake deposit in the third dimension, spectrometric data were obtained from 28 drill cores (Fig. 3.1). These measurements were made with a contact probe at an average spacing of 5.5 m, resulting in 781 spectral readings from all lithologies intersected in drilling. These measurements were acquired with two spectroradiometers: an ASD FieldSpec 3 spectrometer and a TerraSpec 4 Hi-Res Mineral spectrometer. Each spectrum acquired from the drill cores consists of 60 individual measurements taken consecutively and averaged by the instrument. Conversion of radiance to reflectance was as described for ground spectral measurements and only the drill core spectra that were acquired from the rhyolitic rock units were analyzed.

In addition to acquiring spectral measurements, a visual estimate of the hydrothermal alteration intensity was recorded for a subset of eight drill cores (HEN-172, HEN173, HEN-197, HEN-198, HEN-212, HEN-273, HEN-309 and HEN-340) that comprise a cross-section through a central massive sulfide lens. For this subset, each spectral measurement has an associated alteration intensity value that ranges from weak, to moderate, to intense, based on the textural and mineralogical properties of the rock. These visually estimated alteration intensity estimates were then assigned numeric values, with 1 indicating weak alteration, 2 representing moderate alteration, and 3 representing intense alteration.

3.3.3 Bulk geochemical analytical techniques

Of the 781 spectra acquired from the drill cores 624 were from rhyolitic rocks and these were investigated to delineate the vertical extent of hydrothermal alteration and document any zonation present. In the case of the ground spectrometry, fifty spectral measurements out of 455 had to be discarded because of low signal-to-noise ratios. The remaining 405 spectra and the 624 drill core spectra were hull-corrected to minimize the effects of background absorption (Clark 1999), and the hull quotient minima of the Al-OH and Fe-OH absorption features were estimated manually. Drill core spectra were grouped together with ground spectra to achieve maximum sample coverage throughout the study area. In practice, each drill core (HEN-172, HEN-173, HEN-186, HEN-187, HEN-188, HEN-192, HEN-205, HEN-234, HEN-309, HEN-336, HEN-378 and HEN-400) was assigned one Al-OH and Fe-OH absorption feature position if either absorption feature was encountered at a maximum depth of 10 metres below surface. If more than one drill core spectrum is within this depth range, the one closest to the surface (between 3.1 m and 10 m deep) was chosen for further processing to ensure comparability between ground and

drill core spectra. The spatial trends of the Al-OH and Fe-OH absorption feature wavelength positions were then visualized by means of Kriging interpolation (Oliver and Webster 1990) using the nearest 10 values to calculate the contents of each pixel in the continuous surface. Circular buffer zones of 300 m radius were then created around each Al-OH and Fe-OH absorption feature observation, and the interpolated surfaces were cropped to the dimensions of these buffer layers. This diameter was estimated using the average and maximum Euclidean distances between adjacent field observations for the Al-OH (average: 87 m, maximum: 383 m) and Fe-OH (average: 105 m, maximum: 1333 m) features respectively. The 300 m radius was estimated based on these average and maximum distances to minimize extrapolation and to create a realistic representation of the spatial trends of the absorption feature wavelength positions in the study area.

In a separate analysis, the Euclidean distance between the Al-OH and Fe-OH absorption feature observations of the drill cores and their spatially nearest massive sulfide lenses was calculated to investigate possible changes in the spectral properties of the white micas and biotite/chlorite with distance to the mineralization. The locations and spatial dimensions of the massive sulfide lenses were extracted from the drill core logs of MMG. In the case of ground spectra, the horizontal distance between the measurement locations and the nearest massive sulfide lens (see Figure 3.1) was calculated. Finally, all measured distances were combined to obtain a three-dimensional model of the spatial variation of the Al-OH and Fe-OH absorption feature wavelength positions.

3.3.4 Mineralogy and mineral chemistry

A database of whole rock major element oxide analyses of 2902 rock samples collected from outcrops at an average sampling density of 43 m was provided by Minerals and Metals Group Ltd. (MMG). These samples are from intensely altered areas proximal to mineralization and less altered areas distal to mineralization. This database was supplemented by a similar database of 151 drill core samples (NQ core, 4.5 cm diameter, each 15 to 20 cm long) collected at 28 m intervals down hole. The drill core samples are mainly from an intensely altered area proximal to mineralization. The locations of the surface samples and drill cores are shown in Figure 3.1.

For the whole rock major element oxide analyses, the samples were crushed, split and powdered using a hardened steel mill. Powdered samples (0.2 g) were added to lithium metaborate/lithium tetraborate flux (0.9 g), mixed and fused in a furnace at 1000 °C. This was then cooled and dissolved in 100 mL of 4% nitric acid/2% hydrochloric acid. This solution was analyzed by Inductively Coupled Plasma-Atomic Emission Spectroscopy (ICP-AES). The results were corrected for spectral inter-element interferences. Oxide abundances were calculated from the determined elemental contents with 0.01% and 100% lower and upper limits, respectively.

3.3.5 Lithochemical data treatment

The lithochemical database was used to identify large-scale hydrothermal alteration variations across the study area. First, the outcrop samples were restricted to rhyolitic rocks (shown in Figure 3.1) and of the remaining 1263 analyses, 22 were removed because of missing data. The remaining 1241 analyses were used to calculate the Ishikawa index (AI, Ishikawa et al. 1976):

$$AI = 100(K_2O + MgO)/(K_2O + MgO + Na_2O + CaO).$$

The calculated AI values were spatially linked to corresponding ground spectral measurements of the rhyolitic rocks to investigate the relationship between the Al-OH and Fe-OH wavelength positions and intensity of hydrothermal alteration. This was achieved by horizontally joining each Al-OH and Fe-OH absorption feature in the ground spectra with the AI value calculated from its geographically nearest lithochemical analysis. The AI was used as a measure of alteration intensity due to the predominantly white mica-rich nature of the rhyolitic rocks surrounding the massive sulfide lenses.

In order to explore the relationships between the Al-OH and Fe-OH absorption features and alteration intensity in a vertical (depth) sense, 122 drill core whole rock analyses of the rhyolitic rocks were correlated with their nearest Al-OH and Fe-OH absorption features in the drill core spectra. The alteration intensity was estimated by means of the AI and chlorite-carbonate-pyrite index (CCPI) using the following formula (Large et al. 2001):

$$CCPI = 100(FeO + MgO)/(FeO + MgO + K_2O + Na_2O).$$

The AI and CCPI alteration index values ($n=122$) were then combined with their spatially nearest visually estimated alteration intensity (VEAI) values ($n=172$). Only VEAU values for the rhyolitic rock units were included in this analysis. If the down-hole distance between the AI/CCPI and the VEAU values was greater than five metres, no VEAU value was assigned to an AI/CCPI value.

The AI and CCPI values were next compared with the Al-OH and Fe-OH absorption features for the drill core rhyolitic rocks with the objective of associating the wavelength position shifts with the vertical hydrothermal alteration intensity variation. Due to the different sampling

intervals of the analytical and spectral results, the latter were linearly interpolated to the nearest whole rock geochemical analysis. The Al-OH and Fe-OH absorption feature wavelength positions situated immediately down-hole and up-hole from the geochemical analysis were used to calculate the interpolated Al-OH/Fe-OH absorption feature wavelengths. If interpolation was not possible due to a missing value either below or above a particular geochemical analysis, no extrapolation was performed, and the analysis was not assigned a corresponding Al-OH/Fe-OH absorption feature wavelength value. No correlations were done for drill cores HEN-258, HEN-418 and HEN-444 because no geochemical data were available.

Finally, the Kriging interpolation technique (Oliver and Webster 1990) was used to map the spatial distribution of the alteration intensity values in the study area. The nearest 10 alteration intensity values, estimated by means of the AI, were used to calculate the content of each pixel in the interpolation surface. In order to estimate the alteration intensity variation of the study area using a maximal number of observations, the vertical alteration index values of the drill core database were combined with the horizontal alteration index values extracted from the surface samples. This analysis was constrained to the vertical alteration index values from a maximum depth of 10 m so that the vertical AI values would be comparable with the horizontal AI values. For this same reason, AI was used to estimate the hydrothermal alteration intensity both vertically and horizontally. Drill cores HEN-172, HEN-173, HEN-192, HEN-198, HEN-234, HEN-252, HEN-356 and HEN-400 are used in this analysis because they have lithochemical data in the chosen depth range (~2-10 m).

3.3.6 Mineralogy and mineral chemistry

The relationships between the Al-OH and Fe-OH absorption features and the minerals present in the samples were studied by petrographic analysis of six polished thin sections (PTS) using a transmitted polarizing light microscope. The samples were selected based on the presence of an Al-OH or an Fe-OH absorption feature, or both. The PTS of the samples were examined under a Nikon Labophot2[®] polarizing light microscope and the presence or absence of biotite, chlorite and muscovite was recorded at over 500 random spots within each PTS (see Chapter 2 for details).

The electron microprobe analyses of seven PTS were conducted in order to investigate the relationship between the Al-OH and Fe-OH absorption feature wavelength shifts and the compositions of muscovite, biotite and chlorite. The samples were selected for electron microprobe analysis (EMPA) based on the short, intermediate and long wavelength positions of their Al-OH and Fe-OH absorption features. The PTS were carbon-coated and analyzed using a JEOL 8230 SuperProbe[®] electron microprobe. Mineral formulae were calculated on the basis of 22 oxygens for micas (white micas and biotite) and 28 oxygens for chlorite. The mineral cation compositions were then compared to the average Al-OH and Fe-OH absorption feature wavelength positions of the same samples from which the PTS were prepared (see Chapter 2 for details).

3.4 RESULTS

3.4.1 Frequency distribution of Al-OH and Fe-OH absorption features

The Al-OH and Fe-OH absorption features of the ground and drill core datasets show a wide range of absorption feature wavelength positions suggestive of considerable chemical compositional variation within the phyllosilicate minerals. Based on the petrographic analysis of the thin sections, the Al-OH absorption features are associated with the white micas and the Fe-OH absorption features are associated with biotite/chlorite (see Chapter 2 for details). Furthermore, the EMPA results indicate that the Al-OH absorption features of the white micas shift toward shorter wavelengths with increasing Al, and toward longer wavelengths with increasing Mg+Fe (see Chapter 2 for details). Similarly, the Fe-OH absorption features of biotite/chlorite shift toward shorter wavelengths within increasing octahedral Mg, and toward longer wavelengths with increasing octahedral Fe. Figures 3.2A-D illustrate these absorption feature wavelength shifts using four drill core spectra as examples.

Next, the statistical properties of the ground and drill core datasets were assessed by computing their minimum, maximum, median and mode (Table 3.1) with the objective of analyzing possible differences in the Al-OH and Fe-OH absorption feature wavelength positions of these datasets. The Al-OH and Fe-OH absorption feature wavelength position frequency distributions are shown in Figures 3.3A-D. These results show that both the mode and median of the Al-OH and Fe-OH absorption feature wavelength positions are at shorter wavelengths in the drill core spectral dataset than in the ground spectral dataset, indicating that the chemical properties of the phyllosilicate minerals of these datasets may not be identical. Moreover, the wavelength ranges of the Al-OH and Fe-OH absorptions are wider for the drill core spectra than

the ground spectra, suggesting different environmental (chemical and temperature) conditions at the time of massive sulfide formation.

Next, the frequency distributions of the Al-OH and Fe-OH absorption feature wavelengths were compared to the normal distribution using the Kolmogorov-Smirnov test. This test reveals that the Al-OH and Fe-OH wavelength positions of the ground and drill core spectra are not normally distributed ($p=0.000$). The non-normal data distributions of the ground and drill core hyperspectral datasets are also expressed as asymmetry in the frequency distributions of the data sets, which are all positively skewed (Fig. 3.3). All data sets, with the exception of the ground spectra Fe-OH absorption feature wavelengths, have outliers that are more than three standard deviations from the sample mean. The skewed data distributions and the presence of outliers in the data sets necessitated the use of non-parametric statistical methods, specifically Spearman's rank correlation analysis (rather than Pearson's) for determining the relationships between the hyperspectral and lithochemical datasets, discussed in sections 3.4.3 and 3.4.4.

3.4.2 Evaluation of geochemical indicators of alteration intensity of the drillcore dataset

Figure 3.4A,B displays bivariate plots of the visually estimated alteration intensity (VEAI) of the drill cores versus the calculated chlorite-carbonate-pyrite index (CCPI) and the calculated Ishikawa index (AI). Correlations between the VEAU and the AI and CCPI values were calculated using the Spearman's rank correlation coefficient due to the non-normal distributions of all three data sets and the small sample size (<30). There is a statistically significant (Spearman's $\rho=0.494$, $n=24$, $p=0.14$, 95% confidence level, one-tailed) correlation between the CCPI and the VEAU; however, there is no statistically significant correlation between the AI and the VEAU. These results suggest that the CCPI shows systematic variation with the visually observable

alteration intensity parameters (textural and mineralogical) of the drill cores whereas the AI does not. Hence the CCPI was chosen (over the AI) to assess the relationship between the alteration intensity and the Al-OH and Fe-OH wavelength positions of the drill core samples.

3.4.3 Relationships between drill core spectral and geochemical indicators

A comparison between the CCPI and the Al-OH/Fe-OH absorption feature wavelengths of the drill cores (Fig. 3.5A,B) shows that as the alteration intensity increases, there is a systematic shift of the Al-OH absorption feature toward shorter wavelengths and a concomitant shift of the Fe-OH feature towards longer wavelengths. Specifically, there is a weak, negative correlation (Spearman's $\rho=-0.333$, $n=122$, $p=0.000$, 99% confidence level, two-tailed) between the wavelengths of the Al-OH absorption features and the CCPI and a weak, positive correlation between wavelengths of the Fe-OH absorption feature and the CCPI (Spearman's $\rho=0.252$, $n=122$, $p=0.013$, 95% confidence level, two-tailed).

The vertical alteration intensity variation was examined further by selecting for study seven drill cores (HEN-172, HEN-173, HEN-197, HEN-262, HEN-273, HEN-309 and HEN-340) which lie along a planar section. These drill holes comprise a vertical section through the collars of the central massive sulfide lenses of the Izok Lake deposit, and Figure 3.6 displays the interpolated values for Cu, Zn, CCPI, Al-OH absorption feature wavelength position and Fe-OH wavelength position (Fig. 3.6A-E). These interpolations were created by estimating the value of each voxel node (three-dimensional cell) using the value of the nearest drill core observation (i.e. the "nearest neighbor"). The highest Cu and Zn values (Figs. 3.6A,B) occur near 100 and 150 metres of the surface. The high Cu values apparent in Figure 3.6A represent a feeder zone to the

upper massive sulfide lens that is not clearly expressed in this cross section. The central areas of the Izok Lake deposit are in general characterized by a lower Cu-rich zone that transitions to an upper Zn-rich zone (Morrison 2004). These complexly zoned areas are characterized by high (80-96%) CCPI values in the immediate vicinity of the Cu-rich massive sulfide lens that gradually display lower CCPI values (46-60%) toward the surface (Fig. 3.6C). The results also illustrate the inverse correlation between the CCPI values and the Al-OH absorption feature wavelength positions (Fig. 3.6D). The correlation between the spatial distribution of the CCPI and the Fe-OH absorption feature wavelength positions is not as readily apparent (Fig. 3.6E). The holes were drilled in the immediate vicinity of the massive sulfide lenses (Fig. 3.6F), and hence the results are obtained from the intensely altered rocks, as also suggested by the high CCPI values.

3.4.4 Relationships between ground spectral and geochemical indicators

The relationship between the bulk rock compositions and hyperspectral data was assessed by comparing the AI values listed in Appendix A with the Al-OH absorption feature wavelength positions of the ground spectra. Here, the AI (as opposed to the CCPI) was used as a measure of alteration intensity due to the predominantly sericitic alteration of the rhyolitic rocks surrounding the massive sulfide lenses. The Spearman rank correlation analysis suggests that there are no statistically significant relationships between the Al-OH absorption feature wavelength positions and AI. Contrary to this, there is a positive correlation between the Fe-OH absorption feature wavelength positions and the AI (Spearman's $\rho=0.238$, $n=264$, $p=0.000$, 99% confidence level, two-tailed, Fig. 3.7A). This relationship was further explored by comparing the Fe-OH wavelength positions of the ground spectra to the bulk rock Na₂O content. There is a weak, statistically significant inverse correlation between these two parameters (Spearman's $\rho= -$

0.274, $n=264$, $p=0.000$, 99% confidence level, two-tailed, Fig. 3.7B), supporting the findings, discussed above, that intense alteration intensity is associated with a shift toward longer Fe-OH absorption feature wavelength positions. These results suggest that the Fe-OH absorption feature wavelength positions are associated with the alteration intensity of the study area, providing a vector toward the massive sulfide lenses of the Izok Lake mineralization.

3.4.5 Regional map patterns of the Al-OH and Fe-OH absorption feature positions

The spatial distributions of the Al-OH and Fe-OH absorption feature wavelength positions, extracted from the combined ground and drill core spectra, display spectral shifts proximal to mineralization (Fig. 3.8) in rocks with abundant phyllosilicate minerals. The proximal areas within 500 m of mineralization are characterized by relatively short Al-OH and Fe-OH absorption feature wavelength positions, whereas more distal areas (between 500 and 2400 m from mineralization) display a spectral shift toward longer wavelength positions in both data sets (Figs. 3.8A,B). There are no obvious spectral gradients in the Al-OH absorption feature wavelength positions in the most distal areas (between 5700 and 6800 m from mineralization), contrary to the Fe-OH absorption feature wavelength positions that show a spectral shift toward shorter wavelength positions in these areas. These spectral trends are associated with the AI variation (Fig. 3.8C), which is characterized by relatively high to moderate alteration intensity values in the proximal areas (0-500 m from the massive sulfide lenses), and very high alteration intensity values in the immediate vicinity (500-2400 m) of the massive sulfide lenses. The alteration intensity values gradually become less intense in the distal areas (5800-6900 m from the massive sulfide lenses).

The spatial distributions of the Al-OH and Fe-OH absorption feature wavelength positions extracted from the ground and drill core spectra were further assessed by examining their correlation with distance to the nearest massive sulfide mineralization. Bivariate plots, shown in Figures 3.9A-B, suggest that rocks within 500 m of massive sulfide mineralization display considerable variation in the Al-OH and Fe-OH wavelength positions. In general, Figure 3.9A shows a lack of systematic spatial trends in the Al-OH absorption feature wavelength positions as a function of distance to the mineralization, discussed above. Contrary to this, the Fe-OH absorption feature wavelength positions display a shift toward longer wavelengths between 500 and 2400 m from mineralization, and a shift toward shorter wavelengths furthest (between 5800 and 6900 m) from mineralization.

3.5 DISCUSSION

3.5.1 Spectral characteristics of white micas and biotite/chlorite

The wavelength positions of the Al-OH absorption features of the ground and drill core spectra range continuously from 2194 nm to 2216 nm. According to Herrmann et al. (2001), this wavelength range suggests that the chemical composition of the white micas ranges from sodic (paragonitic, or: high octahedral Al) to potassic to phengitic (low octahedral Al) muscovite. Similarly, the positions of the Fe-OH absorption feature wavelengths, associated with biotite and chlorite, display a wide and continuous range from 2244 nm to 2260 nm. Jones et al. (2005) suggested that this wavelength range represents chemical compositional variability from Mg-rich to Fe-rich chlorite in the short and long end of the wavelength range, respectively.

The spectral variation of the Izok Lake deposit is expressed as significant vertical spectral

variation in the immediate vicinity of the massive sulfide lenses (Fig. 3.9A,B), possibly induced by intense hydrothermal alteration at fluctuating temperature and chemical gradients. The vertical alteration intensity variation, measured by means of the CCPI, is expressed as relatively weak alteration intensity near the surface and intense alteration in the immediate vicinity of massive sulfide mineralization approximately a hundred metres below the surface. This observation can be explained through progressively higher temperatures at depth at the time of hydrothermal alteration, and later deformation that may have changed the stratigraphic position of the upflow zone.

In the drill core spectra, the white micas in the immediate vicinity of the massive sulfide lenses (0-500) have short Al-OH wavelength positions, whereas those farther away from the lenses (500-2400 m) have relatively long Al-OH wavelength positions. The spectral characteristics of the latter alteration zone (near 500-2400 m) were interpreted to suggest a marginal discharge area that contains phengitic muscovite (see Chapter 2 for details). This alteration zone is associated with intense hydrothermal alteration (Fig. 3.8C), suggestive of high temperatures and high water/rock ratios at the time of deposit formation. The alteration intensity values decrease further away and the Al-OH wavelength positions shift to slightly shorter wavelengths, consistent with a less celadonic white mica composition in the distal areas. However, the Al-OH wavelength positions, associated with the chemical composition of the white micas, lack systematic trends with respect to distance from mineralization.

Contrary to the spatial patterns of the Al-OH absorption features of the white micas, the Fe-OH wavelength positions of biotite/chlorite display a well-defined vector to mineralization in the Izok Lake deposit area. The spatial patterns of the positions of the Fe-OH absorption feature

wavelengths can be summarized as follows: the most proximal alteration is characterized by relatively short Fe-OH absorption feature wavelength positions, whereas the immediate outer zone (500-2400 m) of the deposit shows a shift toward longer Fe-OH absorption feature wavelength positions. In the distal areas (> 2400m) there is a shift toward shorter Fe-OH absorption feature wavelengths. These findings can be interpreted as follows: an intense alteration in the proximal areas is characterized by Mg-rich biotite/chlorite, whereas the immediate outer zone has intermediate to Fe-rich biotite/chlorite, while areas beyond also contain more Mg-rich biotite/chlorite.

As with the white micas, considerable vertical spectral variation takes place in biotite/chlorite in the immediate vicinity of the massive sulfide lenses (Fig. 3.9B). Furthermore, the spatial dimensions of the region with long Fe-OH absorption feature wavelength positions in the immediate outer zone to the mineralization (500-2400 m) approximates the spatial dimensions of the phengitic alteration zone discussed above. Similar trends to those present in the chemical compositional variety of the white micas and biotite/chlorite group minerals of the Izok Lake deposit have been reported from other VMS deposits such as the South Bay deposit in Ontario, Canada (Urabe et al. 1983), Ambler mineral district in Alaska (Schmidt 1988) and Iberian Pyrite Belt in Spain (Sánchez-España et al. 2000).

3.5.2 Correlations between the spectral absorption features and the bulk rock compositions

The AI was originally devised to measure the intensity of alteration in predominantly felsic volcanic rocks of the Kuroko deposits in Japan. Subsequently, the index has been applied from intermediate to mafic rocks (Gemmell and Large 1992), indicating robustness independent

of lithologic variation. The CCPI measures the enrichment of FeO and MgO, both of which are abundant in mafic and ultramafic rocks. Thus, lithologic variation may influence CCPI values in mixed lithologies. In our study, lithologic variation plays a minimal role, because care was taken to analyze only the lithochemical and spectral results obtained from rhyolitic rocks. The CCPI was chosen over the AI for estimating the alteration intensity variation of the downhole section because a comparison between the AI and VEAI failed to produce statistically significant results, contrary to the comparison between the CCPI and VEAI. These results indicate that the CCPI follows the hydrothermal alteration intensity variation of the downhole proximal areas of the Izok Lake deposit more closely than the AI. The CCPI was originally devised to measure the alteration intensity of the inner alteration zones of VMS deposits that are often typified by chloritic alteration, which can also have significant carbonate alteration (Large et al. 2001). Such alteration has been observed in the vicinity of the massive sulfide lenses of Izok Lake (Morrison 2004), and hence the nature of hydrothermal alteration in these areas can explain the result.

The weak, negative correlation between the Al-OH absorption feature wavelengths of the drill core spectra and the CCPI indicate that an increasing alteration intensity is associated with increasingly Al-rich white micas. In accordance with our results, Yang et al. (2011) documented a similar correlation for the Hellyer VMS deposit (Tasmania) between the Al-OH absorption feature wavelength positions of andesitic rocks and the AI, albeit the statistical significance of their noted positive correlation was not reported. Contrary to the drill core spectra, no statistically significant correlations were found between the Al-OH absorption feature wavelength positions of the ground spectrometry and the alteration intensity on surface, as measured by the AI, possibly due to the smaller sample size of the ground spectral dataset that did not allow for a

possible correlation between the two datasets to be observed.

A comparison between the Fe-OH wavelength positions of the spectral datasets (ground and drill core) and the AI and CCPI values shows a statistically significant positive correlation, suggesting that high alteration intensity values are in general associated with a shift toward a more Fe-rich biotite/chlorite composition in the study area. However, the Fe-OH absorption feature wavelength positions of biotite and chlorite indicate that these minerals have a predominantly Mg-rich composition throughout the study area (see Figs. 3.3B,D). Hence the observed shift toward a more Fe-rich composition is relative and does not imply that biotite/chlorite are universally intermediate to Fe-rich in the highly altered areas. It is also notable that, as for the Al-OH wavelength positions of the drill core spectral dataset, the weakness of the correlation between the Fe-OH absorption features and the alteration intensity estimates suggests that changes in the latter are not always accompanied by systematic changes in the wavelength positions of the former. Nevertheless, the observed correlations between the Al-OH and Fe-OH absorption feature wavelength positions and the alteration indices contrast the findings of a study by Herrmann et al. (2001) that reported no clear associations between the spectral datasets and the AI and CCPI.

Our study highlights the importance of using all available geological and lithochemical information when modeling the hydrothermal alteration intensity variation of VMS deposits. The proximal and distal areas of the Izok Lake mineralization are characterized by high and low hydrothermal alteration intensity values, respectively, but both areas have Mg-rich biotite/chlorite that are spectrally similar. However, estimating the relationships between the hyperspectral and lithochemical datasets separately for the areas of sericitic (ground datasets) and chloritic (drill

core datasets) alteration gave uniform results in the form of a three-dimensional hyperspectral model that can be used for ore deposit vectoring in the study area.

3.5.3 Implications of the spectral features for deposit genesis

Iron enrichment is common in the highly altered discharge areas of VMS deposits that typically contain Fe-rich chlorite (MacLean and Hoy 1991, Barrett and MacLean 1994). Our infrared spectroscopic data, however, indicate that the most intense alteration at the Izok Lake deposit contains more Mg-rich chlorite and biotite than the (less altered) footwall rocks. This finding is supported by Money and Heslop (1976), who reported Mg-enrichment in rocks proximal to the deposit. The chemical composition of chlorite is influenced by the chemical composition of its host rocks (Bettison-Varga and MacKinnon 1997), and hence Mg-rich bulk rock compositions are likely to be associated with Mg-rich chlorite. Several studies (Schmidt 1988, Schade et al. 1989, Paulick et al. 2001, Hannington et al. 2003) have similarly noted Mg-enrichment in the vicinity of the feeder (fluid upflow) zones of VMS deposits, and attributed these patterns to the late-stage influx of sea water. Such Mg-enrichment can overprint other geochemical patterns (Barrett and MacLean 1994). Fluid temperature is an important control on Mg-metasomatism (Seyfried and Mottl 1982). Magnesium is precipitated from sea water when the water is heated to temperatures above 150 °C (Bischoff and Seyfried 1978, Tivey 2007). Clinocllore lies in the stability field of seawater heated to 250 °C in the $\text{MgO} + \text{K}_2\text{O} + \text{Al}_2\text{O}_3 + \text{SiO}_2 + \text{H}_2\text{O}$ system (Larson 1984), and hence the influx of seawater into an active VMS deposit may contribute to the formation of this Mg-rich alteration mineral.

An area of strong alteration is located west of the known massive sulfide lenses (Figure

3.8C). Paleo-hydrothermal upflow and discharge zones generally display the highest alteration intensities in VMS deposits (German and Von Damm 2006), and hence these areas merit further exploration, as this intense alteration may be associated with yet unrecognized mineralization.

3.6 SUMMARY AND CONCLUSIONS

Ground and drill core spectroscopy of the host rocks to the Izok Lake VMS deposit display a wide spectral range of the Al-OH and Fe-OH absorption feature wavelength positions that indicates considerable chemical compositional variation within the contained phyllosilicate minerals. This variation is attributable to variable parameters during the hydrothermal alteration process, possibly including the physico-chemical composition of the hydrothermal fluids, water/rock-ratios and temperature that have influenced the mineralogical and chemical composition of the alteration mineral assemblages. These processes have resulted in the formation of Al-rich white micas and Mg-rich biotite/chlorite in the intensely altered rocks of the proximal areas. The Mg-rich composition of chlorite and biotite in these areas is likely due to late-stage influx of seawater, resulting in Mg-metasomatism overprinting of earlier Fe-rich alteration assemblages. Further away from the proximal alteration is a zone of Al-poor white micas and intermediate to Fe-rich biotite and chlorite. Outside of this alteration zone, distal to the deposit, there is a zone of predominantly potassic muscovite and Mg-rich biotite/chlorite.

The weak, positive correlation between the Fe-OH absorption feature wavelength positions and the alteration intensity, as measured using the AI and CCPI, is evident in both the ground and drill core spectral datasets. There is also a statistically significant correlation between the Al-OH absorption feature wavelength positions of the drill core spectrometry and alteration

intensity, but this is only recorded in the drill core spectra, and not the ground spectra. Hence, in the study area, the spectral properties of chlorite/biotite follow the alteration intensity variation more closely than those of the white micas. Although the correlation coefficients between the Al-OH/Fe-OH absorption feature wavelength positions and the AI/CCPI are weak, the Al-OH and Fe-OH wavelength positions of the white micas and biotite/chlorite, respectively, provide a reasonably good indicator of the alteration intensity of the rocks that host the Izok Lake VMS deposits. However, the weak correlations between the Al-OH and Fe-OH absorption feature wavelength positions and the alteration indices suggest that the spectral shifts detected in these phyllosilicate minerals are better suited for inferring large-scale rather than small-scale alteration patterns. Moreover, because different VMS deposits have different alteration fingerprints due to the complexity of factors that induce hydrothermal alteration, caution should be taken, and a baseline study is recommended before applying the conclusions for Izok Lake to other VMS deposits elsewhere.

TABLE 3.1. Summary statistics of the Al-OH and Fe-OH absorption features of the ground and drill core spectra.

	Min, nm	Max, nm	Median, nm	Mode, nm	Range, nm	<i>N</i>
Al-OH, ground spectrometry	2195	2215	2203	2203	21	357
Al-OH, drill core spectrometry	2194	2216	2199	2199	22	585
Fe-OH, ground spectrometry	2249	2260	2254	2255	12	264
Fe-OH, drill core spectrometry	2244	2259	2252	2250	15	344

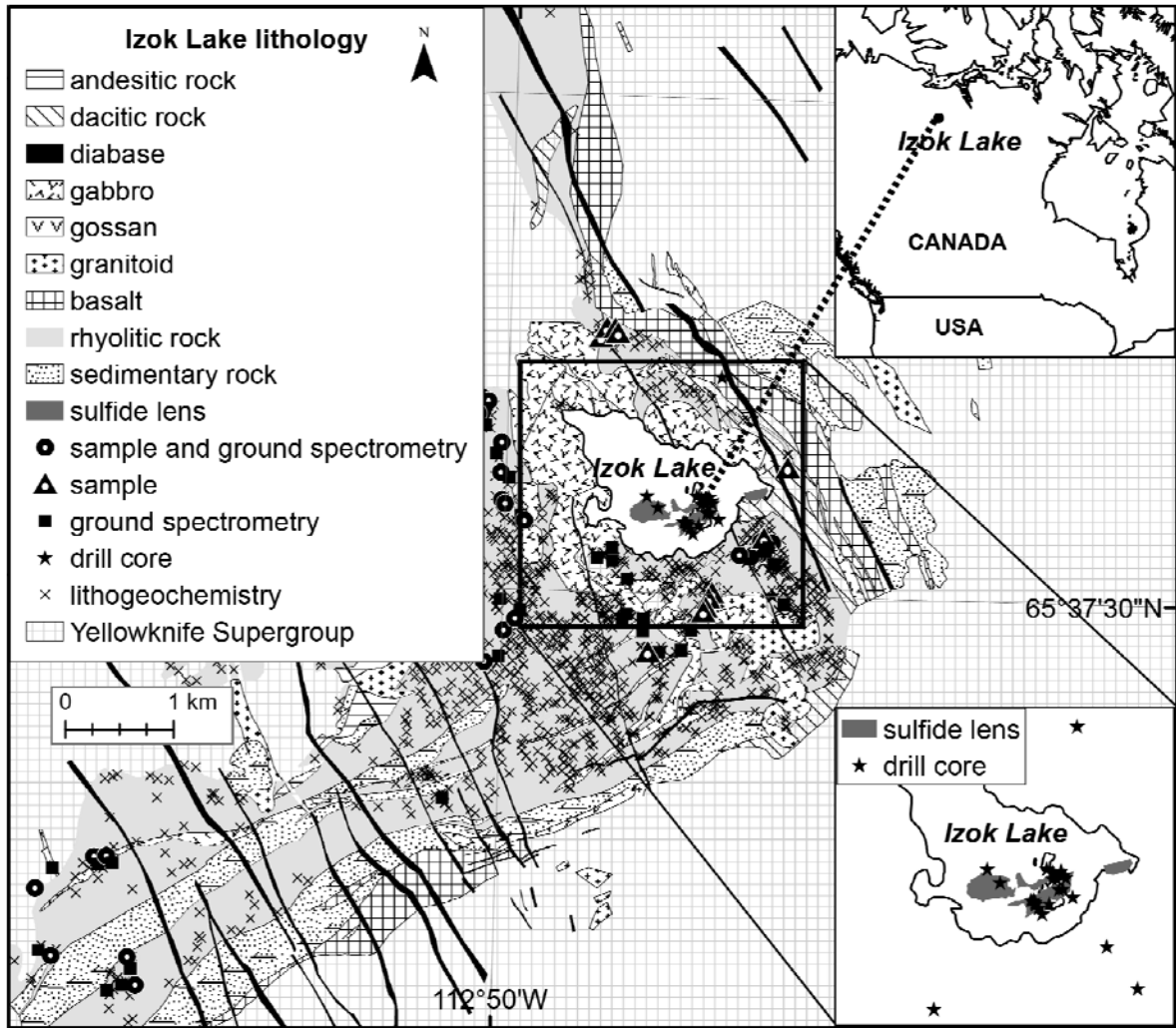


FIGURE 3.1. Location map and geological map of the Izok Lake study area showing the locations of the ground spectrometric sites, samples, drill cores and lithogeochemical samples. The geology and projected location of massive sulphide zones are from Minerals and Metals Group Ltd, unpublished.

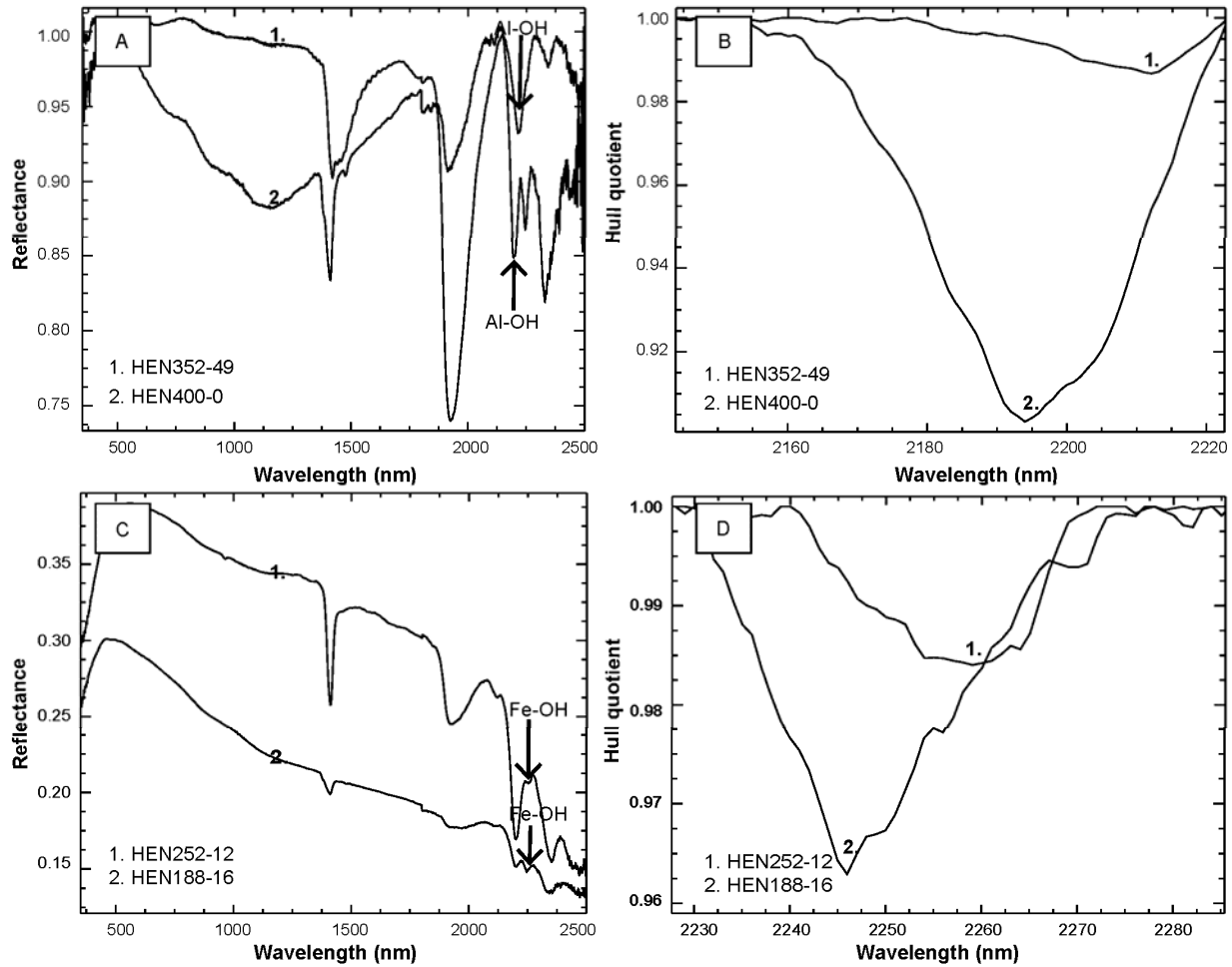


FIGURE 3.2. A) Reflectance spectra from drill cores HEN352 ("HEN352-49", spectrum 1) and HEN-400 ("HEN400-0", spectrum 2); B) Selected range plot of hull quotient-corrected spectra 1 (absorption feature wavelength position: 2216 nm) and 2 (absorption feature wavelength position: 2194 nm) shown in A; C) Reflectance spectra from drill cores HEN-188 ("HEN188-16", spectrum 1) and HEN252 ("HEN252-12", spectrum 2); D) Selected range plot of hull quotient-corrected spectra 1 (absorption feature wavelength position: 2259 nm) and 2 (absorption feature wavelength position: 2246 nm) shown in C.

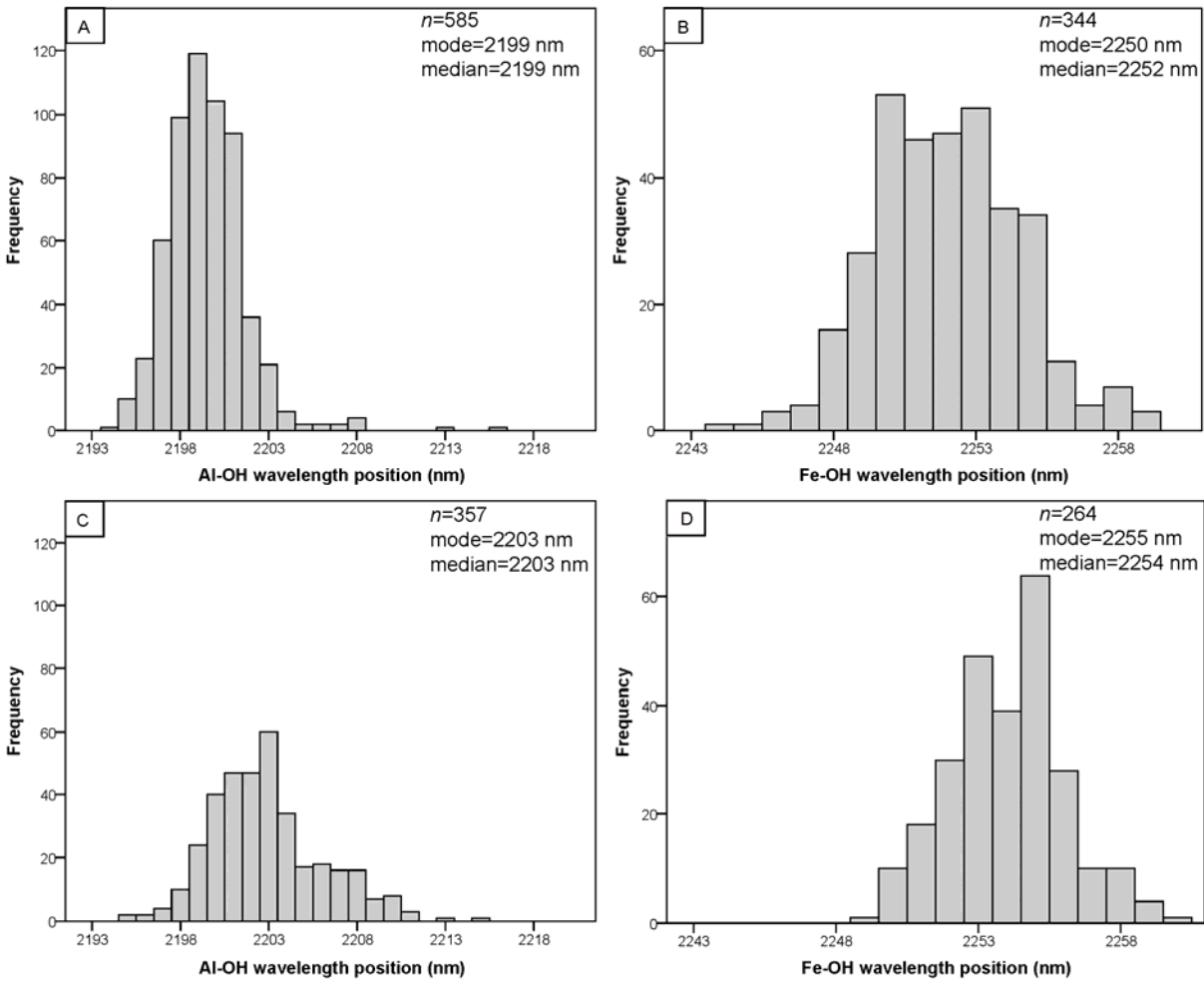


FIGURE 3.3. Frequency distribution histograms of absorption band position for: A) drill core Al-OH absorption; B) drill core Fe-OH absorption; C) ground spectra Al-OH absorption; D) ground spectra Fe-OH absorption.

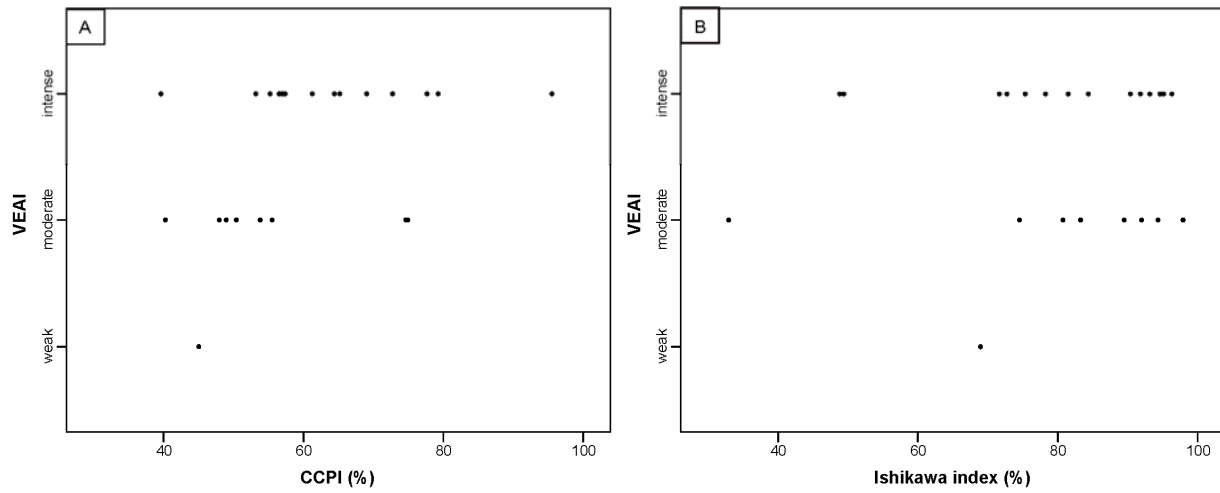


FIGURE 3.4. Bivariate plot of the visually estimated alteration intensity (VEAI) of the drill cores versus A) the calculated chlorite-carbonate-pyrite index (CCPI) (expressed as %) and; B) the calculated Ishikawa index (AI) (expressed as %).

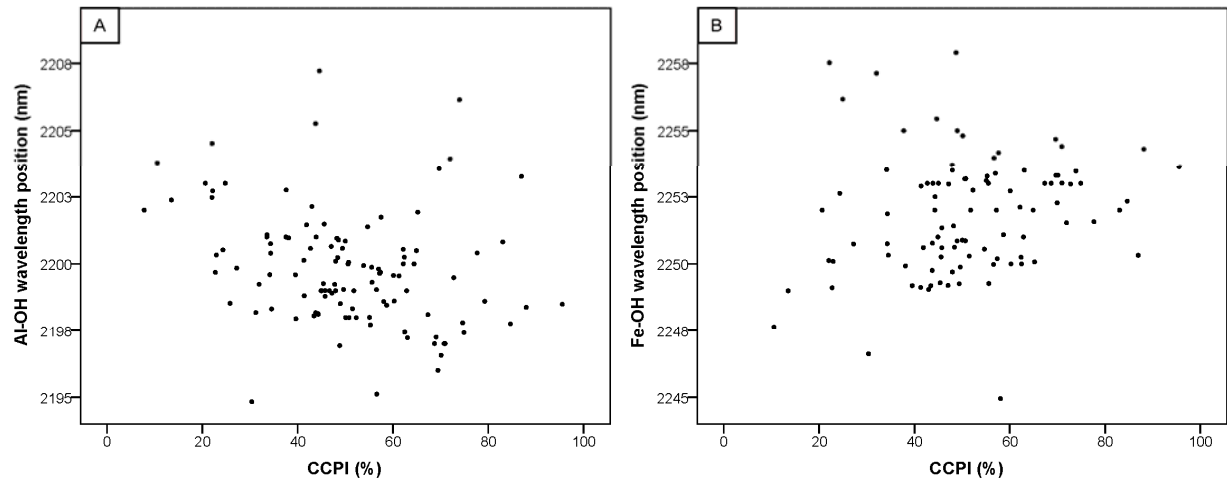


FIGURE 3.5. Bivariate plot of the chlorite-carbonate-pyrite index (CCPI, expressed as %) calculated from the lithochemical data for the drill core samples versus A) the Al-OH wavelength positions (in nm) and; B) the Fe-OH wavelength positions (in nm).

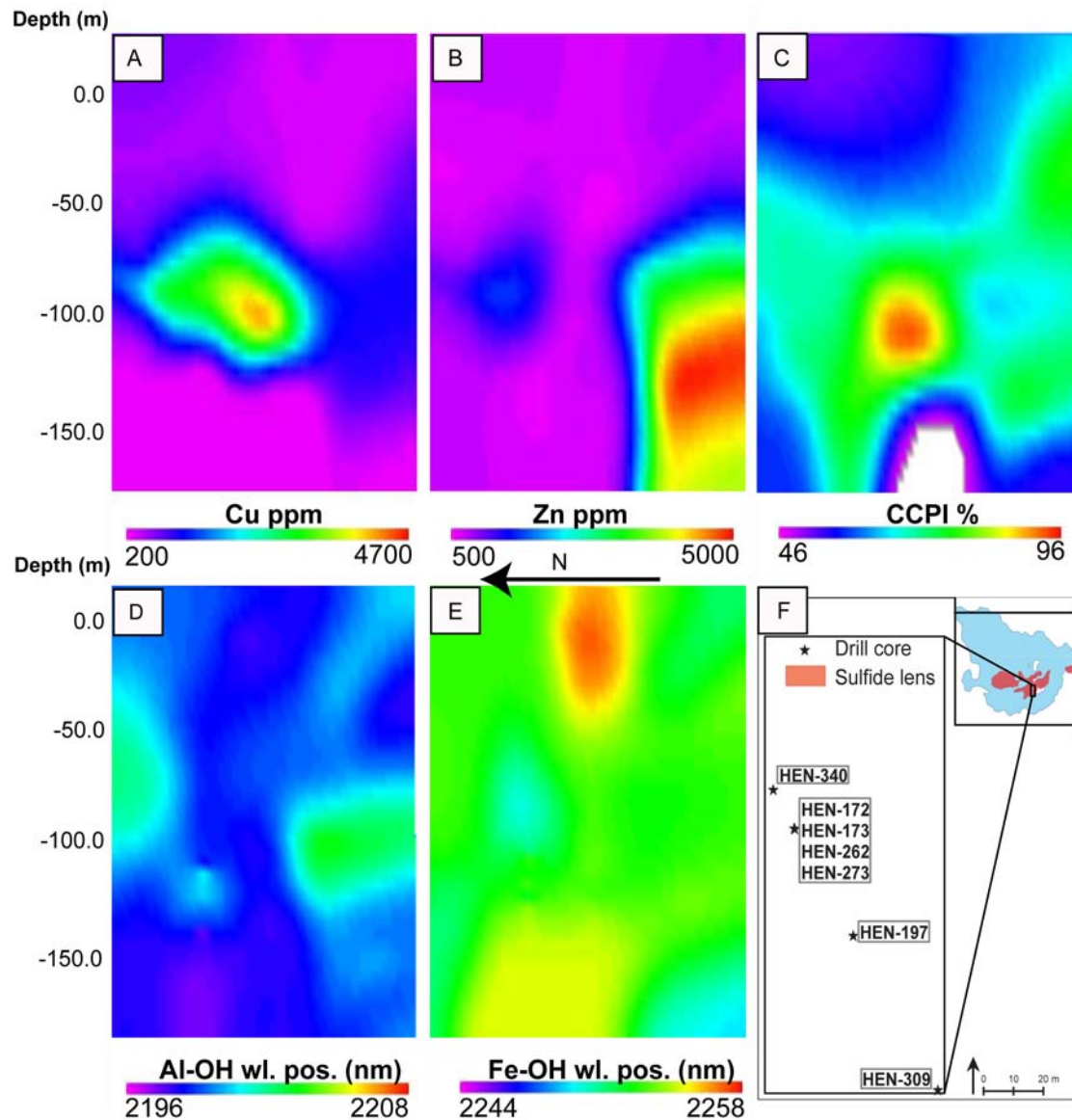


FIGURE 3.6. A vertical cross section of the lithochemical and spectral trends across seven drill cores (HEN-172, HEN-173, HEN-197, HEN-262, HEN-273, HEN-309 and HEN-340). Downhole variation of: A) Cu contents (ppm); B) Zn contents (ppm); C) chlorite-carbonate-pyrite index (CCPI, %) values; D) Al-OH absorption feature wavelength positions (nm); E) Fe-OH absorption feature wavelength positions (nm). The Cu and Zn contents of the drill cores are extracted across all lithologies and the CCPI, Al-OH and Fe-OH values are extracted from the rhyolitic rock sections of the drill cores. Subfigure F: a map view of the locations of the drill cores.

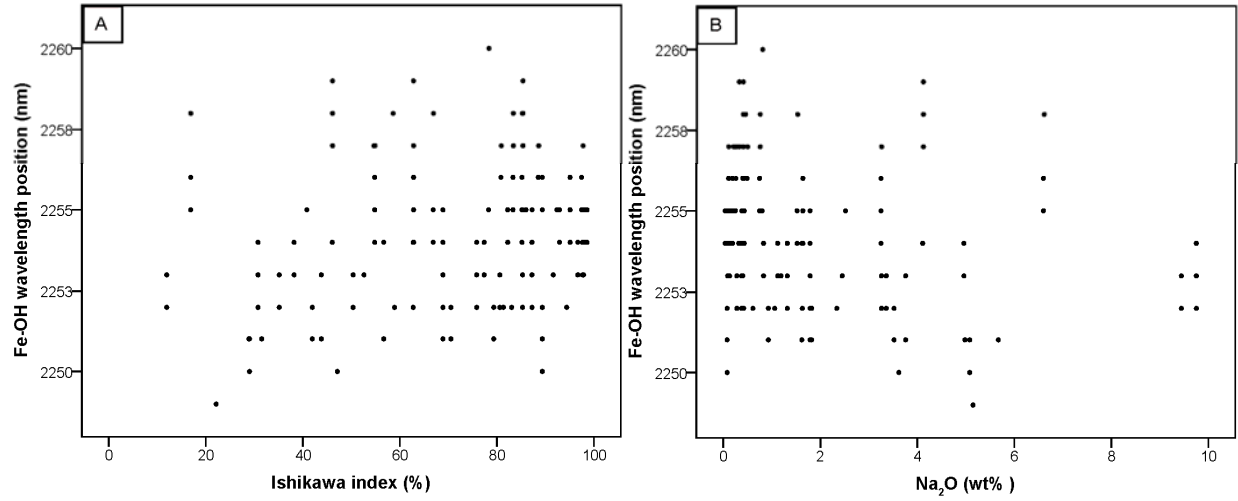


FIGURE 3.7. Bivariate plots of: A) the Fe-OH absorption feature wavelengths of the ground spectra versus the Ishikawa index (AI, expressed as %), extracted from the rhyolitic rock sections of the ground samples and; B) the Fe-OH absorption feature wavelengths versus whole rock Na₂O content (expressed as %), extracted from the rhyolitic rock sections of the ground samples.

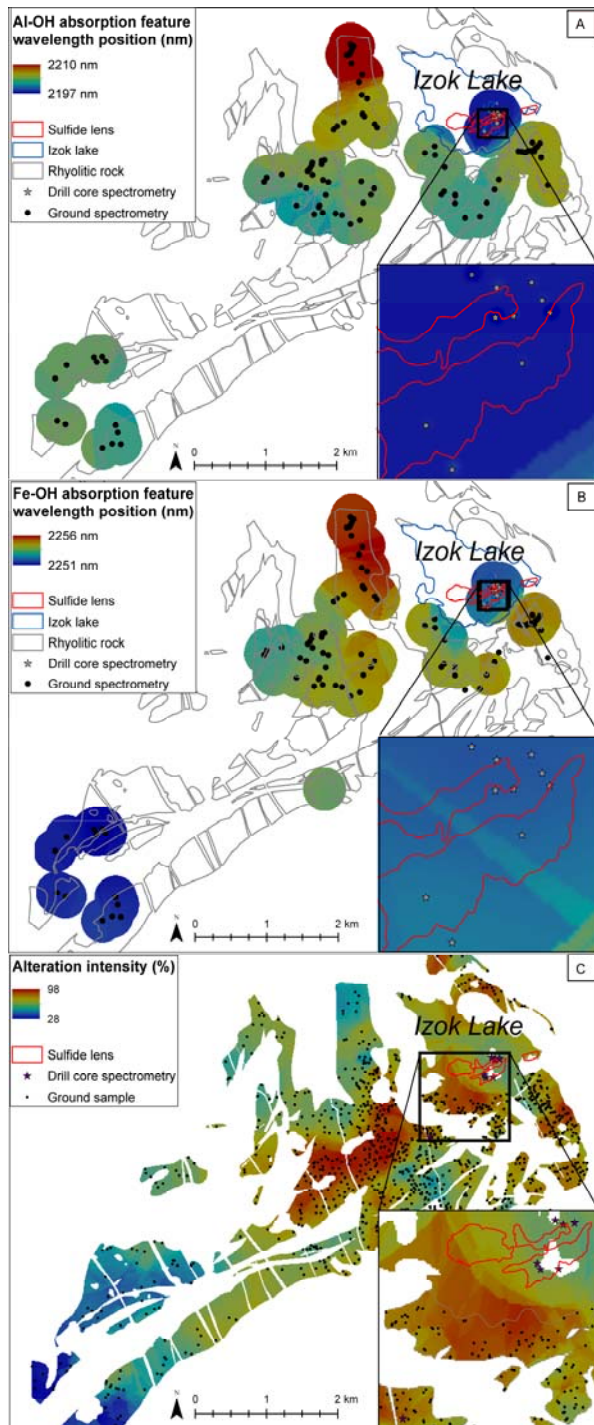


FIGURE 3.8. Colour gradient map of the absorption feature wavelength positions extracted from the drill core and ground spectra for A) Al-OH and B) Fe-OH. C) Color gradient map of the AI calculated from the lithogeochemical data for drill core and ground samples.

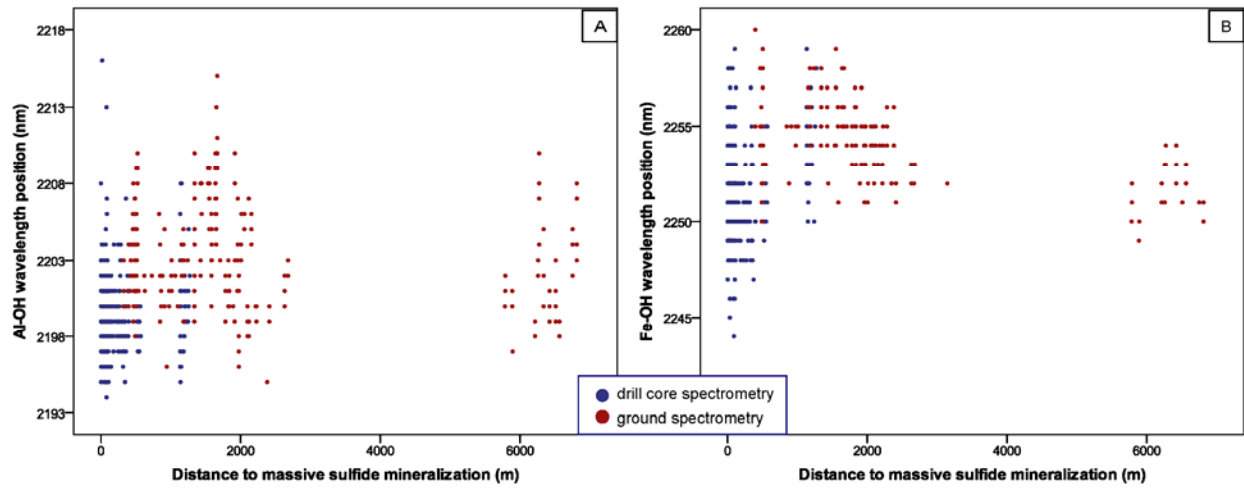


FIGURE 3.9. Bivariate plots of the absorption feature wavelength positions of the ground and drill core spectra versus distance from massive sulfide mineralization for A) Al-OH and B) Fe-OH.

LITERATURE CITED

- Barrett, T.J. and MacLean, W.H., 1994. Chemostratigraphy and hydrothermal alteration in exploration for VHMS deposits in greenstones and younger volcanic rocks. In Lentz, D.R. (ed): Alteration and alteration processes associated with ore-forming Systems. Geological Association of Canada, short course notes 11: 433–467.
- Bassett, W., 1960. Role of hydroxyl orientation in mica alteration. *Bulletin of the Geological Society of America* 71: 449–456.
- Bettison-Varga, L. and MacKinnon, I.D.R., 1997. The role of randomly mixed-layered chlorite/smectite in the transformation of smectite to chlorite. *Clays and Clay Minerals* 45: 506–516.
- Biel, C., Subías, I., Fanlo, I., Mateo, E. and Acevedo, R.D., 2010. The Arroyo Rojo volcanic-hosted massive sulphide deposit (Tierra del Fuego, southernmost Argentina): geology, mineralogy, petrography and mineral chemistry. *Revista Mexicana de Ciencias Geológicas* 27: 84–96.
- Bischoff, J.L. and Seyfried, W.E., 1978. Hydrothermal chemistry of seawater from 25° to 350°C. *American Journal of Science* 278: 838–860.
- Bruegge, C.J., Stiegman, A.E., Rainen, R.A. and Springsteen, A.W., 1993. Use of Spectralon as a diffuse reflectance standard for in-flight calibration of earth-orbiting sensors. *Optical Engineering* 32: 805-814.
- Buckingham, W.F. and Sommer, S.E., 1983. Mineralogical characterization of rock surfaces formed by hydrothermal alteration and weathering - application to remote sensing. *Economic Geology* 78: 664–674.

- Çağatay, N.M., 1993. Hydrothermal alteration associated with volcanogenic massive sulfide deposits: Examples from Turkey. *Economic Geology* 88: 606–621.
- Cathelineau, M., 1988. Cation site occupancy in chlorites and illites as a function of temperature. *Clay Minerals* 23: 471–485.
- Clark, R.N., 1999. Chapter 1: Spectroscopy of rocks and minerals, and principles of spectroscopy. In: Rencz, A.N., ed.: *Manual of remote sensing, Volume 3. Remote Sensing for the Earth Sciences*. John Wiley and Sons, New York, USA: 3–58.
- Clark, R.N., Swayze, G.A., Livo, K.E., Kokaly, R.F., King, T.V.V., Dalton, J.B., Vance, J.S., Rockwell, B.W., Hoefen, T. and McDougal, R.R., 2002. Surface reflectance calibration of terrestrial imaging spectroscopy data. A tutorial using AVIRIS. *Proceedings of the 10th Airborne Earth Science Workshop*, JPL Publication 02-1.
- Costa, U.R., Barnett, R.L. and Kerrich, R., 1983. The Mattagami Lake Mine Archean Zn-Cu sulfide deposit, Quebec: Hydrothermal coprecipitation of talc and sulfides in a sea-floor brine pool-evidence from geochemistry, $^{18}\text{O}/^{16}\text{O}$, and mineral chemistry. *Economic Geology* 78: 1144–1203.
- Date, J., Watanabe, Y. and Saeki, Y., 1983. Zonal alteration around the Fukazawa Kuroko deposits, Akita prefecture, northern Japan. *Economic Geology Monograph* 5: 365–386.
- Duke, E.F., 1994. Near infrared spectra of muscovite, Tschermak substitution, and metamorphic reaction progress: Implications for remote sensing. *Geology* 22: 621–624.
- Franklin, J.M., 1986. Volcanic-associated massive sulphide deposits – an update. In: Andrew, C.J., Crowe, R.W.A., Finlay, S., Pennell, W.M. and Pyne, J.F.: *Geology and genesis of mineral deposits in Ireland*. Irish Association for Economic Geology, Dublin, UK: 49–69.

- Franklin, J.M., 1997. Lithogeochemical and mineralogical methods for base metal and gold exploration. In: Gubins, A.G. (ed.): Proceedings of Exploration 97: Fourth Decennial International Conference on Mineral Exploration, Toronto, Canada: 191–208.
- Franklin, J.M., Kasarda, J. and Poulsen, K.H., 1975. Petrology and chemistry of the alteration zone of the Mattabi massive sulfide deposit. *Economic Geology* 70: 63–79.
- Galley, A.G., 1993. Characteristics of semi-conformable alteration zones associated with volcanogenic massive sulphide districts. *Journal of Geochemical Exploration* 48: 175–200.
- Galley, A.G., Hannington, M.D. and Jonasson, I.R., 2007. Volcanogenic massive sulphide deposits. In: Goodfellow, W.D. (ed.): Mineral deposits of Canada: A synthesis of major deposit-types, district metallogeny, the evolution of geological provinces, and exploration methods. Special Publication No. 5, Geological Association of Canada, Ottawa, Canada: 141-161.
- Gemmell, J.B. and Large, R.R., 1992. Stringer system and alteration zones underlying the Hellyer volcanic-hosted massive sulfide deposit, Tasmania, Australia. *Economic Geology* 87: 620–649.
- German, C.R. and Von Damm, K.L. 2006. Hydrothermal Processes. In: Elderfield, H.: The Oceans and Marine Geochemistry. Elsevier, Oxford, UK: 181-222.
- Goodfellow, W.D. and Peter, J.M., 1994. Geochemistry of hydrothermally altered sediment, Middle Valley, northern Juan de Fuca Ridge. Mottl, M.J., Davis, E.E., Fisher, A.T. and Slack, J.F (eds.): Proceedings of the Ocean Drilling Program, Scientific Results 139: 207–289.

- Hannington, M.D., Kjarsgaard, I.M., Galley, A.G. and Taylor, B., 2003. Mineral-chemical studies of metamorphosed hydrothermal alteration in the Kristineberg volcanogenic massive sulfide district, Sweden. *Mineralium Deposita* 38: 423–442.
- Herrmann, W., Blake, M., Doyle, M., Huston, D., Kamprad, J., Merry, N. and Pontual, S., 2001. Short wavelength infrared (SWIR) spectral analysis of hydrothermal alteration zones associated with base metal sulfide deposits at Rosebery and Western Tharsis, Tasmania, and Highway-Reward, Queensland. *Economic Geology* 96: 939–955.
- Herrmann, W., Green, G.R., Barton, M.D. and Davidson, G.J., 2009. Lithogeochemical and stable isotopic insights into submarine genesis of pyrophyllite-altered facies at the Boco Prospect, Western Tasmania. *Economic Geology* 104: 775–792.
- Hunt, G.R. and Salisbury, J.W., 1970. Visible and near-infrared spectra of minerals and rocks: I. silicate minerals. *Modern Geology* 1: 283–300.
- Ishikawa, Y., Sawaguchi, T., S.-i. Iwaya and Horiuchi, M., 1976. Delineation of prospecting targets for Kuroko deposits based on modes of volcanism of underlying dacite and alteration haloes. *Mining Geology* 26: 105–117.
- Jones, S., Herrmann, W. and Gemmell, J.B., 2005. Short wavelength infrared spectral characteristics of the HW horizon: Implications for exploration in the Myra Falls volcanic-hosted massive sulfide camp, Vancouver Island, British Columbia, Canada. *Economic Geology* 100: 273–294.
- Kranidiotis, P. and MacLean, W.H., 1987. Systematics of chlorite alteration at the Phelps Dodge massive sulfide deposit, Matagami, Quebec. *Economic Geology* 82: 1898–1911.
- Large, R.R., 1977. Chemical evolution and zonation of massive sulfide deposits in volcanic terrains. *Economic Geology* 72: 549–572.

- Large, R.R., Gemmell, J.B., Paulick, H. and Huston, D.L., 2001. The alteration box plot: A simple approach to understanding the relationship between alteration mineralogy and litho geochemistry associated with volcanic-hosted massive sulfide deposits. *Economic Geology* 96: 957–971.
- Larson, P.B., 1984. Geochemistry of the alteration pipe at the Bruce Cu-Zn volcanogenic massive sulfide deposit, Arizona. *Economic Geology* 79: 1880–1896.
- Leistel, J.M., Marcoux, E., Thiéblemont, D., Quesada, C., Sánchez, A., Almodóvar, G.R., Pascual, E. and Sáez, R., 1998. The volcanic-hosted massive sulphide deposits of the Iberian Pyrite Belt. *Mineralium Deposita* 33: 2–30.
- MacLean, W. and Hoy, L.D., 1991. Geochemistry of hydrothermally altered rocks at the Horne Mine, Noranda, Quebec. *Economic Geology* 86: 506–528.
- McLeod, R.L., Gabell, A.R., Green, A.A. and Gardavsky, V., 1987. Chlorite infrared spectral data as proximity indicators of volcanogenic massive sulphide mineralisation. *Pacific Rim Congress (The Geology, Structure, Mineralisation and Economy of the Pacific Rim)*, Gold Coast, Australia: 321–324.
- Miyashiro, A. and Shido, F., 1985. Tschermak substitution in low- and middle-grade pelitic schists. *Journal of Petrology* 26: 449–487.
- MMG, 2011. Izok Lake. A summary of exploration activity on the Izok Lake project 2007-2011, Annual report Nunavut Impact Review Board, Vancouver, Canada. Available at: [ftp://ftp.nirb.ca/01-screenings/completed_screenings/2006/06EN066-MMG\(Wolfden\)-Izok and Hood Project/05-annual report/120201-06EN066-MMG 2011 Annual Report-IA1E.pdf](ftp://ftp.nirb.ca/01-screenings/completed_screenings/2006/06EN066-MMG(Wolfden)-Izok and Hood Project/05-annual report/120201-06EN066-MMG 2011 Annual Report-IA1E.pdf).
- Money, P.L. and Heslop, J.B., 1976. Geology of the Izok Lake massive sulphide deposit. *Canadian Mining Journal* 97: 24–27.

- Morrison, I.R., 2004. Geology of the Izok massive sulfide deposit, Nunavut Territory, Canada. *Exploration and Mining Geology* 13: 25–36.
- Morrison, I.R. and Balint, F., 1993. Geology of the Izok massive sulphide deposits, Northwest Territories, Canada. *Proceedings of the International Symposium on Zinc*, Hobart, Australia: 161-170.
- Mortensen, J.K., Thorpe, R.I., Padgham, W.A., King, J.E.s and Davis, W.J., 1988. U-Pb zircon ages for felsic volcanism in Slave Province, N.W.T.. In: *Radiogenic Age and Isotopic Studies: Report 2*, Geological Survey of Canada 88-2: 85–95.
- Nesbitt, B.E., 1982. Metamorphic sulfide-silicate equilibria in the massive sulfide deposits at Ducktown, Tennessee. *Economic Geology* 77: 364–378.
- Ohmoto, H., 1996. Formation of volcanogenic massive sulfide deposits: The Kuroko perspective. *Ore Geology Reviews* 10: 135–177.
- Oliver, M.A. and Webster, R., 1990. Kriging: a method of interpolation for geographical information systems. *International Journal of Geographical Information Systems* 4: 313–332.
- Paulick, H., Herrmann, W. and Gemmel, J.B., 2001. Alteration of felsic volcanics hosting the Thalanga massive sulfide deposit (Northern Queensland, Australia) and geochemical proximity indicators to ore. *Economic Geology* 96: 1175–1200.
- Pirajno, F., 2009. Hydrothermal processes and wall rock alteration. In: *Hydrothermal Processes and Mineral Systems*, Springer Netherlands: 73-164.
- Plimer, I.R. and de Carvalho, D., 1982. The geochemistry of hydrothermal alteration at the Salgadoinho Copper Deposit, Portugal. *Mineralium Deposita* 17: 193–211.

- Post, J.L. and Noble, P.N., 1993. The near-infrared combination band frequencies of dioctahedral smectites, micas, and illites. *Clays and Clay Minerals*, v. 41, p. 639–644.
- Sánchez-España, J., Velasco, F. and Yusta, I., 2000. Hydrothermal alteration of felsic volcanic rocks associated with massive sulphide deposition in the northern Iberian Pyrite Belt (SW Spain). *Applied Geochemistry* 15: 1265–1290.
- Schade, J., Cornell, D.H. and Theart, H.F.J., 1989. Rare earth element and isotopic evidence for the genesis of the Prieska massive sulfide deposit, South Africa. *Economic Geology* 84: 49–63.
- Schmidt, J.M., 1988. Mineral and whole-rock compositions of seawater-dominated hydrothermal alteration at the Arctic volcanogenic massive sulfide prospect, Alaska. *Economic Geology* 83: 822–842.
- Seyfried, W.E. and Mottl, M.J., 1982. Hydrothermal alteration of basalt by seawater under seawater dominated conditions. *Geochimica et Cosmochimica Acta* 46: 985–1002.
- Seyfried, W.E., Jr., Berndt, M.E. and Seewald, J.S., 1988. Hydrothermal alteration processes at mid-ocean ridges: Constraints from diabase alteration experiments, hot spring fluids and composition of the oceanic crust. *Canadian Mineralogist* 26: 787–804.
- Stephens, M.B., Swinden, H.S. and Slack, J.F., 1984. Correlation of massive sulfide deposits in the Appalachian-Caledonian Orogen on the basis of Paleotectonic setting. *Economic Geology* 79: 1442–1478.
- Tivey, M.K., 2007. Generation of seafloor hydrothermal vent fluids and associated mineral deposits. *Oceanography* 20: 50-65.

- Urabe, T., Scott, S.D. and Hattori, K., 1983. A comparison of footwall-rock alteration and geothermal systems beneath some Japanese and Canadian volcanogenic massive sulfide deposits. *Economic Geology Monograph* 5: 345–364.
- Velde, B., 1965. Phengite micas: Synthesis, stability, and natural occurrence. *American Journal of Science* 263: 886–913.
- Velde, B., 1967. Si^{+4} content of natural phengites. *Contributions to mineralogy and petrology* 14: 250–258.
- Yang, K., Huntington, J.F., Gemmill, J.B. and Scott, K.M., 2011. Variations in composition and abundance of white mica in the hydrothermal alteration system at Hellyer, Tasmania, as revealed by infrared reflectance spectroscopy. *Journal of Geochemical Exploration* 108: 143–156.

CHAPTER 4 - Enhanced detection of gossans using hyperspectral data: example from the Cape Smith Belt of northern Quebec, Canada

4.1 INTRODUCTION

Gossans are rocks with oxidized surfaces that result from the weathering of sulfide-bearing deposits. Gossans comprise predominantly iron oxide and iron hydroxide minerals (here collectively called the iron oxide minerals) such as goethite (α -FeOOH) and hematite (Fe_2O_3). Gossans form at or near the surface where ferrous iron and sulfide minerals are unstable in the presence of weathering agents such as water-dissolved oxygen. These minerals are then converted to iron oxide and sulfate minerals that are less soluble and more stable under surface conditions (Krauskopf 1967). Weathering of the iron sulfides leads to a drop in pH which in turn increases acidity and the weathering rates of sulfides. The profiles that develop through these processes can be tens of metres thick (Bellott et al. 1991, Maria Dreher et al. 2005).

Gossans have distinct earthy colors that result from their spectral characteristics in the visible and near infrared (VNIR; 400-1300 nm) wavelength regions. These characteristics and the economic significance of gossans have drawn the attention of the geologic remote sensing community since the early days of satellite imaging (see Rowan et al. 1977, and references therein). The majority of remote sensing studies that pertain to gossans have focused on low latitude regions where ground cover is minimal or absent. These studies (see e.g. Abdelsalam et al. 2000, Volesky et al. 2003) have shown that orbital multispectral scanners, such as Landsat and ASTER, can be used to detect gossan outcrops in the absence of significant vegetation even at a spatial resolution of 30 m (e.g. Landsat Thematic Mapper). Studies by Bierwirth et al. (2002) and

Rogge et al. (2014) have demonstrated that metre sized gossan outcrops can be delineated, and their iron oxide compositions estimated, by means of airborne hyperspectral datasets of high spatial and spectral resolutions.

The ability to detect gossan outcrops by remote sensing is crucial to support mineral exploration in high latitude regions where field access is difficult. Regions located above the treeline are ideal for remote sensing studies due to the dearth of standing vegetation. However, lichens, the dominant autotrophs of polar ecosystems (Longton 1988), typically form extensive mats on rock outcrops and obscure the spectral properties of the underlying bedrock (Rivard and Arvidson 1992) due to their optical thickness that prevents the transmission of light to the rock substrate (Ager and Milton 1987, Bechtel et al. 2002). Some authors have observed that gossanous areas generally have sparse vegetation (see e.g. West et al. 2009). However, rock encrusting lichens do grow on iron oxide -rich rocks (Purvis and Halls 1996). If the lichen cover is not complete, spectral mixing of gossans, lichens and the rock substrate will take place, which may have a significant impact on spectral characterization and detection of gossans.

The Cape Smith Belt is a high latitude (60 degrees north) Proterozoic fold and thrust belt that is the fourth most productive magmatic Ni-Cu-platinum group element (PGE) resource in Canada (Lydon 2007). The belt comprises numerous gossan outcrops that span a range of characteristics. Thick gossans, which are commonly associated with sedimentary rocks and exhalites, occur as large showings and are not associated with economically viable ore deposits as they developed through weathering of the iron-rich gangue minerals, such as pyrite, or by means of transportation. These gossan surfaces are referred to as barren gossans to distinguish them from fertile gossans that potentially host significant concentrations of sulfide minerals

(Taylor 1987). Thick gossans typically have little or no encrusting lichens owing to low pH. In contrast, lichens generally occur on gossans that only have a thin oxidized layer. In the Cape Smith Belt thin gossans are commonly associated with ultramafic rocks and in the context of exploration act as spatial indicators for prospective deposits. Thus the detection of thin gossans by means of remote sensing is of merit to support exploration activities.

This study was motivated by the observation that despite the voluminous literature on remote sensing of thick gossans, little attention has been paid to the detection of thin gossans, which may be indicators of potential ore bodies, and the effect that biogenic coatings (e.g. lichens) and rock substrate mineralogy could impart on the spectral properties of thin gossans. The detection of thick gossans typically relies on sensing of VNIR spectral features diagnostic of iron oxide minerals (e.g. hematite and goethite) and establishing associations with specific bedrocks. Thin gossans on the other hand may reveal short-wave infrared (SWIR, 1300-2500 nm) spectral properties of the rock substrates beneath the oxidized surfaces. There is thus potential remote sensing information that could be used to distinguish fertile gossans from barren gossans in areas of a known association between specific rock types and mineral deposits.

First, this study examines laboratory spectroscopic data (point and imaging spectroscopy) obtained from field samples encompassing thin gossans of the Cape Smith belt with varying degree of lichen cover. From these data we investigate the effects of the rock substrates (sedimentary, mafic and ultramafic) and the effects of lichens on the VNIR spectra of gossans. Next we scale upwards to airborne hyperspectral imagery to highlight and discriminate thick and thin gossans and associate thin gossans to substrate rock type based on the detection of SWIR spectral features. Thus we examine the ability to detect the spectral properties of the rock

substrates in the SWIR from airborne imagery. We begin by providing geological background on the study area and a description of the various spectroscopic data used, followed by a description of the methodological approach. Laboratory results are then followed by the outcomes of the airborne image analysis and general implications for regional mapping of gossans.

4.2 STUDY AREA

The Cape Smith Belt (60°43'N-62°35'N, 78°11'W-71°59'W) has a rolling topography with relatively good exposure of bedrock. The area is located in a treeless shrub tundra biome that has a mean annual temperature of -7 °C (Payette et al. 1989, St-Onge and Lucas 1993). Due to the climatic conditions the flora of the study area comprises lichens, mosses, shrubs and other low-growing plants. Lichen cover on bedrock varies from nil to exceeding 75%, but generally partially covers rock outcrops.

Geologically the Cape Smith Belt is a Proterozoic fold and thrust belt that constitutes the Ungava segment of the Trans-Hudson orogen (Parrish 1989). The belt consists of several Early Proterozoic tectonic units (from 2.038 to 1.826 Ga; Machado et al. 1993) that separate the Archean gneisses of the Superior Province in the south from the Churchill Province gneisses to the north (Figure 4.1; Modeland et al. 2003). The Povungnituk group, the southernmost unit, consists of sedimentary and volcanic rocks associated with initial Paleoproterozoic rifting of the Superior Province (St-Onge et al. 2000). Farther north, the pillowed and lensoid lava flows of the Chukotat group record a transition from continental rifting to the formation of oceanic crust (Hynes and Francis 1982). The Ni-Cu-PGE deposits of the Cape Smith Belt are associated with mafic and ultramafic lithologies (Leshner 2007) of the Povungnituk and Chukotat groups

(Giovenazzo et al. 1989) and these map units were the focus of our field sampling of gossans. The mineralization comprises pyrrhotite, pentlandite, chalcopyrite, magnetite, ferrochromite, pyrite and PGE minerals (Dillon-Leitch et al. 1986, Giovenazzo et al. 1989). All lithologies were metamorphosed under lower greenschist to middle amphibolite facies conditions (St-Onge and Lucas 1993) and consequently serpentine, amphibole and chlorite group minerals (Giovenazzo et al. 1989, St-Onge and Lucas 1993) abound. Details on units occurring further north (Figure 4.1; Parent and Spartan groups, Watts Group, Narsajuaq Arc) can be found in St-Onge and Lucas (1993), Scott et al. (1992) and St-Onge et al. (1992).

4.3 DATASETS AND SPECTRAL MEASUREMENTS

4.3.1 Sample suite and site selection

In the summer of 2009 and 2010, one hundred and thirty-nine hand samples were collected from outcrops located in the central areas of the Povungnituk and Chukotat groups (Fig. 4.1). The samples encompass mafic, ultramafic and sedimentary rocks of the study area and twenty-three gossans. Each sample presents a weathered surface and these show variable lichen cover across the sample suite. The samples have remained exposed to light and air before their spectral properties were measured to ensure the preservation of lichens at the time of data acquisition. All the gossan samples exhibit a thin, dull and relatively continuous oxidized surface (Fig. 4.2A,B).

4.3.2 X-ray diffraction

The samples were analyzed by means of X-ray powder diffraction (XRD, Rigaku, Ultima IV) to determine their mineralogical makeup. A subset of each sample was cut, crushed

and ground to a mineral powder that comprised both the weathered and fresh parts of each sample. The X-ray diffraction analysis results for the gossan samples are shown in Table 4.1. Samples from mafic and ultramafic rocks contain abundant amphibole (typically: actinolite), chlorite (typically: clinochlore) and serpentine (typically: antigorite) group minerals. Feldspar and epidote group minerals are common in the samples of mafic rocks. The samples of sedimentary rocks are dominated by quartz and mica group minerals. Moreover, samples 6, 13, 15 and 16 contain the iron oxide minerals hematite (two samples), goethite (one sample), lepidocrocite (one sample) and magnetite (one sample). All the gossan samples contain one iron oxide mineral, except sample 16 that contains both goethite and lepidocrocite.

4.3.3 Laboratory spectral measurements

4.3.3.1 Measurements with an ASD FieldSpec[®] 3 spectroradiometer

Spectral measurements were collected from the samples using a PANalytical Boulder Inc. (formerly ASD Inc.) FieldSpec[®] (hereafter referred to as the ASD spectrometer). These spectra were recorded for the 350-2500 nm wavelength region at a spectral resolution of 3 nm (1.4 nm sampling interval) in the VNIR and 10 nm (sampling interval: 1 nm) in the SWIR. Two sets of measurements were collected from the gossan and non-gossan samples: 1) from the lichen-free weathered surfaces, and 2) from the lichen-covered weathered surfaces. These measurements were used to assess the effects of lichens and rock substrates on the spectra of thin gossans. All the spectra were collected using a contact probe (field of view 10 mm) with an internal light source that minimizes the effects of illumination variability during data acquisition. Each spectrum recorded by the spectroradiometer comprises 20-25 individual measurements

taken consecutively and averaged. The radiance values obtained by the spectroradiometer were calibrated to reflectance values using a Spectralon™ panel (Bruegge et al. 1993).

The first set of measurements was collected from 1-4 lichen-free, weathered surfaces of each sample (gossans and non-gossans). These spectra ($n=124$) were acquired from selected samples ($n=48$) that have at least one lichen-free surface with a minimum diameter of 10 mm determined by the diameter of the contact probe. The second set of measurements was acquired from 16 gossan and non-gossan samples that displayed a minimum lichen cover of 90%. These spectra ($n=27$) were acquired from lichens of different colors (red, black-grey and white-green) to account for their possible inter-species spectral variation.

4.3.3.2 Measurements with a SisuRock imager

Spectral imagery was acquired from the weathered surface of the gossan samples using a SisuRock imager. This imaging system is equipped with two cameras that operate in the visible-near infrared (VNIR, 397-1002 nm) and short-wave infrared (SWIR, 928-2530 nm) wavelength regions. The VNIR camera acquired images with a 0.8 mm spatial resolution, 3.6 nm bandwidth and 3.1 nm sampling interval. The SWIR camera acquired images with a 2 mm spatial resolution, 10 nm bandwidth and 6.3 nm sampling interval.

4.3.4 Airborne spectral imaging

Airborne hyperspectral data with pixels of 2x2 m were acquired over 1663 km² in the summer of 2008 ("airborne survey" in Figure 4.1) using a ProSpecTIR system that incorporates the Specim Eagle (VNIR wavelength region) and Hawk (SWIR wavelength region) imaging spectrometers. These data were obtained in the 390-2400 nm wavelength range with a 6.3 nm

sampling interval and 10 nm bandwidth. The dataset was preprocessed by SpecTIR LLC by converting radiance values to reflectance values using the ATCOR[®] 4 software package and MODTRAN[®] 4 atmospheric lookup tables (Richter and Schläpfer 2002). Next, the dataset was geocorrected by means of a three-axis gyroscope attitude INS (Inertial Navigation System) that was positioned with a 12-channel GPS system and boresight calibration data.

The airborne data comprises 22 flight-lines that were corrected for across-track and between-flight-lines radiometric inconsistencies induced by the preprocessing procedures (e.g. atmospheric correction) or changes during the data acquisition (e.g. illumination geometry variation). The corrected flight-lines were subsequently used to generate a single image mosaic, of which a 35 km² subset ("focus area" in Fig. 4.1) was chosen for in-depth analysis in this study owing to multiple known gossans and additional field observations. The number of available bands was reduced owing to the effects of water-associated absorption features (near 1400 nm and 1900 nm), low signal-to-noise ratio (short of 436 nm and long of 2400 nm) and spurious spectral features caused by pre-processing of the airborne data (near 1000 nm). A detailed description on these pre-processing procedures can be found in Rogge et al. (2014).

4.4 SPECTRAL ANALYSIS METHODOLOGY

The iron oxide minerals of gossans have characteristic absorption features in the visible-near infrared wavelength region (VNIR; 400-1300 nm) due to electronic transitions and charge transfers of iron (Hunt et al. 1971). They display a pronounced ferric absorption feature near 900 nm (the ferric iron ${}^6A_1 \rightarrow {}^4T_1$ transition; the "ferric absorption feature" from herein) with an average band position varying from 884 nm for hematite, 917 nm for goethite, to 961 nm for

lepidocrocite (Cornell and Schwertmann 2003). The effects of the rock substrates and lichens on the ferric absorption feature were studied by investigating the relationship between the ferric absorption feature band depth and band position. The intensity of an absorption feature is related to the absorber concentration (Buckingham and Sommer 1983) and hence changes in the depth of the absorption feature are indicative of the thickness of the oxidized surfaces of gossans. Many rock types have ferromagnesian minerals that can induce a ferrous absorption feature near 1000 nm (Hunt et al. 1974, Hunt and Salisbury 1976), thus, spectral mixing with thin gossans (as indicated by the low absorption feature band depths), can shift the position of the ferric absorption feature.

In order to reach the three main objectives, our analysis makes use of both laboratory spectroscopic and airborne data. The first two objectives rely on the investigation of characterized field samples measured with the ASD and SisuRock systems. SisuRock imagery for the twenty-three gossan samples, was used to assess the effect of the rock substrates on the ferric absorption feature. The high spatial resolution of the images provided hundreds of thousands of spectra. The effects of lichens on the spectral properties of gossans were studied with targeted ASD spectra obtained from the lichen-free and lichen-covered parts of the samples. Synthetic mixtures of gossans and non-gossans and gossans and lichens were used to further assess the effects of rock substrates and lichens on the ferric absorption feature of gossans as a function of varying degrees of spectral mixing.

The results obtained for the first two objectives guided the analysis of the airborne data aimed at the identification of the type of gossans and an estimation of their distribution.

4.4.1 Processing of the ASD spectrometry

ASD spectral measurements of lichens taken from the rock samples were averaged to create a single spectral representation of a lichen. The same procedure was repeated for each rock type (sedimentary, mafic and ultramafic) to produce a representation of a lichen-free gossan, and a lichen-free non-gossan. These averaged spectra were then used to generate spectral mixtures of i) gossans and non-gossans and ii) gossans and lichens. These mixtures were conducted in 1% increments and are weighted averages of two spectra:

$$R_j = \sum_{i=1}^n w_{ij} S_{ij}$$

where

R_j = mixed pixel reflectance of the j^{th} band

n = number of spectra

w_{ij} = weight of the i^{th} spectrum in the j^{th} band

$S_{i,j}$ = measured reflectance of the i^{th} spectrum in the j^{th} band.

4.4.2 Processing of the laboratory spectrometry

For the Sisurock images a number of steps were required to extract the lichen-free areas from the VNIR and SWIR images, such that the impact of rock substrates on the ferric absorption features could be assessed.

First the VNIR and SWIR images were smoothed using a spatial and spectral approach (Iterative Adaptive Smoothing filter, Rogge and Rivard 2010) to reduce intra-class variability

and random noise. Next lichen and rock endmembers (or: spectrally pure representations of elements in the scene) were extracted from each SWIR image by means of the Spatial-Spectral Endmember Extraction application (SSEE, Rogge et al. 2007) which produced a total of 329 candidate endmembers spectra that include spectrally similar, but spatially independent pixels. Twelve endmembers were chosen from the candidate endmember set to represent rock ($n=11$) and lichen ($n=1$) surfaces based on their spectral characteristics. In a third step, the SWIR images were spectrally unmixed using the above endmembers as input into the Iterative Spectral Unmixing application (ISMA, Rogge et al. 2006). Spectral unmixing was constrained to the 1874-2487 nm wavelength region because lichens display similar spectral characteristics in the SWIR (Bechtel et al. 2002), and hence a single lichen endmember could represent all lichen species. A threshold value was then determined separately for the lichen fractional abundance image of each SWIR image ($n=23$), based on visual interpretation, with the aim to mask lichen-related pixels. Next, the VNIR and SWIR images were spatially co-registered to the VNIR spatial resolution and the masks that were created in the previous processing step were used to remove lichen-related pixels from the VNIR images.

The analysis of the characteristics of ferric absorption feature could begin once the lichen free pixels were located in the imagery of each sample. The absorption feature band depth and band position were calculated from the hull quotient of each lichen free pixel in the VNIR images spectrally subset to the wavelength range of 602-1002 nm. This range was chosen so as to account for the broad ferric absorption feature in this wavelength region. The band position and depth data sets were tested for outliers by applying a limit of three standard deviations separately to each data set. No outliers were detected in the band position set, whereas 1823 values were classified as outliers in the band depths data set. The spectra associated with these band depths (>

23.1 %) were also assessed to be of relatively low signal-to-noise and were thus left out of further analysis.

The end result is a set of lichen free pixel measurements that were subsequently grouped into sedimentary and mafic-ultramafic rocks to investigate the ferric related spectral properties of these rock types. Mafic and ultramafic rocks were grouped together due to the small number of mafic samples ($n=3$) and the spectral similarity of these rock types (Hunt et al. 1974) in this wavelength range.

The relationship between the ferric absorption feature band depths and band positions was further investigated by separately extracting all the spectra from the gossan surface areas with band depths between 0-10% and 10-20%. Spectra with band depths greater than 20% were left out of this analysis due to their small representation in the full dataset ($n=7080$, or: 1.7% of the total number of pixels). We then calculated an average, representative spectrum of the 0-10% and 10-20% band depth groups from the remaining 409391 pixels. The ferric absorption feature band positions of these two spectra (representing band depths groups 0-10% and 10-20%) were manually extracted to assess possible spectral shifts that take place as a function of changing band depths.

4.4.3 Processing of the airborne spectrometry

The airborne data were analyzed for the detection and characterization of gossans. For this purpose the spectral dimensionality of the image data was reduced to 27 bands (14 in the VNIR wavelength region and 13 in the SWIR wavelength region). The bands were chosen through careful analysis of the key spectral features of the rock samples collected from the study area. Twenty-three image endmembers were chosen and labeled from a set of 590 candidate

endmembers extracted using the SSEE application using knowledge on the spectral properties of rock units and other image components in the study area. These endmembers encompass gossans (7), other rock types (7), vegetation (6), snow (2) and water (1). The gossan endmembers comprise representatives of the various gossan signatures obtained for the study area. These endmembers were subsequently used as input into the ISMA to unmix the airborne image resulting in twenty three fractional abundance images. Isolated pixels (e.g. lacking spatial continuity) are not likely to represent gossan outcrops and were removed from the abundance images. Based on the abundance images a minimum threshold of 0.3609 was set separately for each gossan abundance image ($n=7$). This threshold value was derived from the seven gossan abundance fraction images (as one standard deviation: 0.1182, from the mean) and aimed at highlighting the map distribution patterns by displaying the spectrally purest gossans while minimizing false positives.

To gain an insight into the mineralogy of the gossan endmember spectra, these were first compared to spectra of iron oxide minerals selected from the USGS library (Clark et al. 2007). Goethite, hematite, lepidocrocite and magnetite were chosen for this analysis due to their presence in the gossan sample set (see XRD results, Table 4.1). The gossan image endmembers were also compared to laboratory spectra acquired from the lichen-free areas of samples (see section 4.3.3.1 for details). The objective of this analysis was to assess the rock substrates by comparing the spectral features of the airborne spectra to the spectral features of samples of known mineralogy established through XRD analysis. In both instances comparisons were conducted by means of the Spectral Angle Mapper (SAM) algorithm (Kruse et al. 1993) with each spectrum assigned a score between 0 and 1. Higher SAM values reflect increasing similarity between two spectra (Kruse and Lefkoff 1999) such that values close to or equal to one suggest a

perfect similarity between the shapes of these spectra. Both the USGS library spectra and the laboratory spectra were re-sampled to the sampling interval of the airborne spectra (27 bands) prior to applying the SAM algorithm. When comparing the gossan endmembers to the USGS spectral library, only the wavelength range between 436 nm and 1169 nm was considered to highlight the spectral features of the iron oxide minerals in the VNIR wavelength region. Contrary to this, the full wavelength range (436-2389 nm) was used when comparing the airborne gossan endmembers to the spectra obtained from the gossan samples because in this analysis both the iron oxide (VNIR wavelengths) and the rock substrate mineralogies (SWIR wavelengths) were used in comparisons. Furthermore, the spectral similarity between the airborne gossan endmembers and the non-gossan samples was assessed using the 2112-2389 nm wavelength region that retains the spectral signature of many infrared active minerals.

4.5 RESULTS

4.5.1 Ferric absorption for the weathered surfaces of the gossan samples

The frequency distribution of the band depth and band position of the ferric absorption extracted from the SisuRock sample imagery are shown on figure 4.3. Data for the band position display a bimodal distribution (Fig. 4.3A) with peaks near 886 nm and 909 nm. In contrast, the band depth data set is unimodal and approximates more closely a normal distribution (Fig. 4.3B). Due to the non-normal data distribution of the ferric absorption feature band positions data set, the correlation between the band positions and the band depths was assessed using the Spearman rank correlation test (instead of the Pearson's correlation test). A weak correlation (Spearman's $\rho = -0.113$, $n = 416234$, $p = 0.000$, two-tailed, 99 % confidence level) was observed between the band depths and band position datasets across all rock types.

The relationship between the position and the depth of the ferric absorption was further evaluated separately for sedimentary rocks as a group and mafic and ultramafic rocks as another group. More specifically, this was done by comparing the average band positions of the 0-10% and 10-20% band depth range groups. The premise is that the effects of the rock substrate vary with the transparency of the gossan to bedrock. The results, shown in Figures 4.4A-D and Table 4.2, suggest that decreasing band depths are associated with a spectral shift toward longer wavelengths. This spectral shift is 19 nm in the sedimentary rocks (Figs. 4.4A,B), and 22 nm in the mafic and ultramafic rocks (Figs. 4.4C,D). Thus decreasing ferric absorption feature band depths are associated with increasing ferric absorption feature band positions. This relationship was observed as a statistically significant, inverse correlation explained by the optically thin (< 50 μm ; Buckingham and Sommer 1983) nature of thin gossans resulting in a progressive influence of the rock substrate. Thinner gossans are indicated by lower ferric absorption feature band depths correlated with a spectral shift toward longer wavelengths. The observed spectral shift was slightly more pronounced in the mafic/ultramafic rocks than in the sedimentary rocks, which relates to the greater amount of ferromagnesian minerals in these rocks.

4.5.2 Synthetic spectral mixtures of gossans and non-gossans

The results obtained through synthetic mixtures of gossans and non-gossans support the observations extracted from sample imagery in the previous section. A systematic shift of the ferric absorption toward longer wavelengths is observed with increasing amount of non-gossans in the spectral mixture (Figs. 4.5A-F). When comparing the ferric absorption feature band position of a "pure" (100 %) gossan to a fifty-fifty (50 % gossan - 50 % non-gossan) mixture of gossans and non-gossans, it is furthermore evident that this effect is more pronounced for the

mafic and ultramafic rocks than for the sedimentary rocks. Specifically, there is an average spectral shift of 9 nm toward longer wavelengths for the sedimentary rocks, whereas the shift for the mafic and ultramafic rocks is 13 nm and 24 nm, respectively (Figs. 4.5A-F, Table 4.3).

When working with powders, Singer (1981) concluded that an increasing amount of ferromagnesian minerals in a mineral powder mixture of iron oxide and ferromagnesian minerals induces a spectral shift toward longer wavelengths in the ferric absorption feature. These observations are here reiterated for natural surfaces, in this instance gossans as thin films over a range of bedrock substrates.

4.5.3 Synthetic spectral mixtures of gossans and lichens

Synthetic mixtures of gossans and lichens (Figs. 4.6A-F) were used to estimate the effects of lichens on the position of the ferric absorption feature of gossans. A systematic shift of the ferric absorption toward shorter wavelengths is observed with increasing amount of lichen in the spectral mixture regardless of the rock type. The spectral shift between an unmixed (100% gossan) and mixed (fifty-fifty mixture) is greatest (35 nm) for the mafic gossans and of 15 nm and 18 nm for the sedimentary and ultramafic gossans, respectively. On average, the spectral shift is 23 nm toward shorter wavelengths for all rock types (Table 4.4).

Thus the mixing of gossans and lichens synthesized in this study would suggest that mixing should induce a general shift of the ferric absorption feature toward shorter wavelengths. However, lichens have distinct spectral characteristics in the VNIR wavelength region (Ager and Milton 1987, Petzold and Goward 1988) and although care was taken here to include different kinds of lichens, our data may not account for the full spectral variability of lichens. For this reason, it can only be concluded that spectral mixing between lichens and the iron oxide minerals

of gossans induces a general spectral shift toward shorter wavelengths, albeit the magnitude and direction of this shift may depend on the iron oxide mineralogy and specifics of the lichen community composition.

4.5.4 Airborne spectrometry

4.5.4.1 Comparison of gossan image endmembers with laboratory spectra

The seven airborne gossan endmembers showing ferric iron absorption features are shown in Figure 4.7 and they display spectral variation both in the VNIR (436-1169 nm) and SWIR (2112-2389 nm) wavelength regions. When a comparison is conducted in the VNIR region with iron oxide mineral spectra of the USGS spectral library the results suggest that the airborne gossan endmembers G1, G3, G5 and G7 are spectrally similar to hematite (SAM similarity score: 0.828-0.895), whereas gossan endmembers G2, G4 and G6 are similar to goethite (SAM similarity score: 0.829-0.879). These results, listed in Table 4.5, suggest that hematite and goethite are the predominant iron oxide minerals of the gossan endmembers.

When examined in the SWIR, airborne gossan endmember G1 has a subtle feature near 2280 nm, possibly indicative of jarosite, and endmembers G2, G5 and G7 have a distinct absorption feature near 2313-2326 nm. Rogge et al. (2104) reported cation-OH features (Hunt and Salisbury 1970; Hunt et al. 1974) for antigorite (2285, 2325 nm), actinolite (2245, 2315 nm) and clinocllore (2345 nm) consistent with serpentine, amphibole and chlorite group minerals abundantly present in the mafic and ultramafic sample set (see Table 4.1 for details). The presence of a distinct feature implies that these are thin gossans. Endmembers G3 and G4 do not display distinct absorption features in the SWIR wavelength region implying that they represent thick gossans. Endmember G6 has an Al-OH absorption feature near 2200 nm best explained by

the presence of mica or clay group minerals (Hunt and Salisbury 1970) and thus a sedimentary substrate. These observations are consistent with results obtained from a comparison between the airborne gossan endmembers and laboratory spectra of the non-gossan samples having SAM similarity scores exceeding 0.941 (Figs. 4.7A-G). Endmembers G2, G5 and G7 have distinct SWIR features that best match that of the ultramafic samples (Figs. 4.7B,E,G). Endmember G6 (Fig. 4.7F) has no equivalent in the sample set.

4.5.4.2 Map distribution of gossan image endmembers

The gossan endmembers were overlain on a regional geological map (Rogge et al. 2014; Figure 4.8B) to examine their context with the lithological units for this part of the Cape Smith Belt. Endmembers interpreted to represent thick gossans (G1, G3, G4), on the basis of having no distinct SWIR feature, display a spatial distribution that encompasses known occurrences of such gossans. These include: 1) clusters of endmembers G1, G3 and G4 associated with sediments that lie between the mafic and ultramafic units (e.g. A on Fig. 4.8B), 2) endmember G4 occurrences along river beds (e.g. B on Fig 4.8B), and 3) endmember G1 and G4 occurrences at the base of ultramafic units (e.g. C on Fig 4.8B). Endmembers interpreted to represent thin gossans (G2, G5, G6, G7) based on presence of distinct SWIR features are spatially associated with: 1) sediments (G6; D on Fig. 4.8B), 2) pyroxenites/peridotites (G7; e.g. E on Fig 4.8B) along the perimeter of ultramafics, 3) restrictive occurrences within mafic rocks (G5; F on Fig 4.8B), and 4) primarily along the perimeter of ultramafics with some occurrences along a river bed (G2; G on Fig 4.8B). Given that mineralization is observed in the area in gossans occurring along the perimeter of ultramafics, the detection of G2 and G7 gossan endmembers is of particular interest for exploration.

4.6 DISCUSSION

4.6.1 Pitfalls in the use of iron feature characteristics for the spectral identification of gossans

This study highlights challenges that can emerge in northern environments in attempting the spectral identification of gossans from the detection of iron oxide minerals in hyperspectral imagery. First the presence of rock encrusting lichens induces a general spectral shift of the iron absorption toward shorter wavelengths while the opposite shift is observed due to the influence of the rock substrates for thin gossans. Though these effects will not typically impact the detection of gossans in hyperspectral and many multispectral data (e.g. WorldView-2), in particular the most extensive gossans (e.g. typically thick gossans), they can impede further classification of thin gossans based on their iron oxide mineralogy. The later can be attempted with hyperspectral imagery keeping in mind that these effects may impact the interpretation of mineralogy.

4.6.2 Merits of hyperspectral imaging for gossan detection and value for exploration

The analysis of the airborne hyperspectral imagery has revealed the presence of a number of gossan classes distinct in their spectral characteristics and map distribution. Each class can be interpreted as representing either a thick gossan, whose spectrum is largely devoid of SWIR absorption features, or a thin gossan with a spectrum retaining the influence of bedrock mineralogy. Thick gossans are typically spatially extensive and are readily captured in satellite multispectral data spanning a range of spatial resolutions. However this study demonstrated that thin gossans could also be detected in hyperspectral imagery and separated into distinct classes associated with bedrock type. In the Cape Smith belt thin gossans are typically of limited spatial extent and are not readily found during field mapping. Their detection is of significance for

mineral exploration because they can lead to the detection of subsurface mineralization. The ability to define distinct classes of thin gossans is also significant since, as observed in the Cape Smith belt, thin gossans associated with specific substrates (e.g. pyroxenites and peridotites) are of greater interest for exploration. Access to high spectral resolution data thus offers expanded opportunities for the detection of gossans in northern environments and their use for targeted exploration efforts.

4.7 CONCLUSIONS

Several studies have documented the remotely sensed detection of gossans (e.g. thick) from a variety of platforms. This study has documented that thin gossans can also be detected and discriminated from thick gossans, and further broken down into several classes associated with bedrock type. The ability to define distinct classes of thin gossans is significant since the association of thin gossans with specific rock substrates can be exploited for exploration.

In northern environments where rock-encrusting lichens abound on rock outcrops, the presence of lichens on thin gossans induces a general spectral shift towards shorter wavelengths of the iron absorption typical of gossan spectra. The opposite shift is observed due to the influence of the rock substrate. These effects can thus impede classification of gossans based on the iron oxide mineralogy interpreted from spectra.

TABLE 4.1. Minerals identified by XRD (gossan sample set).

	A	B	C	D	E	F	G	H	I	J	K	L	M
Sed. Rocks													
Sample 1			X					X			X		
Sample 5			X			X		X	X		X		
Sample 6							X		X		X		
Sample 7		X						X	X		X		X
Sample 11			X			X		X			X		
Sample 13							X				X		X
Sample 14			X			X		X			X		
Sample 16	X					X	X				X		X
Sample 22								X					X
Sample 23						X		X			X		
Mafic rocks													
Sample 17			X		X	X						X	
Sample 18			X		X	X						X	
Sample 20	X		X		X	X		X					
Ultram. rocks													
Sample 2	X		X										
Sample 3			X							X	X		
Sample 4	X		X								X		
Sample 8	X		X									X	
Sample 9	X		X	X									
Sample 10	X		X	X									
Sample 12	X		X	X								X	
Sample 15	X		X				X					X	
Sample 19	X	X	X									X	
Sample 21	X									X			

Columns: A=Amphibole group; B=Carbonate group; C=Chlorite group; D=Cordierite group; E=Epidote group; F=Feldspar group; G=Iron oxide group; H=Mica group; I=Other phyllosilicates; J=Pyroxene

group; K=Quartz; L=Serpentine group; M=Sulfide group; Abbreviations: Sed.=sedimentary, Ultram.=ultramafic. Amphibole group minerals: actinolite, fluoromagnesiorichterite and magnesiohornblende. Carbonate group minerals: calcite and dolomite. Chlorite group minerals: clinocllore and chamosite. Epidote group minerals: epidote and clinozoisite. Feldspar group minerals: albite, anorthite, orthoclase and microcline. Iron oxide group minerals: hematite, goethite, lepidocrocite and magnetite. Mica group minerals: muscovite, phengite, phlogopite and margarite. Other phyllosilicates: vermiculite, minnesotaite and stilpnomelane. Pyroxene group minerals: enstatite, diopside. Serpentine group minerals: antigorite, cronstedtite and tremolite. Sulfide group minerals: pyrite, pyrhotite and marcasite.

TABLE 4.2. The average band position (in nm) of the 0-10 % and 10-20 % band depth ranges per rock type, and the spectral shifts calculated as the difference between these band depths (0-10%-10-20%).

	0-10 %	10-20 %	Spectral shift (nm)
All rock types	909	890	19
Sedimentary rocks	909	890	19
Mafic and ultramafic rocks	912	890	22
Average difference			20

TABLE 4.3. The results of synthetic mixtures of gossans and non-gossans. The values given in the table are for unmixed and mixed (gossan - non-gossan) ferric/ferrous absorption feature band positions (in nm); diff.=difference, gos.=gossan, n.-gos.=non-gossan, sedim.=sedimentary, ultram.=ultramafic.

	100% gos.-0% n.-gos.	75% gos.-25% n.-gos.	50% gos.-50% n.-gos.	25% gos.-75% n.-gos.	0% gos.-100% n.-gos.	Diff. 50% gos.-100% gos.
Sedim. rocks	952	958	961	963	989	9
Mafic rocks	1019	1023	1032	1047	1158	13
Ultram. rocks	962	974	986	1010	1052	24
Average diff.						15

TABLE 4.4. The results of synthetic mixtures of gossans and lichens. The values given in the table are for unmixed and mixed (rock-lichen) ferric absorption feature band positions (in nm). Lichens do not have a clear absorption feature in the near infrared wavelength region and hence no values are given for pure (100 %) lichens; diff.= difference, gos.=gossan, sedim.=sedimentary, ultram.=ultramafic.

	100% gos./0% lichen	75% gos./25% lichen	50% gos./50% lichen	25% gos./75% lichen	Diff. 100% gos.-50% gos.
Sedim. gossan, lichen	952	948	937	932	15
Mafic gossans, lichen	1019	1006	984	938	35
Ultram. gossan, lichen	962	957	944	931	18
Average difference					23

TABLE 4.5. The results of the Spectral Angle Mapper (SAM) similarity comparisons between the airborne gossan endmembers (G1-G7) and the iron oxide minerals (goethite, hematite, lepidocrocite and magnetite) of the USGS spectral library (Clark et al., 2007). SAM similarity scores range from 0 (no match) to 1 (a perfect match).

	goethite	hematite	lepidocrocite	magnetite
G1	0.799	0.869	0.783	0.600
G2	0.858	0.796	0.733	0.651
G3	0.804	0.895	0.816	0.566
G4	0.829	0.719	0.664	0.659
G5	0.810	0.857	0.791	0.603
G6	0.879	0.802	0.703	0.698
G7	0.788	0.828	0.740	0.576

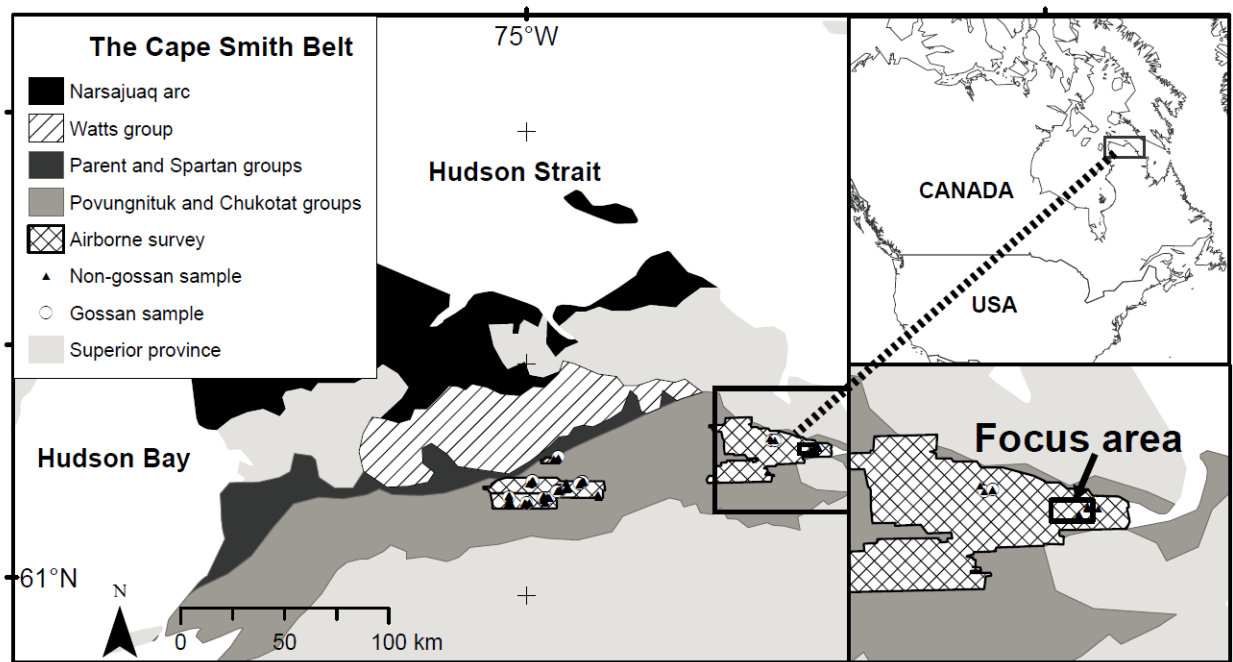


FIGURE 4.1. The locations of the samples and the airborne survey in the context of the tectonic elements of the Ungava peninsula. The tectonic units are modified after St-Onge and Lucas (1993). Inset figure: A focus area for airborne data analysis.

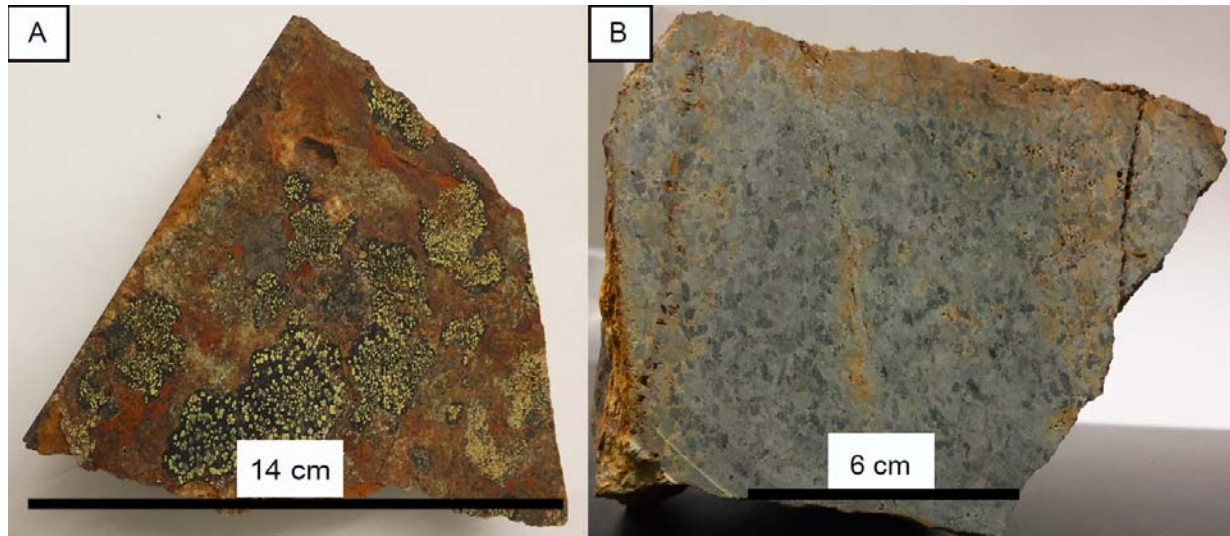


FIGURE 4.2. An ultramafic gossan sample: A) a weathered surface; B) a fresh cut surface.

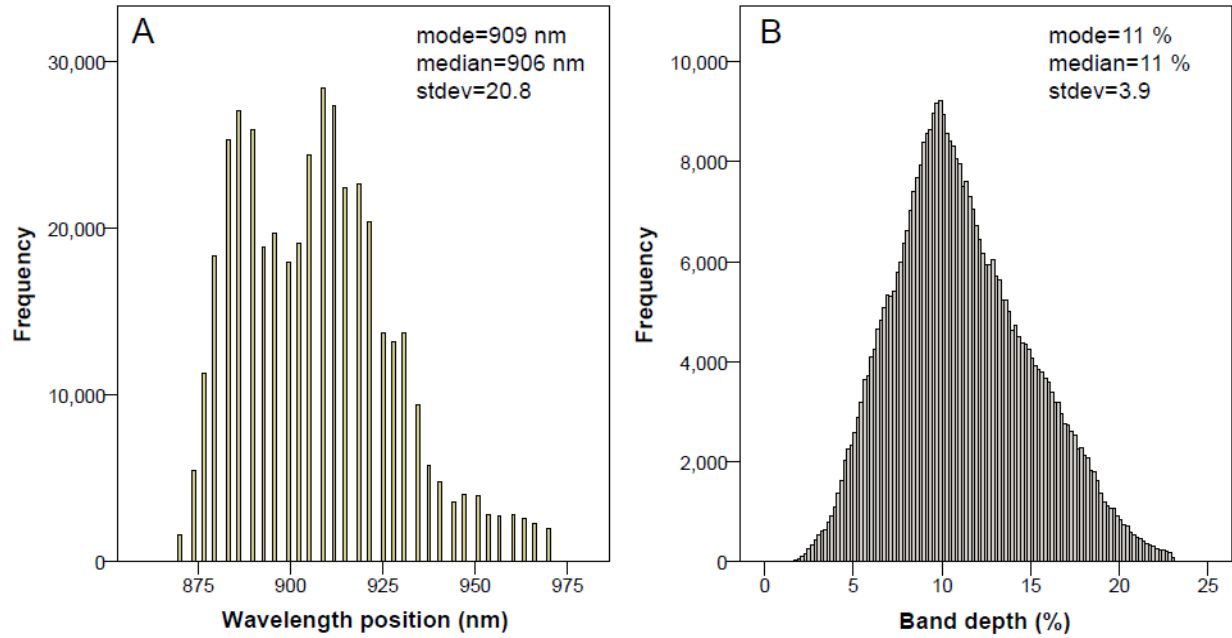


FIGURE 4.3. The frequency distribution (n=423314) of the ferric iron absorption band position (A) and band depth (B) acquired by means of a sample imagery.

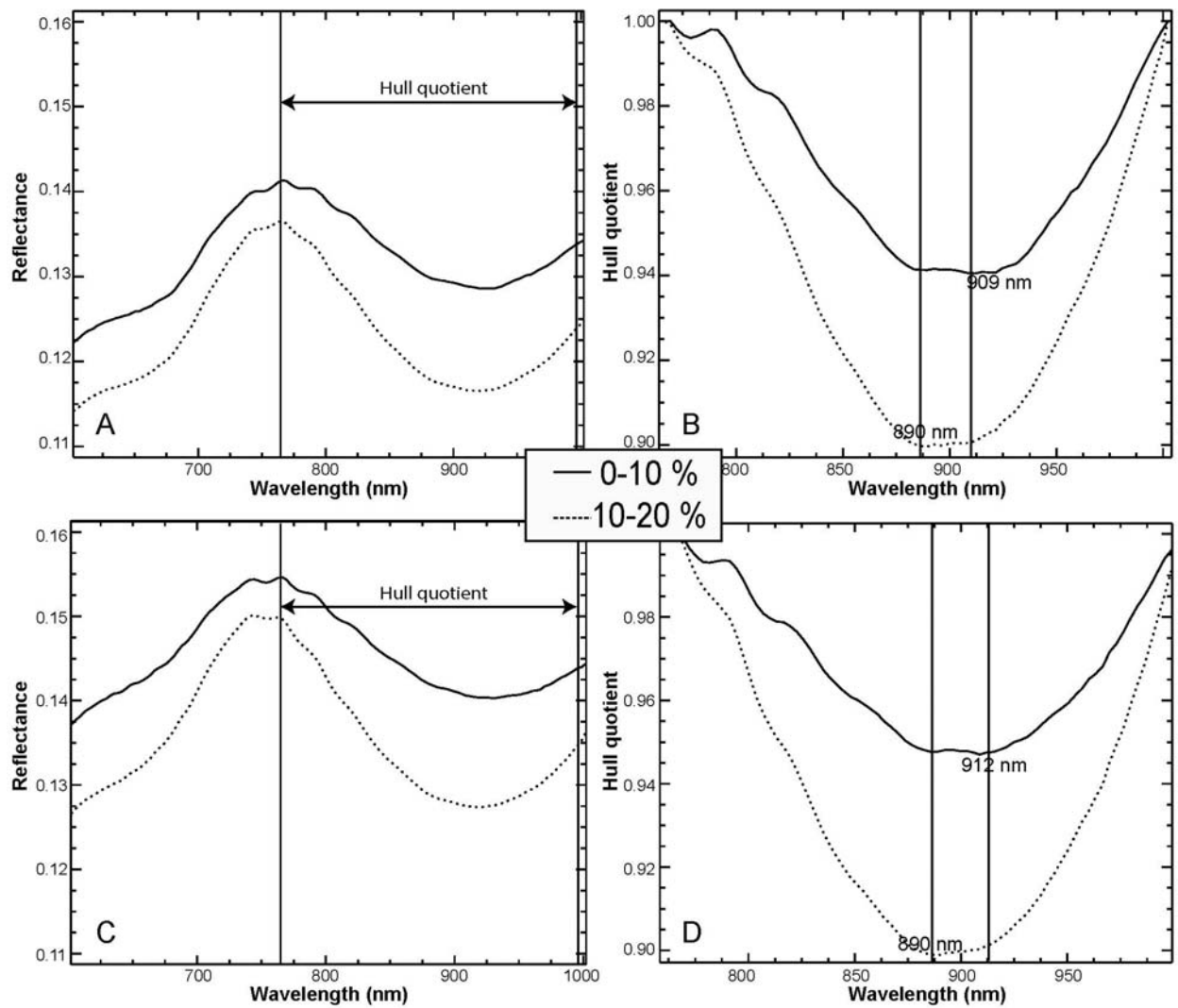


FIGURE 4.4. The averaged spectra of the 0-10 % and 10-20 % band depths for sedimentary rocks (A) and the corresponding hull quotient and band center (B); the averaged spectra of the 0-10 % and 10-20 % band depths for mafic and ultramafic rocks (C) and the corresponding hull quotient and band center (D).

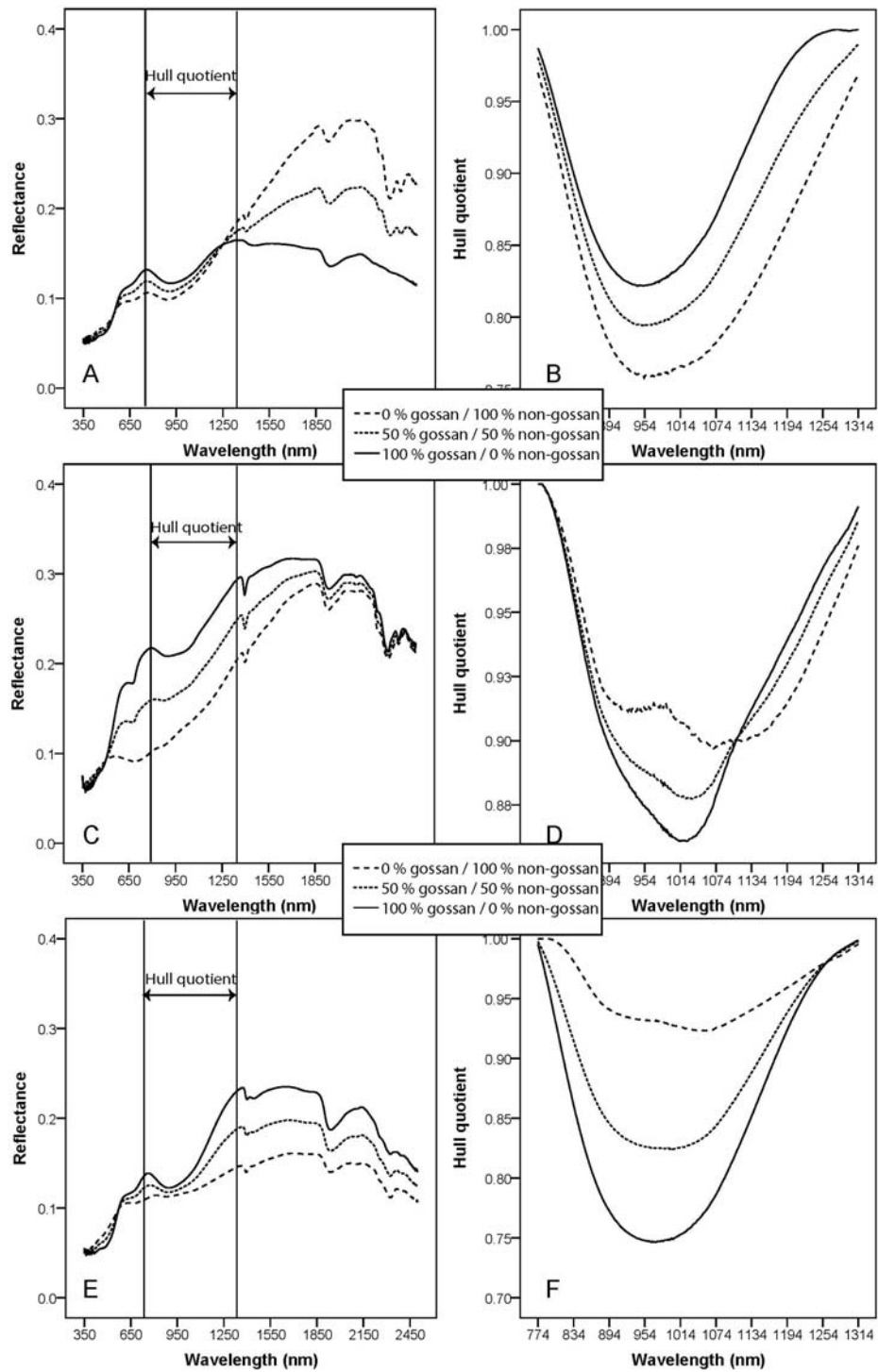


FIGURE 4.5. Synthetic spectral mixtures of gossan and non-gossans for sedimentary rocks (A) and related hull quotient spectra (B); for mafic rocks (C) and related hull quotient spectra (D); and for ultramafic rocks (E) and related hull quotient spectra (F).

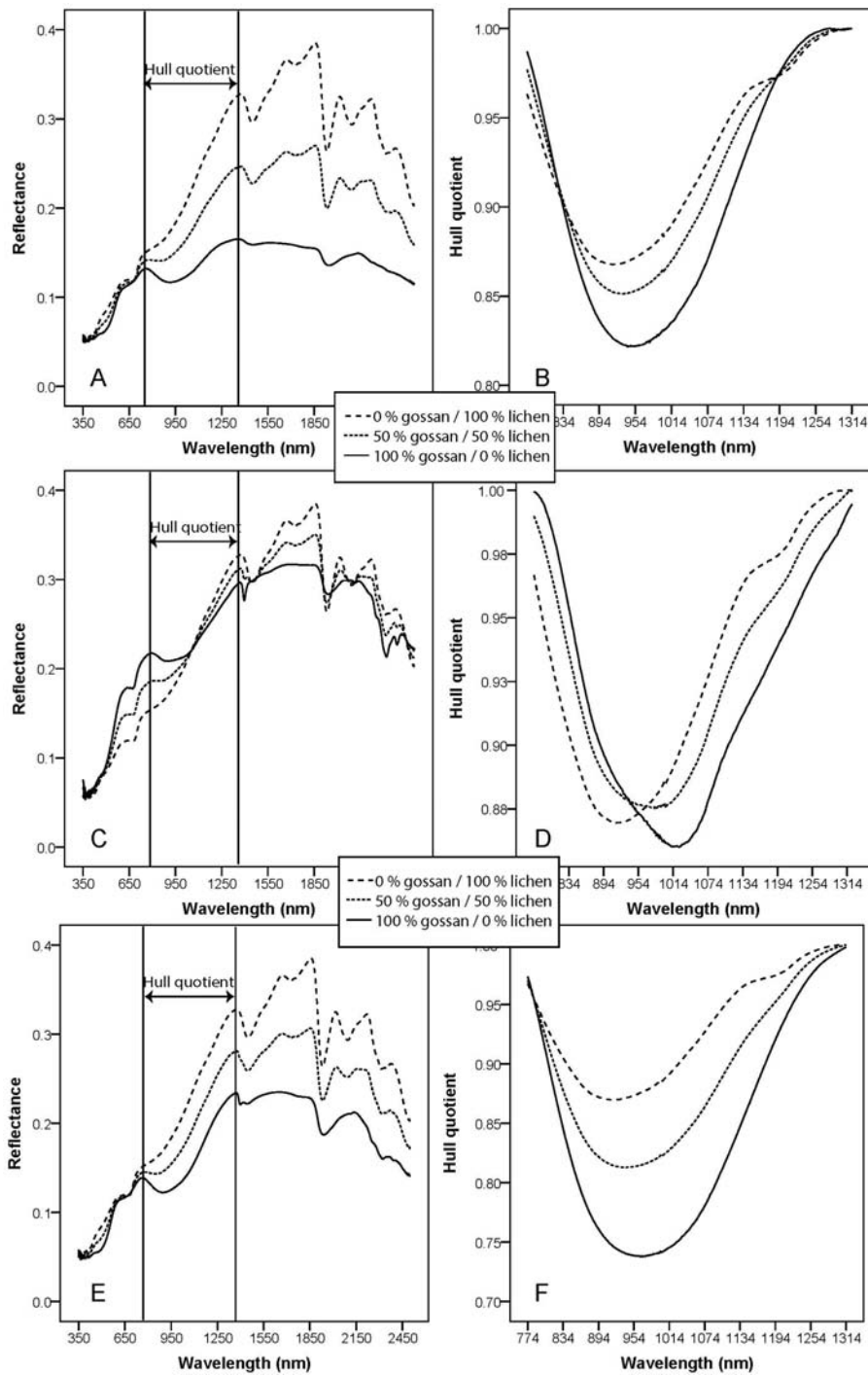


FIGURE 4.6. Synthetic spectral mixtures of gossan and lichen for sedimentary gossan (A) and related hull quotient spectra (B); for mafic gossan (C) and related hull quotient spectra (D); and for ultramafic gossan (E) and related hull quotient spectra (F).

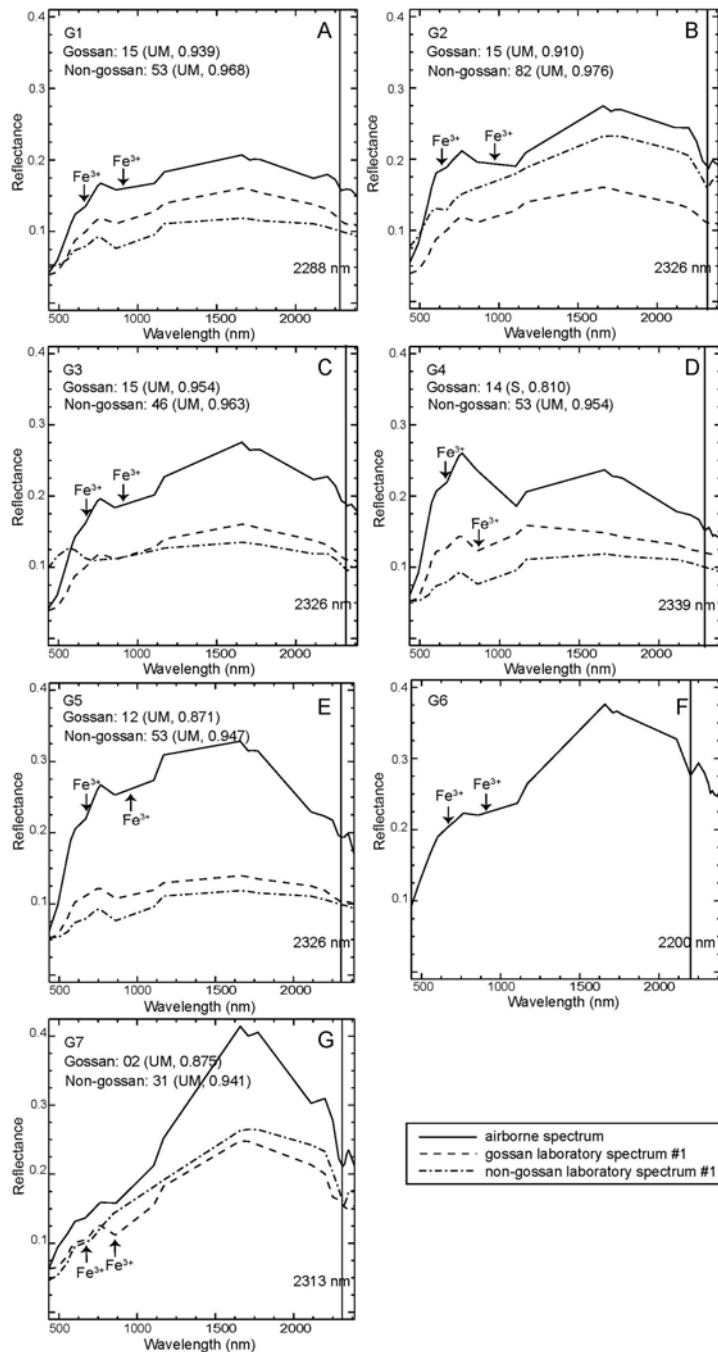


FIGURE 4.7. A comparison of airborne gossan endmembers (A-G as endmembers G1-G7) with laboratory spectra from samples. Each frame displays the gossan and non-gossan sample spectra of highest similarity score (as measured by SAM). Endmember G6 (Frame F) has no spectrally similar laboratory equivalent. The number refers to the sample number followed in brackets by the SAM similarity score. S=sedimentary sample, UM=ultramafic sample.

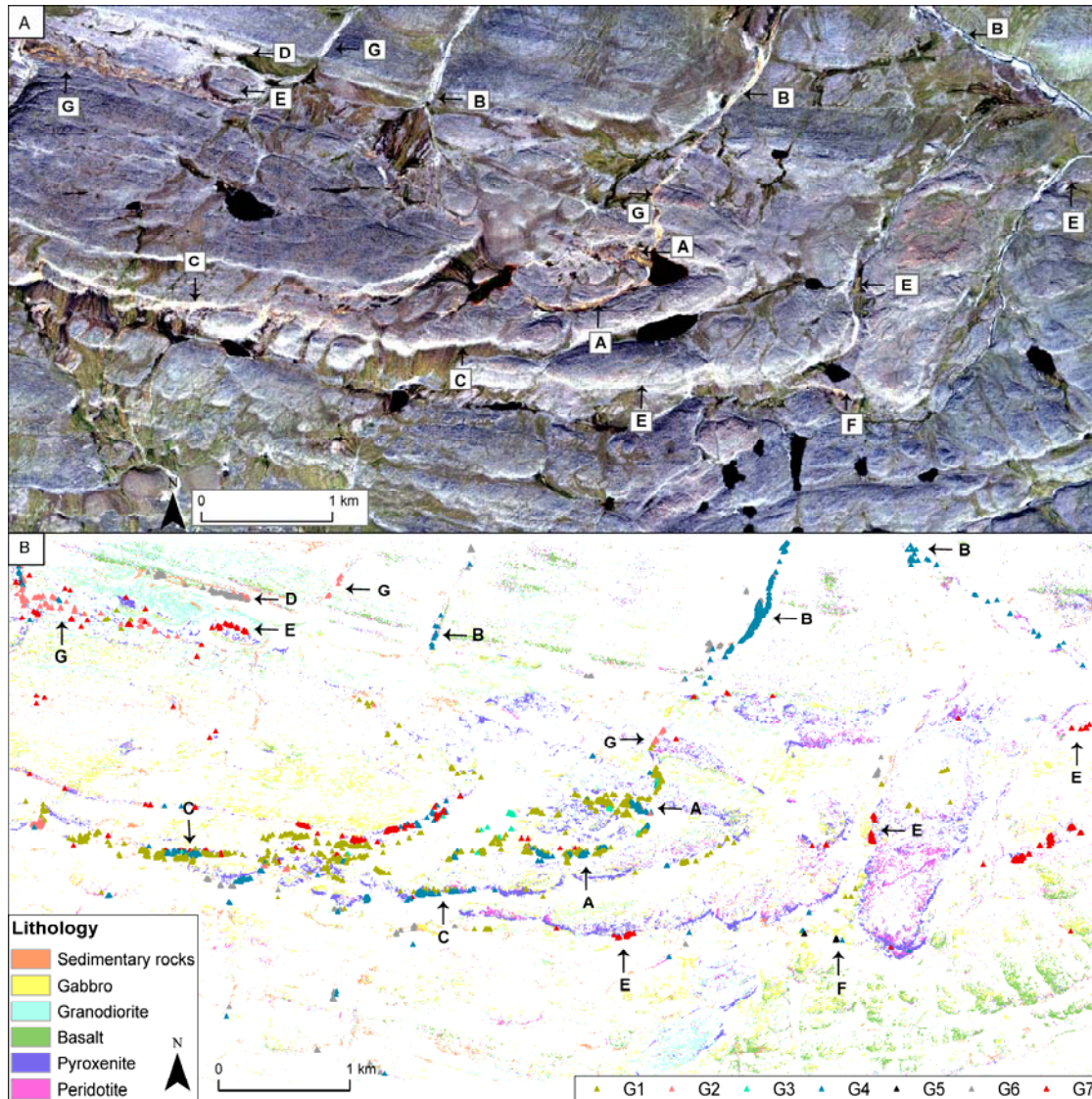


FIGURE 4.8. A true color composite (R: 641 nm, G: 546 nm, B: 463 nm) of the "focus area" (A) and the spatial distribution of the airborne gossan endmembers (G1-G7) shown in the context of a thematic geological map by Rogge et al. (2014) (B). The letters A-G refer to clusters of different airborne gossan endmembers. A: clusters of endmembers G1, G3 and G4 associated with sediments that lie between the mafic and ultramafic units; B: endmember G4 occurrences along river beds; C: endmember G1 and G4 occurrences at the base of ultramafic units; D: sediments associated with the endmember G6; E: occurrences of the endmember G7 associated with the pyroxenite/peridotite rock outcrops; F: restrictive occurrences of the endmember G5 within mafics rocks; G: rock outcrops associated with the endmember G2, primarily along the perimeter of ultramafics with some occurrences along a river bed.

LITERATURE CITED

- Abdelsalam, M.G., Stern, R.J. and Berhane, W.G., 2000. Mapping gossans in arid regions with Landsat TM and SIR-C images: the Beddaho alteration zone in northern Eritrea. *Journal of African Earth Sciences* 30: 903–916.
- Ager, C.M. and Milton, N.M., 1987. Spectral reflectance of lichens and their effects on the reflectance of rock substrates. *Geophysics* 52: 898–906.
- Bechtel, R., Rivard, B. and Sánchez-Azofeifa, A., 2002. Spectral properties of foliose and crustose lichens based on laboratory experiments. *Remote Sensing of Environment* 82: 389–396.
- Bellott, A., Corpel, J. and Millon, R., 1991. Contribution of magnetic modeling to the discovery of a hidden massive sulfide body at Hajar, Morocco. *Geophysics* 56: 983–991.
- Bierwirth, P., Huston, D. and Blewett, R., 2002. Hyperspectral mapping of mineral assemblages associated with gold mineralization in the Central Pilbara, Western Australia. *Economic Geology* 97: 819-826.
- Bruegge, C.J., Stiegman, A.E., Rainen, R.A. and Springsteen, A.W., 1993. Use of Spectralon as a diffuse reflectance standard for in-flight calibration of earth-orbiting sensors. *Optical Engineering* 32: 805–814.
- Buckingham, W.F. and Sommer, S.E., 1983. Mineralogical characterization of rock surfaces formed by hydrothermal alteration and weathering - application to remote sensing. *Economic Geology* 78: 664–674.

- Clark, R.N., Swayze, G.A., Wise, R., Livo, E., Hoefen, T., Kokaly, R. and Sutley, S.J., 2007. USGS digital spectral library splib06a: U.S. Geological Survey, Digital Data Series 231 (<http://speclab.cr.usgs.gov/spectral.lib06>).
- Cornell, R.M. and Schwertmann, U., 2003. The iron oxides: Structure, properties, reactions, occurrences and uses. Wiley-VCH GmbH & Co., Weinheim, Germany.
- Dillon-Leitch, H.C.H., Watkinson, D.H. and Coats, C.J.A., 1986. Distribution of Platinum-Group Elements in the Donaldson West Deposit, Cape Smith Belt, Quebec. *Economic Geology* 81: 1147-1158.
- Giovenazzo, D., Picard, C. and Guha, J., 1989. Tectonic setting of Ni-Cu-PGE deposits in the central part of the Cape Smith Belt. *Geoscience Canada* 16: 134–136.
- Hunt, G.R. and Salisbury, J.W., 1970. Visible and near-infrared spectra of minerals and rocks: I Silicate minerals. *Modern Geology* 1: 283–300.
- Hunt, G.R. and Salisbury, J.W., 1976. Visible and near infrared spectra of minerals and rocks: XI. Sedimentary rocks. *Modern Geology* 5: 211–217.
- Hunt, G.R., Salisbury, J.W. and Lenhoff, C.J., 1971. Visible and near infrared spectra of minerals and rocks: III. Oxides and hydroxides. *Modern Geology* 2: 195–205.
- Hunt, G.R., Salisbury, J.W. and Lenhoff, C.J., 1974. Visible and near infrared spectra of minerals and rocks: IX. Basic and ultrabasic igneous rocks. *Modern Geology* 5: 15–22.
- Hynes, A. and Francis, D.M., 1982. A transect of the Early Proterozoic Cape Smith foldbelt, New Quebec. *Tectonophysics* 88: 23–59.
- Krauskopf, K.B., 1967. Introduction to geochemistry. McGraw-Hill Book Company, New York, USA.

- Kruse, F.A. and Lefkoff, A.B., 1999. Analysis of spectral data of manmade materials, military targets, and background using an expert system based approach. Proceedings of ISSSR (International Society for Strategic Studies in Radiology), Las Vegas, USA: 339–350.
- Kruse, F.A., Lefkoff, A.B., Boardman, J.W., Heidebrecht, K.B., Shapiro, A.T., Barloon, P.J. and Goetz, A.F.H., 1993. The Spectral Image Processing System (SIPS)-interactive visualization and analysis of imaging spectrometer data. *Remote Sensing of Environment* 44: 145–163.
- Leshner, C.M., 2007. Ni-Cu-PGE deposits in the Raglan area, Cape Smith Belt, New Quebec. In: Goodfellow, W.D. (ed.): *Mineral Deposits of Canada. A synthesis of major deposit types, district metallogeny, the evolution of geological provinces and exploration methods.* Special Publication no. 5, Geological Association of Canada, Ottawa, Canada: 351–386.
- Longton, R.E., 1988. *Biology of polar bryophytes and lichens.* Cambridge University Press, Cambridge, UK.
- Lydon, J.W., 2007. An overview of the economic and geological contexts of Canada's major mineral deposit types. In: Goodfellow, W.D. (ed.): *Mineral Deposits of Canada. A synthesis of major deposit-types, district metallogeny, the evolution of geological provinces, and exploration methods.* Special Publication No. 5, Geological Association of Canada, Ottawa, Canada: 3–48.
- Machado, N., David, J., Scott, D., Lamothe, D., Philippe, S. and Gariépy, C., 1993. U-Pb geochronology of the western Cape Smith Belt, Canada: new insights on the age of initial rifting and arc magmatism. *Precambrian Research* 63: 211–223.

- Maria Dreher, A., Perez Xavier, R. and Luiz Martini, S., 2005. Fragmental rocks of the Igarapé Bahia Cu-Au deposit, Carajás mineral province. Brazil, *Revista Brasileira de Geociências* 35: 359–368.
- Modeland, S., Francis, D. and Hynes, A., 2003. Enriched mantle components in Proterozoic continental-flood basalts of the Cape Smith foldbelt, northern Québec. *Lithos* 71: 1–17.
- Parrish, R.R., 1989. U-Pb geochronology of the Cape Smith Belt and Sugluk block, northern Quebec. *Geoscience Canada* 16: 126–130.
- Payette, S., Morneau, C., Sirois, L. and Despons, M., 1989. Recent fire history of the northern Québec biomes. *Ecology* 70: 656–673.
- Petzold, D.E. and Goward, S.N., 1988. Reflectance spectra of subarctic lichens. *Remote Sensing of Environment* 24: 481-492.
- Purvis, O.W. and Halls, C., 1996. A review of lichens in metal-enriched environments. *Lichenologist* 28: 571-601.
- Richter, R. and Schläpfer, D., 2002. Geo-atmospheric processing of airborne imaging spectrometry data. Part 2: Atmospheric/topographic correction. *International Journal of Remote Sensing* 23: 2631-2649.
- Rivard, B. and Arvidson, R.E., 1992. Utility of imaging spectrometry for lithologic mapping in Greenland. *Photogrammetric Engineering & Remote Sensing* 58: 945–949.
- Rogge, D.M. and Rivard, B., 2010. Iterative spatial filtering for reducing intra-class spectral variability and noise. 2nd Workshop on Hyperspectral Image and Signal Processing: Evolution in Remote Sensing (WHISPERS), Reykjavik, Iceland: 1–4.

- Rogge, D., Rivard, B., Segl, K., Grant, B. and Feng, J., 2014. Mapping of Ni-Cu-PGE ore hosting ultramafic rocks using airborne and simulated EnMap hyperspectral imagery, Nunavik, Canada. *Remote Sensing of Environment* 152: 302-317.
- Rogge, D.M., Rivard, B., Zhang, J. and Feng, J., 2006. Iterative spectral unmixing for optimizing per-pixel endmember sets. *IEEE Transactions on Geoscience and Remote Sensing* 44: 3725-3736.
- Rogge, D.M., Rivard, B., Zhang, J., Sanchez, A., Harris, J. and Feng, J., 2007. Integration of spatial-spectral information for the improved extraction of endmembers. *Remote Sensing of Environment* 110: 287–303.
- Rowan, L.C., Goetz, A.F.H. and Ashley, R.P., 1977. Discrimination of hydrothermally altered and unaltered rocks in visible and near infrared multispectral images. *Geophysics* 42: 522–535.
- Scott, D.J., Helmstaedt, H. and Bickle, M.J., 1992. Purtuniqu ophiolite, Cape Smith belt, northern Quebec, Canada: A reconstructed section of Early Proterozoic oceanic crust. *Geology* 20: 173–176.
- Singer, R.B., 1981. Near-infrared spectral reflectance of mineral mixtures: systematic combinations of pyroxenes, olivine, and iron oxides. *Journal of Geophysical Research* 86: 7967– 7982.
- St-Onge, M.R. and Lucas, S.B., 1993. Geology of the eastern Cape Smith Belt: Parts of the Kangiqsujuaq, Cratère du Nouveau-Québec, and Lacs Nuvilik map areas, Quebec. Geological Survey of Canada Memoir 438, Ottawa, Canada.

- St-Onge, M.R., Lucas, S.B. and Parrish, R.R., 1992. Terrane accretion in the internal zone of the Ungava orogen, northern Quebec. Part 1: Tectonostratigraphic assemblages and their tectonic implications. *Canadian Journal of Earth Sciences* 29: 746–764.
- St-Onge, M.R., Scott, D.J. and Lucas, S.B., 2000. Early partitioning of Quebec: Microcontinent formation in the Paleoproterozoic. *Geology* 28: 323–326.
- Taylor, G.F., 1987. Near-infrared spectra of West Shasta gossans compared with true and false gossans from Australia and Saudi Arabia and trace element content of gossans at four mines in the West Shasta massive sulfide district - A discussion. *Economic Geology* 82: 230-234.
- Volesky, J.C., Stern, R.J. and Johnson, P.R., 2003. Geological control of massive sulfide mineralization in the Neoproterozoic Wadi Bidah shear zone, southwestern Saudi Arabia, inferences from orbital remote sensing and field studies. *Precambrian Research* 123: 235–247.
- West, L., McGown, D.J., Onstott, T.C., Morris, R.V., Suchecki, P. and Pratt, L.M., 2009. High Lake gossan deposit: An Arctic analogue for ancient Martian surficial processes? *Planetary and Space Science* 57: 1302–1311.

CHAPTER 5 – Discussion, summary of limitations, future research and conclusions

5.1 DISCUSSION

The mining industry faces growing demands to minimize the environmental footprint of mineral exploration and exploitation operations (Jenkins and Yakovleva 2006). These demands are particularly relevant in northern areas that have significant mineral potential, but which are also susceptible to environmental degradation. This is evident in areas such as the Taimyr Peninsula in Siberia, which suffers from contamination caused by mining and other industrial activities (Allen-Gil et al. 2003). Noninvasive and nondestructive remote sensing techniques have the potential to help bridge the gap between the demands of environmental awareness and cost-efficiency in mineral exploration. Detailed information can be extracted on the mineralogy and chemical composition of rocks by means of remote sensing imagery with high spatial and spectral resolution, potentially reducing the need to conduct field work in pristine northern environments. This is made possible by the distinct spectral fingerprints of different minerals, and variations of these fingerprints induced by subtle chemical compositional changes of minerals. The characteristic spectral shape of each mineral is determined by the electronic transition and vibrational processes (Hunt and Salisbury 1970) that operate in different parts of the electromagnetic spectrum when minerals interact with light.

However, remote sensing campaigns face challenges in high latitude regions. Arctic areas have little solar radiation for several months in a year and even in the summer the solar zenith angle is always a minimum of 60° at the highest latitudes and 43° at the Arctic Circle (Curry et

al. 1996). Another problem, specific to the geological applications of remote sensing, is the cryptogam cover of the rock outcrops. Tundra plants are well adapted to environmental extremes (Chapin 1983), and lichens do not generally allow for the transmission of light (Bechtel et al. 2002).

5.2 SUMMARY OF LIMITATIONS TO RESEARCH PROJECTS

Several aspects of my doctoral thesis are subject to limitations resulting from data availability, instrumental limitations and logistical aspects of field sampling.

5.2.1 Data availability

The number of samples given for electron microprobe analysis ($n=7$, Chapter 2) was limited by the available funds, and a larger number of samples could have provided statistically more robust results. Moreover, the number of drill cores ($n=28$) available for the investigation discussed in Chapter three was spatially confined to the immediate vicinity of the massive sulfide lenses. However, a spatially more extensive drill core data coverage would have been ideal as it would have enabled enhanced comparisons between the areas proximal and distal to the massive sulfide lenses. Moreover, the investigation discussed in Chapter four could have benefited from a greater amount of samples and field observations from the area that was used for airborne data analysis. Ideally these observations and samples would have been used to validate the results inferred from the airborne hyperspectral dataset.

5.2.2 Instrumental limitations

In Chapter four, the different spatial resolutions of the visible-near infrared (VNIR, 397-1002 nm) and short-wave infrared (SWIR, 928-2530 nm) cameras may have influenced the

results despite the efforts to co-register these two sets of images as accurately as possible. In practice, the SWIR images were used to mask out pixels associated with lichens from the VNIR images, but due to the lower spatial resolution of the SWIR images, it is possible that some lichen-infested pixels were left in the VNIR images.

Furthermore, the study discussed in Chapter four suffered from the lack of comprehensive XRD (X-Ray Diffraction) results on the mineralogy of gossans. More specifically, iron oxide minerals were not encountered in nineteen out of twenty-three gossan samples despite the visual and spectral observations confirming their presence in all the samples. This absence of the iron oxide minerals in the XRD results is probably due to the small proportion of the oxidized surfaces in the mineral powder samples that were delivered for XRD analysis. Care was taken to include both the oxidized surfaces of the gossans and their underlying host rock substrates in these mineral powders, but the proportion of gossans may not have been large enough for the detection of the iron oxide minerals. Optimally, both the mineralogy of the gossans and their host rock substrates would have been recorded by the x-ray diffractometer, which would have enabled comparisons between the iron oxide mineralogy, the host rock mineralogy and the spectrometry obtained from the oxidized and fresh surfaces of the samples.

Furthermore, the airborne data used in the study of Chapter four was compromised by the lack of bands between 863 nm and 1081 nm. These bands were left out from the airborne dataset due to some observed irregularities resulting from atmospheric correction, as discussed by Rogge et al. (2014). Unfortunately these bands coincide with a pronounced absorption feature of the iron oxide minerals (Cornell and Schwertmann 2003), used in the study to investigate the spectral properties of gossans. Ideally these bands (between 863 nm and 1081 nm) would have been

used to draw comparisons between the spectral properties of the airborne spectrometry and the sample spectrometry of gossans, had the quality of the airborne dataset allowed it.

5.2.3 Logistical aspects of field sampling

In all investigations (Chapters 2-4), logistics made the selection of field sites a challenge. All the field work in 2009, 2010, 2011 and 2013 were undertaken using helicopter support, which posed restrictions on the number and location of study sites. Moreover, the amount of samples that could be collected in the field was limited to what the helicopter could carry. In all cases the amount of time available for collecting samples and acquiring spectral measurements was confined to two weeks at a maximum, restricting the amount of ground spectral measurements to be acquired for the investigations discussed in this thesis. Another limiting factor for the collection of ground spectrometry was weather: no ground spectrometry was acquired during the rainy days.

5.3 CONTRIBUTIONS AND IMPLICATIONS FOR FUTURE RESEARCH

This doctoral dissertation addresses issues that are critical for the advancement of mineral exploration applications of hyperspectral remote sensing in high latitude regions. The research conducted demonstrates that irrespective of the environmental challenges posed by northern environments, hyperspectral remote sensing data can be used to guide mineral exploration.

5.3.1 Chapter Two: Application of airborne, laboratory and field hyperspectral methods to mineral exploration in the Canadian Arctic: recognition and characterization of volcanogenic massive sulfide-associated hydrothermal alteration in the Izok Lake deposit area, Nunavut, Canada

In this chapter ground, laboratory and airborne hyperspectral remote sensing data are used to estimate the spatial dimensions of the alteration zones surrounding the Izok Lake Zn-Cu-Pb-Ag deposit (65°45' N, 111°15' W, Nunavut, northern Canada). Moreover, the applicability of using the spectral properties of the white micas and biotite/chlorite for ore deposit vectoring is assessed.

The results discussed in this chapter indicate that the Al-OH wavelength positions of the white micas and the Fe-OH wavelength positions of the biotite/chlorite group minerals have spectral shifts in the vicinity of the Izok Lake deposit. According to the electron microprobe analysis results, these wavelength positions are directly related to the chemical composition of the white micas and biotite/chlorite. This chemical compositional variability is, in turn, associated with the temperature and chemical gradients of the deposit at the time of hydrothermal alteration. In case of the Izok Lake deposit, the environmental conditions at the time of ore deposit formation have resulted in the development of an area of relatively long Al-OH and Fe-OH absorption feature wavelength positions in the vicinity of the massive sulfide lenses. This area was observed both in the ground and airborne hyperspectral datasets. Furthermore, the results obtained by analyzing the hyperspectral airborne dataset were validated by comparing each Al-OH absorption feature wavelength position of this dataset to the spatially nearest Al-OH absorption feature wavelength position of the ground spectral dataset. This comparison revealed a

moderate accuracy of 65%, which can be explained through the dense vegetation and lichen cover of the study area. A total of 99% of the pixels associated with the rhyolitic rock outcrops of the study area had to be masked out from the airborne dataset because these pixels were estimated to be spectrally mixed with lichens and other vegetation. Despite this relatively low detection accuracy of the airborne spectrometry, the ability to detect an alteration zone both in the ground and airborne hyperspectral datasets suggest that hyperspectral airborne data can be used to delineate the hydrothermal alteration zones of VMS deposits in high latitudes. The detected alteration zone is interpreted to be a possible marginal discharge area of the massive sulfide lenses of the Izok Lake deposit. Hence the study discussed in this chapter provides new insights into the possible spatial dimensions of the massive sulfide lenses of the Izok Lake deposit, because these lenses develop in discharge areas. However, the Al-OH absorption feature wavelength positions of the study area do not show systematic trends with distance to the massive sulfide lenses, contrary to the Fe-OH absorption feature wavelength positions of the biotite/chlorite group minerals. This indicates that in the Izok Lake VMS deposit chlorite and biotite may serve as better vectors to the massive sulfide lenses than white micas. Nonetheless, the usefulness of biotite/chlorite group minerals for ore deposit vectoring is compromised by the inability to detect these minerals in the airborne dataset, as opposed to the white micas that could be detected. This is most likely a result of the smaller proportion of biotite/chlorite in the study area. In the broader context, the investigation discussed in Chapter two provides new information on the ability to use airborne hyperspectral remote sensing data for the detection of VMS related alteration zones in the subarctic and Arctic regions that are often characterized by abundant lichens on rock outcrops. Moreover, this investigation adds to the existing knowledge on the

applicability of the spectral properties of white micas and biotite/chlorite group minerals for ore deposit vectoring in VMS systems.

Future experiments should be designed to address the question of using the crystallinity of the white micas and chlorite group minerals to map hydrothermal alteration zones of VMS deposits. Changes in crystallinity have been shown to induce subtle differences in the spectral shape of e.g. the clay group minerals (Clark 1999), and the usability of this information for mineral deposit vectoring should be more systematically investigated. Moreover, the applicability of unmanned aerial vehicles (UAV) for the detection of hydrothermal alteration zones in high latitudes should be investigated. These vehicles have the potential to provide data with high spatial resolution and thus more opportunities to image vegetation free pixels, and technical issues related to operational data volumes are no longer a key obstacle.

5.3.2 Chapter Three: Short-wave infrared (SWIR) spectral and geochemical characteristics of hydrothermal alteration zones at the Archean Izok Lake Zn-Cu-Pb-Ag volcanogenic massive sulfide deposit, Nunavut, Canada: application in exploration target vectoring

Hydrothermal alteration indices, such as the Ishikawa index (Ishikawa et al. 1976) and the chlorite-carbonate-pyrite index (CCPI, Large et al. 2001) can be used to measure the alteration intensity variation of volcanogenic massive sulfide deposits. Similarly, the mineral chemistry of the alteration minerals, such as white micas and chlorite, can give indications on the temperature gradients of their formation environment (e.g. Cathelineau 1988, Duke 1994), associated with hydrothermal alteration and other metamorphic processes of different geological contexts. Previous attempts to correlate alteration indices with hyperspectral data (Herrmann et al. 2001,

Yang et al. 2011) have failed to demonstrate statistically significant relationships between the two. In this chapter I use ground and laboratory hyperspectral remote sensing data, combined with whole rock lithochemistry, to investigate the relationship between the alteration intensity variability, inferred from the alteration indices, and hyperspectral data. The results discussed in this chapter suggest that the hydrothermal alteration variation of the Izok Lake VMS deposit is accompanied by a systematic variation in the wavelength positions of the Al-OH absorption feature of the white micas and the Fe-OH absorption feature wavelength positions of biotite/chlorite. This relationship was encountered when the Fe-OH absorption feature wavelength positions of the ground and drill core spectral datasets were compared to the Ishikawa index and the chlorite-carbonate-pyrite index, respectively. Contrary to this, a statistically significant relationship was only found between the Al-OH absorption feature wavelength positions of the drill core spectrometry and the CCPI, and no relationship was found between the Al-OH absorption feature wavelength positions of the ground spectrometry and the Ishikawa index. These results offer new insights into the potential of hyperspectral remote sensing techniques for estimating the hydrothermal alteration intensity variation of VMS deposits. Moreover, the Al-OH and Fe-OH absorption feature wavelength positions of the hyperspectral ground and drill core datasets were interpolated to surfaces, and these visualizations were used to estimate the spectral variation of these absorption features in the deposit. The results suggest that the alteration core of the Izok Lake deposit is characterized by Al-rich white micas and Mg-rich biotite/chlorite. The alteration core is surrounded by a zone of relatively long Al-OH and Fe-OH wavelength positions, suggestive of Al-poor white micas and intermediate to Fe-rich biotite/chlorite. These patterns indicate possible influx of seawater into the deposit at the time of ore deposit formation, resulting in Mg-metasomatism in the vicinity of

the alteration core. These results provide new information on the possible formation history of the Izok Lake deposit.

As future work, the association encountered between the alteration indices and hyperspectral data should be extended to other VMS deposits to infer possible general trends. Such assessments could reveal similarities in VMS deposits of apparently distinct geochemical fingerprints. This information, in turn, could be used to guide future exploration efforts. In practice, airborne or spaceborne hyperspectral remote sensing data could be used to estimate the spatial patterns of the Al-OH and Fe-OH absorption features of the phyllosilicate minerals, and if this information could be put into the context of general hydrothermal alteration intensity variation patterns, exploration could be focused on the most promising areas of the highest alteration intensities. In VMS deposits such areas occur in the immediate vicinity of the massive sulfide lenses (German and Von Damm 2006).

5.3.3 Chapter Four: Enhanced detection of gossans using hyperspectral data: example from the Cape Smith Belt of northern Quebec, Canada

In this chapter I discuss the optical thickness properties of gossans and the influence of lichens and the host rock substrates on their spectral properties. These topics are investigated by means of hyperspectral laboratory and airborne remote sensing data from the Cape Smith Belt (60°43'N-62°35'N, 78°11'W-71°59'W, in Quebec, northern Canada) magmatic Ni-Cu-(PGE) deposit.

The results discussed in this chapter suggest that some gossans are optically thin, allowing the transmission of light into the host rock substrate. The implications are: i) the spectral features of gossans and their underlying host rock substrates can get spectrally mixed and ii) the spectral

properties of the underlying host rock substrates can be estimated by remote sensing means. The latter finding has particular importance in areas where there is a known association between specific rock types and mineral deposits. However, the spectral mixing between gossans and their host rock substrates was found to induce a spectral shift toward longer wavelengths in the ferric absorption feature. This shift can be explained through spectral mixing between the ferric absorption feature of gossans and the ferrous absorption feature of the host rock substrates. Because the ferrous absorption feature occurs at longer wavelengths (near 1000 nm) than the ferric absorption feature, increasing influence from the host rock substrates can explain the observed spectral shift. Moreover, spectral mixing between gossans and lichens was observed to trigger a spectral shift toward shorter wavelengths in the investigated ferric absorption feature near 900 nm, further complicating efforts to use this spectral feature for iron oxide mineral identification in areas of abundant lichens.

The findings discussed in this chapter indicate that to reliably identify different iron oxide minerals in areas of abundant lichens or optically thin gossans, observations on the ferric absorption feature wavelength position should be supplemented by other observations and techniques. Such techniques involve e.g. spectral endmember extraction and unmixing. These techniques were applied to a hyperspectral airborne dataset acquired from the Cape Smith Belt with the objective of delineating the gossan outcrops of the study area. Based on the spectral properties of these outcrops, two distinct gossan types were encountered: sedimentary gossans and mafic/ultramafic gossans. The latter gossan type is directly associated with the sulfide deposits of the Cape Smith Belt (Giovenazzo et al. 1989).

The results introduced in this chapter increase the current body of knowledge on the spectral characteristics of gossans and their usability for mineral exploration in northern areas. More specifically, the results suggest that gossans, and in some cases their underlying host rock mineralogy, can be detected by airborne hyperspectral remote sensing means in areas of abundant lichens on rock outcrops. This knowledge can be used to focus exploration efforts on the gossan outcrops most likely to be associated with economically viable sulfide deposits.

5.4. CONCLUSIONS

As pressures to improve cost-efficiency, and ethical, social and environmental standards increase in the mining industry, new techniques are needed to conduct mineral exploration. Hyperspectral remote sensing data and techniques offer a potentially powerful tool for mineral exploration in high latitude regions that are particularly vulnerable to environmental degradation and social disruption of indigenous cultures. This is possible if exploration efforts are focused on areas of the highest mineral potential, hence avoiding unnecessary intrusions to environmentally fragile areas. Hyperspectral remote sensing techniques are yet to be fully exploited by academia and industry, which may result from multiple factors, such as a lack of readily available data processing tools and an insufficient understanding on the possibilities and limitations of hyperspectral techniques. The three chapters of this thesis focus on developing such tools for the hyperspectral remote sensing detection of ore deposits in northern regions. The three main topics of the thesis, namely: i) the evaluation of the applicability of airborne hyperspectral remote sensing data for the detection of hydrothermal alteration zones and gossans in the presence of abundant lichens, ii) the applicability of hyperspectral remote sensing data for the detection of hydrothermal alteration intensity variability and iii) the optical thickness properties of gossans

and the influence of lichens and rock substrates on their spectral properties, address important information gaps in the scientific literature. The results of this work have contributed to advance the use of hyperspectral remote sensing for mineral exploration in general and in the Arctic in particular.

LITERATURE CITED

- Allen-Gil, S.M., Ford, J., Lasorsa, B.K., Monetti, M., Vlasova, T. and Landers, D.H., 2003. Heavy metal contamination in the Taimyr Peninsula, Siberian Arctic. *The Science of the Total Environment* 301: 119-138.
- Bechtel, R., Rivard, B. and Sánchez-Azofeifa, A., 2002. Spectral properties of foliose and crustose lichens based on laboratory experiments. *Remote Sensing of Environment* 82: 389–396.
- Cathelineau, M., 1988. Cation site occupancy in chlorites and illites as a function of temperature. *Clay Minerals* 23: 471-485.
- Chapin, F.S. III., 1983. Direct and indirect effects of temperature on Arctic plants. *Polar Biology* 2: 47-52.
- Clark, R. N., 1999. Chapter 1: Spectroscopy of rocks and minerals, and principles of spectroscopy. In: Rencz, A.N., ed.; *Manual of Remote Sensing, Volume 3, Remote Sensing for the Earth Sciences*, John Wiley and Sons, New York, USA: 3- 58.
- Cornell, R.M. and Schwertmann, U., 2003. *The iron oxides: Structure, properties, reactions, occurrences and uses*. Wiley-VCH GmbH & Co., Weiheim, Germany.
- Curry, J.A., Rossow, W.B., Randall, D. and Schramm, J.L., 1996. Overview of Arctic cloud and radiation characteristics. *Journal of Climate* 9: 1731-1764.
- Duke, E.F., 1994. Near infrared spectra of muscovite, Tschermak substitution, and metamorphic reaction progress: Implications for remote sensing. *Geology* 22: 621-624.
- German, C.R. and Von Damm, K.L., 2006. Hydrothermal Processes. In: Elderfield, H.: *The Oceans and Marine Geochemistry*. Elsevier, Oxford, UK: 181-222.

- Giovenazzo, D., Picard, C. and Guha, J., 1989. Tectonic setting of Ni-Cu-PGE deposits in the central part of the Cape Smith Belt. *Geoscience Canada* 16: 134–136.
- Herrmann, W., Blake, M., Doyle, M., Huston, D., Kamprad, J., Merry, N. and Pontual, S., 2001. Short wavelength infrared (SWIR) spectral analysis of hydrothermal alteration zones associated with base metal sulfide deposits at Rosebery and Western Tharsis, Tasmania, and Highway-Reward, Queensland. *Economic Geology* 96: 939-955.
- Hunt, G.R. and Salisbury, J.W., 1970. Visible and near-infrared spectra of minerals and rocks: I Silicate minerals. *Modern Geology* 1: 283-300.
- Ishikawa, Y., Sawaguchi, T., Iwaya, S.-i. and Horiuchi, M., 1976. Delineation of prospecting targets for Kuroko deposits based on modes of volcanism of underlying dacite and alteration haloes. *Mining Geology* 26: 105–117.
- Jenkins, H. and Yakovleva, N., 2006. Corporate social responsibility in the mining industry: Exploring trends in social and environmental disclosure. *Journal of Cleaner Production* 14: 271-284.
- Large, R.R., Gemmill, J.B., Paulick, H. and Huston, D.L., 2001. The alteration box plot: A simple approach to understanding the relationship between alteration mineralogy and lithochemistry associated with volcanic-hosted massive sulfide deposits. *Economic Geology* 96: 957–971.
- Rogge, D., Rivard, B., Segl, K., Grant, B. and Feng, J., 2014. Mapping of Ni-Cu-PGE ore hosting ultramafic rocks using airborne and simulated EnMap hyperspectral imagery, Nunavik, Canada. *Remote Sensing of Environment* 152: 302-317.
- Yang, K., Huntington, J.F., Gemmill, J.B. and Scott, K.M., 2011. Variations in composition and abundance of white mica in the hydrothermal alteration system at Hellyer, Tasmania, as

revealed by infrared reflectance spectroscopy. *Journal of Geochemical Exploration* 108:
143-156.

LITERATURE CITED (THESIS)

- Abdelsalam, M.G., Stern, R.J. and Berhane, W.G., 2000. Mapping gossans in arid regions with Landsat TM and SIR-C images: the Beddaho alteration zone in northern Eritrea. *Journal of African Earth Sciences* 30: 903–916.
- Abrams, M., Ashley, R., Rowan, L., Goetz, A. and Kahle, A., 1977. Mapping of hydrothermal alteration in the Cuprite mining district, Nevada, using aircraft scanner images for the spectral region 0.46 to 2.46 μm . *Geology* 5: 713–718.
- Adams, J. B., Smith, M. O. and Gillespie, A. R., 1993. Imaging spectroscopy: Interpretation based on spectral mixture analysis. In Pieters, C.M. and Englert, P.A., (eds.): *Remote geochemical analysis: Elemental and mineralogical composition*. Cambridge University Press, Cambridge, UK: 145–166.
- Ager, C.M. and Milton, N.M., 1987. Spectral reflectance of lichens and their effects on the reflectance of rock substrates. *Geophysics* 52: 898–906.
- Allen-Gil, S.M., Ford, J., Lasorsa, B.K., Monetti, M., Vlasova, T. and Landers, D.H., 2003. Heavy metal contamination in the Taimyr Peninsula, Siberian Arctic. *The Science of the Total Environment* 301: 119-138.
- Barrett, T.J. and MacLean, W.H., 1994. Chemostratigraphy and hydrothermal alteration in exploration for VHMS deposits in greenstones and younger volcanic rocks. In: Lentz, D.R. (ed): *Alteration and alteration processes associated with ore-forming Systems*. Geological Association of Canada, short course notes 11: 433–467.

- Barrett, T.J. and MacLean, W.H., 1994. Mass changes in hydrothermal alteration zones associated with VMS deposits of the Noranda area. *Exploration and Mining Geology* 3: 131–160.
- Bassett, W., 1960. Role of hydroxyl orientation in mica alteration. *Bulletin of the Geological Society of America* 71: 449–456.
- Bechtel, R., Rivard, B. and Sánchez-Azofeifa, A., 2002. Spectral properties of foliose and crustose lichens based on laboratory experiments. *Remote Sensing of Environment* 82: 389–396.
- Bedini, E., 2011. Mineral mapping in the Kap Simpson complex, central East Greenland, using HyMap and ASTER remote sensing data. *Advances in Space Research* 47: 60-73.
- Bellott, A., Corpel, J. and Millon, R., 1991. Contribution of magnetic modeling to the discovery of a hidden massive sulfide body at Hajar, Morocco. *Geophysics* 56: 983–991.
- Bettison-Varga, L. and MacKinnon, I.D.R., 1997. The role of randomly mixed-layered chlorite/smectite in the transformation of smectite to chlorite. *Clays and Clay Minerals* 45: 506–516.
- Biel, C., Subías, I., Fanlo, I., Mateo, E. and Acevedo, R.D., 2010. The Arroyo Rojo volcanic-hosted massive sulphide deposit (Tierra del Fuego, southernmost Argentina): geology, mineralogy, petrography and mineral chemistry. *Revista Mexicana de Ciencias Geológicas* 27: 84–96.
- Bierwirth, P., Huston, D. and Blewett, R., 2002. Hyperspectral mapping of mineral assemblages associated with gold mineralization in the Central Pilbara, Western Australia. *Economic Geology* 97: 819-826.

- Bischoff, J.L. and Seyfried, W.E., 1978. Hydrothermal chemistry of seawater from 25° to 350°C. *American Journal of Science* 278: 838–860.
- Boardman, J.W., 1993. Automating spectral unmixing of AVIRIS data using convex geometry concepts. Summaries of the fourth annual JPL (Jet Propulsion Laboratory) airborne geoscience workshop, JPL publication 93-26, AVIRIS Workshop, v. 1, Washington, USA: 11–14.
- Bostock, H.H., 1980. Geology of the Itchen Lake area, district of Mackenzie. Geological Survey of Canada, Memoir 391, Canadian Government Publishing Centre, Quebec, Canada.
- Bruegge, C.J., Stiegman, A.E., Rainen, R.A. and Springsteen, A.W., 1993. Use of Spectralon as a diffuse reflectance standard for in-flight calibration of earth-orbiting sensors. *Optical Engineering* 32: 805–814.
- Buckingham, W.F. and Sommer, S.E., 1983. Mineralogical characterization of rock surfaces formed by hydrothermal alteration and weathering - application to remote sensing. *Economic Geology* 78: 664–674.
- Burns, R.G., 1993. Mineralogical applications of crystal field theory. 2nd edition. Cambridge University Press, Cambridge, UK.
- Çağatay, N.M., 1993. Hydrothermal alteration associated with volcanogenic massive sulfide deposits: Examples from Turkey. *Economic Geology* 88: 606–621.
- Cathelineau, M., 1988. Cation site occupancy in chlorites and illites as a function of temperature. *Clay Minerals* 23: 471–485.
- Chapin, F.S. III., 1983. Direct and indirect effects of temperature on Arctic plants. *Polar Biology* 2: 47-52.

- Clark, R. N., 1999. Chapter 1: Spectroscopy of rocks and minerals, and principles of spectroscopy. In: Rencz, A.N., ed.; *Manual of Remote Sensing, Volume 3, Remote Sensing for the Earth Sciences*, John Wiley and Sons, New York, USA: 3- 58.
- Clark, R.N. and Roush, T.L., 1984. Reflectance spectroscopy: quantitative analysis techniques for remote sensing applications. *Journal of Geophysical Research* 89: 6329–6340.
- Clark, R.N., Swayze, G.A., Livo, K.E., Kokaly, R.F., King, T.V.V., Dalton, J.B., Vance, J.S., Rockwell, B.W., Hoefen, T. and McDougal, R.R., 2002. Surface reflectance calibration of terrestrial imaging spectroscopy data. A tutorial using AVIRIS. *Proceedings of the 10th Airborne Earth Science Workshop*, JPL Publication 02-1.
- Clark, R.N., Swayze, G.A., Wise, R., Livo, E., Hoefen, T., Kokaly, R. and Sutley, S.J., 2007. USGS digital spectral library splib06a: U.S. Geological Survey, Digital Data Series 231 (<http://speclab.cr.usgs.gov/spectral.lib06>).
- Conradsen, K. and Harpøth, O., 1984. Use of Landsat multispectral scanner data for detection and reconnaissance mapping of iron oxide staining in mineral exploration. Central East Greenland. *Economic Geology* 79: 1229–1244.
- Cornell, R.M. and Schwertmann, U., 2003. *The iron oxides: Structure, properties, reactions, occurrences and uses*. Wiley-VCH GmbH & Co., Weiheim, Germany.
- Costa, U.R., Barnett, R.L. and Kerrich, R., 1983. The Mattagami Lake Mine Archean Zn-Cu sulfide deposit, Quebec: Hydrothermal coprecipitation of talc and sulfides in a sea-floor brine pool-evidence from geochemistry, $^{18}\text{O}/^{16}\text{O}$, and mineral chemistry. *Economic Geology* 78: 1144–1203.
- Cressman, G.P., 1959. An operational objective analysis system. *Monthly Weather Review* 87: 367-374.

- Curry, J.A., Rossow, W.B., Randall, D. and Schramm, J.L., 1996. Overview of Arctic cloud and radiation characteristics. *Journal of Climate* 9: 1731-1764.
- Date, J., Watanabe, Y. and Saeki, Y., 1983. Zonal alteration around the Fukazawa Kuroko deposits, Akita prefecture, northern Japan. *Economic Geology Monograph* 5: 365–386.
- Dillon-Leitch, H.C.H., Watkinson, D.H. and Coats, C.J.A., 1986. Distribution of Platinum-Group Elements in the Donaldson West Deposit, Cape Smith Belt, Quebec. *Economic Geology* 81: 1147-1158.
- Duke, E.F., 1994. Near infrared spectra of muscovite, Tschermak substitution, and metamorphic reaction progress: Implications for remote sensing. *Geology* 22: 621–624.
- Eberl, D.D., Środoń, J., Lee, M., Nadeau, P.H. and Northrop, H.R., 1987. Sericite from the Silverton caldera, Colorado: Correlation among structure, composition, origin, and particle thickness. *American Mineralogist* 72: 914-934.
- ESRI, 2011. ArcGIS Desktop. Release 10. Redlands, CA: Environmental Systems Research Institute.
- Franklin, J.M., 1986. Volcanic-associated massive sulphide deposits – an update. In: Andrew, C.J., Crowe, R.W.A., Finlay, S., Pennell, W.M. and Pyne, J.F.: *Geology and genesis of mineral deposits in Ireland*. Irish Association for Economic Geology, Dublin, UK: 49–69.
- Franklin, J.M., 1997. Lithochemical and mineralogical methods for base metal and gold exploration. In: Gubins, A.G. (ed.): *Proceedings of Exploration 97: Fourth Decennial International Conference on Mineral Exploration*, Toronto, Canada: 191–208.
- Franklin, J.M., Kasarda, J. and Poulsen, K.H., 1975. Petrology and chemistry of the alteration zone of the Mattabi massive sulfide deposit, *Economic Geology* 70: 63–79.

- Galley, A.G., 1993. Characteristics of semi-conformable alteration zones associated with volcanogenic massive sulphide districts. *Journal of Geochemical Exploration* 48: 175–200.
- Galley, A.G., Hannington, M.D. and Jonasson, I.R., 2007. Volcanogenic massive sulphide deposits. In: Goodfellow, W.D. (ed.): *Mineral deposits of Canada: A synthesis of major deposit-types, district metallogeny, the evolution of geological provinces, and exploration methods*. Special Publication No. 5, Geological Association of Canada, Ottawa, Canada: 141-161.
- Gemmell, J.B. and Large, R.R., 1992. Stringer system and alteration zones underlying the Hellyer volcanic-hosted massive sulfide deposit, Tasmania, Australia. *Economic Geology* 87: 620–649.
- German, C.R. and Von Damm, K.L., 2006. Hydrothermal Processes. In: Elderfield, H.: *The Oceans and Marine Geochemistry*. Elsevier, Oxford, UK: 181-222.
- Giovenazzo, D., Picard, C. and Guha, J., 1989. Tectonic setting of Ni-Cu-PGE deposits in the central part of the Cape Smith Belt. *Geoscience Canada* 16: 134–136.
- Gitelson, A. and Merzlyak, M.N., 1994. Spectral reflectance changes associated with autumn senescence of *Aesculus hippocastanum* L. and *Acer platanoides* L. leaves. Spectral features and relation to chlorophyll estimation. *Journal of Plant Physiology* 143: 286–292.
- Goetz, A.F.H., Curtiss, B. and Shiley, D.A., 2009. Rapid gangue mineral concentration measurement over conveyors by NIR reflectance spectroscopy. *Minerals Engineering* 22: 490-499.
- Goetz, A.F.H. and Rowan, L.C., 1981. Geologic remote sensing. *Science* 211: 781–791.
- Goodfellow, W.D. and Peter, J.M., 1994. Geochemistry of hydrothermally altered sediment, Middle Valley, northern Juan de Fuca Ridge. Mottl, M.J., Davis, E.E., Fisher, A.T. and

Slack, J.F (eds.): Proceedings of the Ocean Drilling Program, Scientific Results 139: 207–289.

Government of Canada, 2014. Calculation of the 1971 to 2000 climate normals for Canada. Available at: http://climate.weather.gc.ca/climate_normals/.

Granier, C., Niemeier, U., Jungclaus, J.H., Emmons, L., Hess, P., Lamarque, J.-F., Walters, S. and Brasseur, G.P., 2006. Ozone pollution from future ship traffic in the Arctic northern passages. *Geophysical Research Letters* 33: L13807, doi:10.1029/2006GL026180.

Guidotti, C.V. and Sassi, F.P., 1998. Petrogenetic significance of Na-K white mica mineralogy: Recent advances for metamorphic rocks. *European Journal of Mineralogy* 10: 815–854.

Hannington, M.D., Kjarsgaard, I.M., Galley, A.G. and Taylor, B., 2003. Mineral-chemical studies of metamorphosed hydrothermal alteration in the Kristineberg volcanogenic massive sulfide district, Sweden. *Mineralium Deposita* 38: 423–442.

Harding, D.J., Wirth, K.R. and Bird, J.M., 1989. Spectral mapping of Alaskan ophiolites using Landsat thematic mapper data. *Remote Sensing of Environment* 28: 219-232.

Harris, J.R., Ponomarev, P., Shang, J. and Rogge, D., 2006. Noise reduction and best band selection techniques for improving classification results using hyperspectral data: application to lithological mapping in Canada's Arctic. *Canadian Journal of Remote Sensing* 32: 341-354.

Harris, J.R., Rogge, D., Hitchcock, R., Ijewliw, O. and Wright, D., 2005. Mapping lithology in Canada's Arctic: application of hyperspectral data using the minimum noise fraction transformation and matched filtering. *Canadian Journal of Earth Sciences* 42: 2173-2193.

Herrmann, W., Blake, M., Doyle, M., Huston, D., Kamprad, J., Merry, N. and Pontual, S., 2001. Short wavelength infrared (SWIR) spectral analysis of hydrothermal alteration zones

- associated with base metal sulfide deposits at Rosebery and Western Tharsis, Tasmania, and Highway-Reward, Queensland. *Economic Geology* 96: 939–955.
- Herrmann, W., Green, G.R., Barton, M.D. and Davidson, G.J., 2009. Lithogeochemical and stable isotopic insights into submarine genesis of pyrophyllite-altered facies at the Boco Prospect, Western Tasmania. *Economic Geology* 104: 775–792.
- Hitchcock, R. and White, H.P., 2007. Processing EO-1 Hyperion data using ISDAS, Geomatics, Canada, Technical Note 2.
- Hulen, J.B. and Nielson, D.L., 1986. Hydrothermal alteration in the Baca geothermal system, Redondo Dome, Valles Caldera, New Mexico. *Journal of Geophysical Research* 91: 1867–1886.
- Hunt, G.R., 1977. Spectral signatures of particulate minerals in the visible and near infrared. *Geophysics* 42: 501-513.
- Hunt, G.R., 1979. Near-infrared (1.3-2.4 μm) spectra of alteration minerals—Potential for use in remote sensing. *Geophysics* 44: 1974–1986.
- Hunt, G.R. and Ashley, R.P., 1979. Spectra of altered rocks in the visible and near infrared. *Economic Geology* 74: 1613–1629.
- Hunt, G.R. and Salisbury, J.W., 1970. Visible and near-infrared spectra of minerals and rocks: I Silicate minerals. *Modern Geology* 1: 283–300.
- Hunt, G.R. and Salisbury, J.W., 1976. Visible and near infrared spectra of minerals and rocks: XI. Sedimentary rocks. *Modern Geology* 5: 211–217.
- Hunt, G.R., Salisbury, J.W. and Lenhoff, C.J., 1971. Visible and near infrared spectra of minerals and rocks: III. Oxides and hydroxides. *Modern Geology* 2: 195–205.

- Hunt, G.R., Salisbury, J.W. and Lenhoff, C.J. 1974. Visible and near infrared spectra of minerals and rocks: IX. Basic and ultrabasic igneous rocks. *Modern Geology* 5: 15–22.
- Hynes, A. and Francis, D., 1982. A transect of the Early Proterozoic Cape Smith foldbelt, New Quebec. *Tectonophysics* 88: 23–59.
- Intrieri, J.M., Shupe, M.D., Uttal, T. and B.J. McCarty. 2002. An annual cycle of Arctic cloud characteristics observed by radar and lidar at SHEBA. *Journal of Geophysical Research* 107: SHE 5-1 – SHE 5-15.
- Inui, M. and Toriumi, M., 2004. A theoretical study on the formation of growth zoning in garnet consuming chlorite. *Journal of Petrology* 45: 1369–1392.
- Ishikawa, Y., Sawaguchi, T., Iwaya, S.-i. and Horiuchi, M., 1976. Delineation of prospecting targets for Kuroko deposits based on modes of volcanism of underlying dacite and alteration haloes. *Mining Geology* 26: 105–117.
- Jenkins, H. and Yakovleva, N., 2006. Corporate social responsibility in the mining industry: Exploring trends in social and environmental disclosure. *Journal of Cleaner Production* 14: 271-284.
- Jones, S., Herrmann, W. and Gemmill, J.B., 2005. Short wavelength infrared spectral characteristics of the HW horizon: Implications for exploration in the Myra Falls volcanic-hosted massive sulfide camp, Vancouver Island, British Columbia, Canada. *Economic Geology* 100: 273–294.
- Kokaly, R.F., Asner, G.P., Ollinger, S.V., Martin, M.E. and Wessman, C.A., 2009. Characterizing canopy biochemistry from imaging spectroscopy and its application to ecosystem studies. *Remote Sensing of Environment* 113: S78-S91.

- Kranidiotis, P. and MacLean, W.H., 1987. Systematics of chlorite alteration at the Phelps Dodge massive sulfide deposit, Matagami, Quebec. *Economic Geology* 82: 1898–1911.
- Krauskopf, K. 1967. *Introduction to geochemistry*. McGraw-Hill Book Company, New York, USA.
- Kruse, F. and Lefkoff, A., 1999. Analysis of spectral data of manmade materials, military targets, and background using an expert system based approach. *Proceedings of ISSSR (International Society for Strategic Studies in Radiology)*, Las Vegas, USA: 339–350.
- Kruse, F., Lefkoff, A., Boardman, J., Heidebrecht, K., Shapiro, A., Barloon, P. and Goetz, A., 1993. The Spectral Image Processing System (SIPS) - interactive visualization and analysis of imaging spectrometer data. *Remote Sensing of Environment* 44: 145–163.
- Laidler, G.J., Treitz, P.M. and Atkinson, D.M., 2008. Remote sensing of Arctic vegetation: Relations between the NDVI, spatial resolution and vegetation cover on Boothia Peninsula, Nunavut. *Arctic* 61: 1–13.
- Large, R.R. 1977. Chemical evolution and zonation of massive sulfide deposits in volcanic terrains. *Economic Geology* 72: 549–572.
- Large, R.R., Gemmell, J.B., Paulick, H. and Huston, D.L., 2001. The alteration box plot: A simple approach to understanding the relationship between alteration mineralogy and litho-geochemistry associated with volcanic-hosted massive sulfide deposits. *Economic Geology* 96: 957–971.
- Larson, P.B. 1984. Geochemistry of the alteration pipe at the Bruce Cu-Zn volcanogenic massive sulfide deposit, Arizona. *Economic Geology* 79: 1880–1896.

- Leistel, J.M., Marcoux, E., Thiéblemont, D., Quesada, C., Sánchez, A., Almodóvar, G.R., Pascual, E. and Sáez, R., 1998. The volcanic-hosted massive sulphide deposits of the Iberian Pyrite Belt. *Mineralium Deposita* 33: 2–30.
- Lentz, D.R. and Goodfellow, W.D., 1993. Petrology and mass-balance constraints on the origin of quartz-augen schist associated with the Brunswick massive sulfide deposits, Bathurst, New Brunswick. *The Canadian Mineralogist* 31: 877-903.
- Leshner, C., 2007. Ni-Cu-PGE deposits in the Raglan area, Cape Smith Belt, New Quebec. In: Goodfellow, W.D. (ed.): *Mineral Deposits of Canada. A synthesis of major deposit types, district metallogeny, the evolution of geological provinces and exploration methods*. Special Publication no. 5, Geological Association of Canada, Ottawa, Canada: 351–386.
- Leverington, D.W., 2010. Discrimination of sedimentary lithologies using Hyperion and Landsat Thematic Mapper data: a case study at Melville Island, Canadian High Arctic. *International Journal of Remote Sensing* 31: 233-260.
- Leverington, D.W. and Moon, W.M., 2012. Landsat-TM-based discrimination of lithological units associated with the Purtuniqu ophiolite, Quebec, Canada. *Remote Sensing* 4: 1208-1231.
- Li, G., Peacor, D.R., Merriman, R.J. and Roberts, B., 1994. The diagenetic to low-grade metamorphic evolution of matrix white micas in the system muscovite-paragonite in a mudrock from Central Wales. *Clays and Clay Minerals* 42: 369-381.
- Longton, R., 1988. *Biology of polar bryophytes and lichens*. Cambridge University Press, Cambridge, UK.

- Lydon, J.W., 2007. An overview of the economic and geological contexts of Canada's major mineral deposit types. In: Goodfellow, W.D. (ed.): Mineral Deposits of Canada. A synthesis of major deposit-types, district metallogeny, the evolution of geological provinces, and exploration methods. Special Publication No. 5, Geological Association of Canada, Ottawa, Canada: 3–48.
- Machado, N., David, J., Scott, D., Lamothe, D., Philippe, S. and Gariépy, C., 1993. U-Pb geochronology of the western Cape Smith Belt, Canada: new insights on the age of initial rifting and arc magmatism. *Precambrian Research* 63: 211–223.
- MacLean, W. and Hoy, L.D., 1991. Geochemistry of hydrothermally altered rocks at the Horne Mine, Noranda, Quebec. *Economic Geology* 86: 506–528.
- Mager, D., 2009. Climate change, conflicts and cooperation in the Arctic: Easier access to hydrocarbons and mineral resources? *The International Journal of Marine and Coastal Law* 24: 347–354.
- Maria Dreher, A., Perez Xavier, R. and Luiz Martini, S., 2005. Fragmental rocks of the Igarapé Bahia Cu-Au deposit, Carajás mineral province. Brazil, *Revista Brasileira de Geociências* 35: 359–368.
- McLeod, R.L., Gabell, A.R., Green, A.A. and Gardavsky, V., 1987. Chlorite infrared spectral data as proximity indicators of volcanogenic massive sulphide mineralisation. *Pacific Rim Congress (The Geology, Structure, Mineralisation and Economy of the Pacific Rim)*, Gold Coast, Australia: 321–324.
- Miyashiro, A. and Shido, F., 1985. Tschermak substitution in low- and middle-grade pelitic schists. *Journal of Petrology* 26: 449–487.

- MMG, 2011. Izok Lake. A summary of exploration activity on the Izok Lake project 2007-2011, Annual report Nunavut Impact Review Board, Vancouver, Canada. Available at: [ftp://ftp.nirb.ca/01-screenings/completed_screenings/2006/06EN066-MMG\(Wolfden\)-Izok and Hood Project/05-annual report/120201-06EN066-MMG 2011 Annual Report-IA1E.pdf](ftp://ftp.nirb.ca/01-screenings/completed_screenings/2006/06EN066-MMG(Wolfden)-Izok_and_Hood_Project/05-annual_report/120201-06EN066-MMG_2011_Annual_Report-IA1E.pdf).
- Modeland, S., Francis, D. and Hynes, A., 2003. Enriched mantle components in Proterozoic continental-flood basalts of the Cape Smith foldbelt, northern Québec. *Lithos* 71: 1–17.
- Money, P.L and Heslop, J.B., 1976. Geology of the Izok Lake massive sulphide deposit. *Canadian Mining Journal* 97: 24–27.
- Morrison, I.R., 2004. Geology of the Izok massive sulfide deposit, Nunavut Territory, Canada. *Exploration and Mining Geology* 13: 25–36.
- Morrison, I.R. and Balint, F., 1993. Geology of the Izok massive sulphide deposits, Northwest Territories, Canada. *Proceedings of the International Symposium on Zinc, Hobart, Australia*: 161-170.
- Mortensen, J.K., Thorpe, R.I., Padgham, W.A., King, J.E.s and Davis, W.J., 1988. U-Pb zircon ages for felsic volcanism in Slave Province, N.W.T.. In: *Radiogenic Age and Isotopic Studies: Report 2, Geological Survey of Canada* 88-2: 85–95.
- Mustard, J.F., 1994. Lithologic mapping of gabbro and peridotite sills in the Cape Smith fold and thrust belt with thematic mapper and airborne radar data. *Canadian Journal of Remote Sensing* 20: 222-232.
- Nesbitt, B.E., 1982. Metamorphic sulfide-silicate equilibria in the massive sulfide deposits at Ducktown, Tennessee. *Economic Geology* 77: 364–378.
- Nielsen, H.H., 1951. The vibration-rotation energies of molecules. *Reviews of Modern Physics* 23: 90–136.

- Ohmoto, H., 1996. Formation of volcanogenic massive sulfide deposits: The Kuroko perspective. *Ore Geology Reviews* 10: 135–177.
- Oliver, M.A. and Webster, R., 1990. Kriging: a method of interpolation for geographical information systems. *International Journal of Geographical Information Systems* 4: 313–332.
- Parrish, R.R., 1989. U-Pb geochronology of the Cape Smith Belt and Sugluk block, northern Quebec. *Geoscience Canada* 16: 126–130.
- Paulick, H., Herrmann, W. and Gemmill, J.B., 2001. Alteration of felsic volcanics hosting the Thalanga massive sulfide deposit (Northern Queensland, Australia) and geochemical proximity indicators to ore. *Economic Geology* 96: 1175–1200.
- Payette, S., Morneau, C., Sirois, L. and Despons, M., 1989. Recent fire history of the northern Québec biomes. *Ecology* 70: 656–673.
- Petzold, D.E. and Goward, S.N., 1988. Reflectance spectra of subarctic lichens. *Remote Sensing of Environment* 24: 481-492.
- Philip, G.M. and Watson, D.F., 1982. A precise method for determining contoured surfaces. *Australian Petroleum Exploration Association Journal* 22: 205-212.
- Pirajno, F., 2009. Hydrothermal processes and wall rock alteration. In: *Hydrothermal Processes and Mineral Systems*, Springer Netherlands: 73-164.
- Plimer, I.R. and de Carvalho, D., 1982. The geochemistry of hydrothermal alteration at the Salgadoinho Copper Deposit, Portugal, *Mineralium Deposita* 17: 193–211.
- Post, J.L. and Noble, P.N., 1993. The near-infrared combination band frequencies of dioctahedral smectites, micas, and illites. *Clays and Clay Minerals* 41: 639–644.

- Purvis, W., 2000. Lichens (Smithsonian's Natural World Series). Smithsonian Institution Press, Washington, USA.
- Purvis, O.W. and Halls, C., 1996. A review of lichens in metal-enriched environments. *Lichenologist* 28: 571-601.
- Rasmussen, B., 2000. Filamentous microfossils in a 3,235-million-year-old volcanogenic massive sulphide deposit. *Nature* 405, 676-679.
- Richter, R. and Schläpfer, D., 2002. Geo-atmospheric processing of airborne imaging spectrometry data. Part 2: Atmospheric/topographic correction. *International Journal of Remote Sensing* 23: 2631-2649.
- Rieder, M., Cavazzini, G., D'Yakonov, Y.S., Frank-Kamenetskii, V.A., Gottardi, G., Guggenheim, S., Koval, P.V., Müller, G., Neiva, A.M.R., Radoslovich, E.W., Robert, J.-L., Sassi, F.P., Takeda, H., Weiss, Z. and Wones, D.R., 1998. Nomenclature of the micas. *The Canadian Mineralogist* 36: 41-48.
- Rivard, B. and Arvidson, R.E., 1992. Utility of imaging spectrometry for lithologic mapping in Greenland. *Photogrammetric Engineering & Remote Sensing* 58: 945-949.
- Rivard, B., Rogge, D., Jeng, J., Grant, B. and Pardy, J., 2010. Hyperspectral sensing in support of mineral exploration in the Arctic: Example from the Cape Smith nickel belt, Canada. *Proceedings of the 'Hyperspectral 2010 Workshop', Frascati, Italy.*
- Rogge, D.M. and Rivard, B., 2010. Iterative spatial filtering for reducing intra-class spectral variability and noise. *2nd Workshop on Hyperspectral Image and Signal Processing: Evolution in Remote Sensing (WHISPERS), Reykjavik, Iceland: 1-4.*

- Rogge, D., Rivard, B., Segl, K., Grant, B. and Feng, J., 2014. Mapping of Ni-Cu-PGE ore hosting ultramafic rocks using airborne and simulated EnMap hyperspectral imagery, Nunavik, Canada. *Remote Sensing of Environment* 152: 302-317.
- Rogge, D.M., Rivard, B., Zhang, J. and Feng, J., 2006. Iterative spectral unmixing for optimizing per-pixel endmember sets. *IEEE Transactions on Geoscience and Remote Sensing*, 44: 3725-3736.
- Rogge, D.M., Rivard, B., Zhang, J., Sanchez, A., Harris, J. and Feng, J., 2007. Integration of spatial-spectral information for the improved extraction of endmembers. *Remote Sensing of Environment* 110: 287–303.
- Rowan, L.C., Goetz, A.F.H. and Ashley, R.P., 1977. Discrimination of hydrothermally altered and unaltered rocks in visible and near infrared multispectral images. *Geophysics* 42: 522– 535.
- Sánchez-España, J., Velasco, F. and Yusta, I., 2000. Hydrothermal alteration of felsic volcanic rocks associated with massive sulphide deposition in the northern Iberian Pyrite Belt (SW Spain). *Applied Geochemistry* 15: 1265–1290.
- Sancho, L.G., de la Torre, R., Horneck, G., Ascaso, C., de los Rios, A., Pintado, A., Wierzchos, J. and Schuster, M., 2007. Lichens survive in space: Results from the 2005 LICHENS Experiment. *Astrobiology* 7: 443-454.
- Schade, J., Cornell, D.H. and Theart, H.F.J., 1989. Rare earth element and isotopic evidence for the genesis of the Prieska massive sulfide deposit, South Africa. *Economic Geology* 84: 49–63.

- Scheinost, A.C., Chavernas, A., Barrón, V. and Torrent, J., 1998. Use and limitations of second-derivative diffuse reflectance spectroscopy in the visible to near-infrared range to identify and quantify Fe oxide minerals in soils. *Clays and Clay Minerals* 46: 528–536.
- Schetselaar, E. and de Kemp, E., 2000. Image classification from Landsat TM, airborne magnetics and DEM data for mapping Paleoproterozoic bedrock units, Baffin Island, Nunavut, Canada. *International Archives of Photogrammetry and Remote Sensing*, Vol. XXXIII, Part B7: 1325-1332.
- Schetselaar, E.M., Ryan, J.J., 2009. Remote predictive mapping of the Boothia mainland area, Nunavut, Canada: an iterative approach using Landsat ETM, aeromagnetic, and geological field data. *Canadian Journal of Remote Sensing* 35: S72-S94.
- Schmidt, J.M., 1988. Mineral and whole-rock compositions of seawater-dominated hydrothermal alteration at the Arctic volcanogenic massive sulfide prospect, Alaska. *Economic Geology* 83: 822–842.
- Scott, D.J., Helmstaedt, H. and Bickle, M.J., 1992. Purtunig ophiolite, Cape Smith belt, northern Quebec, Canada: A reconstructed section of Early Proterozoic oceanic crust. *Geology* 20: 173–176.
- Scott, K.M. and Yang, K., 1997. Spectral reflectance studies of white micas: Exploration and mining report 439R. CSIRO Division of Exploration and Mining, Australia.
- Settle, J.J. and Drake, N.A., 1993. Linear mixing and the estimation of ground cover proportions. *International Journal of Remote Sensing* 14: 1159-1177.
- Seyfried, W.E., Jr., Berndt, M.E. and Seewald, J.S., 1988. Hydrothermal alteration processes at mid-ocean ridges: Constraints from diabase alteration experiments, hot spring fluids and composition of the oceanic crust. *Canadian Mineralogist* 26: 787–804.

- Seyfried, W.E., Jr. and Mottl, M.J., 1982. Hydrothermal alteration of basalt by seawater under seawater dominated conditions. *Geochimica et Cosmochimica Acta* 46: 985–1002.
- Shepard, D., 1968. A two-dimensional interpolation function for irregularly-spaced data. *Proceedings of the 1968 ACM (Association for Computing Machinery) National Conference*, New York, USA: 517–524.
- Shupe, M.D. and Intrieri, J.M., 2004. Cloud radiative forcing of the Arctic surface: The influence of cloud properties, surface albedo, and solar zenith angle. *Journal of Climate* 17: 616-628.
- Sims, D.A. and Gamon, J.A., 2002. Relationships between leaf pigment content and spectral reflectance across a wide range of species, leaf structures and developmental stages. *Remote Sensing of Environment* 81: 337–354.
- Singer, R.B., 1981. Near-infrared spectral reflectance of mineral mixtures: systematic combinations of pyroxenes, olivine, and iron oxides. *Journal of Geophysical Research* 86: 7967– 7982.
- Staeenz, K., Nadeau, C., Secker, J. and Budkewitsch, P., 2000. Spectral unmixing applied to vegetated environments in the Canadian Arctic for mineral mapping. *Proceedings of the International Archives of Photogrammetry and Remote Sensing*, Vol. XXXIII, Part B7: 1464-1471.
- Stephens, M.B., Swinden, H.S. and Slack, J.F., 1984. Correlation of massive sulfide deposits in the Appalachian-Caledonian Orogen on the basis of Paleotectonic setting. *Economic Geology* 79: 1442–1478.
- St-Onge, M.R. and Lucas, S.B., 1993. *Geology of the eastern Cape Smith Belt: Parts of the Kangiqsujuaq, Cratère du Nouveau-Québec, and Lacs Nuvilik map areas, Quebec*. Geological Survey of Canada Memoir 438, Ottawa, Canada.

- St-Onge, M.R., Lucas, S.B. and Parrish, R.R., 1992. Terrane accretion in the internal zone of the Ungava orogen, northern Quebec. Part 1: Tectonostratigraphic assemblages and their tectonic implications. *Canadian Journal of Earth Sciences* 29: 746–764.
- St-Onge, M.R., Scott, D.J. and Lucas, S.B., 2000. Early partitioning of Quebec: Microcontinent formation in the Paleoproterozoic. *Geology* 28: 323–326.
- Stow, D.A., Hope, A., McGuire, D., Verbyla, D., Gamon, J., Huemrich, F., Houston, S., Racine, C., Sturm, M., Tape, K., Hinzman, L., Yoshikawa, K., Tweedie, C., Noyle, B., Silapaswan, C., Douglas, D., Griffith, B., Jia, G., Epstein, H., Walker, D., Daeschner, S., Petersen, A., Zhou, L. and Myneni, R., 2004. Remote sensing of vegetation and land-cover change in Arctic Tundra Ecosystems. *Remote Sensing of Environment* 89: 281–308.
- Swayze, G.A., Clark, R.N., Goetz, A.F.H., Chrien, T.G. and Gorelick, N.S., 2003. Effects of spectrometer band pass, sampling, and signal-to-noise ratio on spectral identification using the Tetracorder algorithm. *Journal of Geophysical Research* 108, doi: 10.1029/2002JE001975.
- Taylor, G.F., 1987. Near-infrared spectra of West Shasta gossans compared with true and false gossans from Australia and Saudi Arabia and trace element content of gossans at four mines in the West Shasta massive sulfide district - A discussion. *Economic Geology* 82: 230-234.
- Tivey, M.K., 2007. Generation of seafloor hydrothermal vent fluids and associated mineral deposits. *Oceanography* 20: 50-65.
- Urabe, T., Scott, S.D. and Hattori, K., 1983. A comparison of footwall-rock alteration and geothermal systems beneath some Japanese and Canadian volcanogenic massive sulfide deposits. *Economic Geology Monograph* 5: 345–364.

- Van der Meer, F., van Ruitenbeek, F., van der Werff, H. and Hecker, C., 2010. Mapping P-T conditions in hydrothermal systems using hyperspectral remote sensing and object based techniques. 2nd Workshop on Hyperspectral Image and Signal Processing: Evolution in Remote Sensing (WHISPERS), Reykjavik, Iceland: 1-4.
- Van der Meer, F.D., van der Werff, H.M.A., van Ruitenbeek, F.J.A., Hecker, C.A., Bakker, W.H., van der Meijde, M., Carranza, E.J.M., de Smeth, J.B. and Woldai, T., 2012. Multi- and hyperspectral geologic remote sensing: A review. *International Journal of Applied Earth Observation and Geoinformation* 14: 112–128.
- Van Ruitenbeek, F.J.A., Cudahy, T., Hale, M. and van der Meer, F.D., 2005. Tracing fluid pathways in fossil hydrothermal systems with near-infrared spectroscopy. *Geology* 33: 597–600.
- Van Ruitenbeek, F.J.A., Cudahy, T.J., van der Meer, F.D. and Hale, M., 2012. Characterization of the hydrothermal systems associated with Archean VMS-mineralization at Panorama, Western Australia, using hyperspectral, geochemical and geothermometric data. *Ore Geology Reviews* 45: 33–46.
- Van Ruitenbeek, F.J.A., Debba, P., van der Meer, F. D., Cudahy, T., van der Meijde, M. and Hale, M., 2006. Mapping white micas and their absorption wavelengths using hyperspectral band ratios. *Remote Sensing of Environment* 102: 211–222.
- Velde, B., 1965. Phengite micas: Synthesis, stability, and natural occurrence. *American Journal of Science* 263: 886–913.
- Velde, B., 1967. Si⁺⁴ content of natural phengites. *Contributions to mineralogy and petrology* 14: 250–258.

- Volesky, J.C., Stern, R.J. and Johnson, P.R., 2003. Geological control of massive sulfide mineralization in the Neoproterozoic Wadi Bidah shear zone, southwestern Saudi Arabia, inferences from orbital remote sensing and field studies. *Precambrian Research* 123: 235–247.
- West, L., McGown, D.J., Onstott, T.C., Morris, R.V., Suchecki, P. and Pratt, L.M., 2009. High Lake gossan deposit: An Arctic analogue for ancient Martian surficial processes? *Planetary and Space Science* 57: 1302–1311.
- Winton, M., 2006. Amplified Arctic climate change: What does surface albedo feedback have to do with it? *Geophysical Research Letters* 33: L03701, doi:10.1029/2005GL025244.
- Yang, K. and Huntington, J.F., 1996. Spectral signatures of hydrothermal alteration in the metasediments at Dead Bullock Soak, Tatami desert, Northern Territory: Exploration and mining report 270R. CSIRO Division of Exploration and Mining, New South Wales, Australia.
- Yang, K., Huntington, J.F., Gemmell, J.B. and Scott, K.M., 2011. Variations in composition and abundance of white mica in the hydrothermal alteration system at Hellyer, Tasmania, as revealed by infrared reflectance spectroscopy: *Journal of Geochemical Exploration* 108: 143–156.

APPENDIX A: The Ishikawa Index (AI) values (%) in the Izok Lake study area

Easting	Northing	AI (%)	Easting	Northing	AI (%)
416465	7279647	85	417984	7279586	44
416500	7279676	93	418011	7279684	52
416520	7279641	74	417836	7279873	91
416669	7279615	97	417746	7279993	62
416710	7279579	92	417717	7279653	73
417121	7279459	84	417783	7279670	24
417334	7279543	96	418335	7279062	87
417586	7279719	97	418348	7279099	73
417963	7279994	74	418366	7279099	87
418202	7279193	94	418177	7279306	95
418208	7278052	97	418173	7279303	94
414917	7281784	72	418201	7279198	96
416232	7281024	97	418596	7279114	64
416116	7281082	56	416995	7281465	32
418613	7278523	82	416909	7281194	81
415883	7282940	47	416952	7281226	94
416250	7283636	38	417003	7281244	81
414793	7285719	46	417061	7281292	95
415129	7285333	37	417152	7281330	93
415543	7285322	43	417315	7281412	26
416006	7285663	32	416953	7281354	86
416196	7285920	55	417011	7281128	43
418066	7279490	70	417068	7281160	83
418159	7279540	83	417227	7281291	89
418180	7279582	89	417029	7281641	23

APPENDIX A: The Ishikawa Index (AI) values (%) in the Izok Lake study area

Easting	Northing	AI (%)	Easting	Northing	AI (%)
416963	7281612	38	418372	7279168	64
416802	7281615	97	416400	7282194	86
416845	7281646	60	418206	7279531	89
416918	7281692	75	418132	7279505	50
416650	7281742	93	418071	7279471	84
416570	7281707	97	418066	7279337	83
416537	7281672	97	418141	7279381	70
416482	7281649	71	418236	7279465	91
416611	7281610	98	418383	7279520	95
416675	7281648	93	418174	7279301	94
416741	7281673	94	418270	7279332	62
416798	7281703	77	418335	7279374	94
416838	7281733	77	418374	7279411	97
416573	7281819	85	418415	7279442	94
416501	7281773	54	418451	7279453	98
416471	7281741	73	418486	7279368	98
417512	7281126	87	418446	7279336	84
417644	7280989	44	418193	7279178	79
417351	7281214	91	418133	7279148	75
417383	7281174	93	418288	7279122	96
417402	7281130	93	418441	7279226	92
417424	7281085	94	418538	7279270	94
417467	7281004	69	418564	7279291	65
417211	7281230	86	418563	7279166	87
417256	7281172	94	418506	7279135	86

APPENDIX A: The Ishikawa Index (AI) values (%) in the Izok Lake study area

Easting	Northing	AI (%)	Easting	Northing	AI (%)
418333	7279030	55	417821	7278677	90
418604	7279090	69	417895	7278552	82
418597	7278889	76	417923	7278493	60
418235	7278730	57	418001	7278370	97
418190	7278701	68	417677	7278526	78
418262	7278646	74	417627	7278594	83
418298	7278645	78	417564	7278268	89
418340	7278678	93	417586	7278175	25
418386	7278695	89	417421	7278146	74
418439	7278709	94	417345	7278216	93
418511	7278737	96	417131	7278661	54
418557	7278764	95	417063	7278770	80
418586	7278773	84	417007	7278473	47
418714	7278769	59	417271	7278041	92
418667	7278773	80	418157	7279801	81
418619	7278706	84	418046	7279968	91
418577	7278682	86	417952	7279990	85
418509	7278645	64	418025	7279895	38
418439	7278614	75	418063	7279824	92
418315	7278554	96	418177	7279674	45
418478	7278551	95	418185	7279622	84
418624	7278634	80	418102	7279569	92
418657	7278655	74	418070	7279633	76
417735	7278818	94	418018	7279718	81
417770	7278761	67	417987	7279754	78

APPENDIX A: The Ishikawa Index (AI) values (%) in the Izok Lake study area

Easting	Northing	AI (%)	Easting	Northing	AI (%)
417967	7279821	94	417428	7279151	59
417896	7279902	68	417396	7279197	85
417748	7280000	56	417337	7279304	89
417827	7279862	9	417228	7279508	68
417906	7279736	81	417250	7279455	75
417932	7279693	84	417209	7279541	97
417955	7279647	35	417182	7279588	96
417992	7279586	92	417348	7279078	93
418043	7279522	39	417067	7279340	85
417827	7279657	46	417001	7279449	89
417896	7279553	34	416974	7279529	69
417552	7279313	65	416774	7279446	92
417520	7279360	89	416705	7279612	66
417479	7279407	54	416617	7279724	69
417390	7279597	90	416518	7279685	72
417548	7279511	93	416443	7279635	69
417658	7279332	86	416581	7279581	90
417533	7279175	94	416631	7279486	89
417490	7279222	84	416891	7279066	41
417465	7279266	95	416921	7278803	55
417429	7279331	67	416773	7279094	68
417402	7279369	93	416506	7279252	38
417333	7279500	49	416546	7279216	91
417303	7279543	88	416575	7279153	91
417443	7279121	86	416624	7279103	81

APPENDIX A: The Ishikawa Index (AI) values (%) in the Izok Lake study area

Easting	Northing	AI (%)	Easting	Northing	AI (%)
416661	7279027	60	416181	7278879	94
416594	7278983	84	416152	7278934	63
416554	7279057	75	416129	7278989	96
416469	7279171	97	416040	7279100	96
416415	7279245	98	415893	7279322	54
416290	7279281	87	415836	7279247	98
416306	7279228	96	415861	7279202	98
416572	7278797	54	415931	7279101	99
416935	7278156	53	415956	7279033	98
416797	7277998	90	416055	7278891	86
416744	7278145	84	416083	7278844	70
416499	7278556	16	416187	7278676	63
416452	7278625	69	416238	7278589	78
416397	7278723	84	416273	7278533	67
416348	7278801	66	416321	7278453	39
416320	7278843	46	416354	7278395	71
416199	7279015	93	416390	7278338	48
416255	7279098	72	416436	7278264	70
416475	7278754	85	416514	7278155	78
416519	7278682	96	416660	7277905	45
416585	7278351	33	416676	7277840	75
416426	7278479	35	416592	7279731	94
416355	7278590	94	416076	7280179	36
416311	7278667	47	416039	7280238	47
416284	7278720	65	415320	7280064	81

APPENDIX A: The Ishikawa Index (AI) values (%) in the Izok Lake study area

Easting	Northing	AI (%)	Easting	Northing	AI (%)
415423	7279926	33	416292	7282242	66
415474	7279865	69	416325	7282258	82
415500	7279817	52	416387	7282292	89
415637	7279570	70	416304	7282483	46
415684	7279516	80	418225	7280607	75
415883	7279379	97	417087	7279274	68
415837	7279425	92	416910	7279526	95
415806	7279482	97	416862	7279653	97
415766	7279533	98	416740	7279702	89
415725	7279592	92	416409	7279701	86
415664	7279691	92	416379	7279175	95
415652	7279756	67	416636	7279271	72
415614	7279804	68	416659	7279202	88
415585	7279870	74	416535	7279117	76
415563	7279887	73	416344	7279070	79
415449	7280062	67	416362	7278960	21
415951	7280014	79	416376	7278879	49
415960	7279798	81	416455	7278933	82
415640	7280148	57	417588	7279623	96
415732	7280035	92	417501	7279697	56
415789	7279944	65	417141	7279374	76
415977	7279564	90	416854	7278803	58
415930	7279477	92	416781	7278658	32
415924	7279500	97	416546	7278855	50
415596	7280018	69	416359	7282401	54

APPENDIX A: The Ishikawa Index (AI) values (%) in the Izok Lake study area

Easting	Northing	AI (%)	Easting	Northing	AI (%)
416366	7282095	91	411883	7274946	24
416463	7281835	92	411959	7274915	32
417426	7279668	74	412032	7275047	27
417839	7280928	84	412087	7275205	43
417801	7280929	87	412120	7275288	25
417696	7281013	83	412162	7275322	69
410948	7275674	15	412135	7275539	7
410915	7275972	26	412204	7275657	9
411314	7276012	29	412133	7275667	83
411069	7275864	60	412143	7275798	44
410955	7275772	22	412158	7275908	79
411226	7275702	27	412499	7275660	72
411456	7275980	34	412783	7276318	92
411399	7275902	29	412778	7276098	36
411215	7275660	22	412798	7276074	34
411320	7275183	39	412761	7275994	19
411470	7275083	82	412676	7275869	50
411959	7275769	92	412734	7275860	88
412027	7275714	87	413158	7276138	51
412098	7275678	31	413073	7276155	40
412013	7275694	39	413251	7276260	58
411956	7275742	95	413289	7276391	89
411986	7275594	56	413240	7276485	88
411950	7275551	12	413498	7276321	82
411943	7275420	5	413782	7276612	90

APPENDIX A: The Ishikawa Index (AI) values (%) in the Izok Lake study area

Easting	Northing	AI (%)	Easting	Northing	AI (%)
413685	7276641	56	414804	7279753	86
413666	7279919	50	415227	7279939	57
413693	7279937	70	415300	7280457	84
414004	7280265	87	415332	7280466	42
413639	7280163	45	415285	7280863	10
413888	7280372	43	415360	7280967	17
413937	7280505	75	415459	7281115	63
414099	7280972	86	415507	7281065	55
414110	7280794	73	415484	7280972	60
414023	7280667	52	415470	7280857	63
414148	7280831	73	415550	7280576	83
414175	7280790	57	415285	7280819	55
414378	7280738	93	415568	7280438	59
414145	7280665	47	415512	7280404	80
414143	7279839	24	415516	7280218	29
414088	7279697	40	415575	7280139	73
414254	7279654	66	415557	7280075	57
414357	7279680	71	415662	7279988	57
414423	7279734	64	415716	7279983	91
414351	7280502	72	415765	7280056	86
414429	7280496	68	415653	7280394	81
414457	7280560	55	415733	7280464	91
414638	7279749	81	416113	7281045	49
414611	7279699	65	416120	7281078	85
414752	7279739	61	416211	7281053	63

APPENDIX A: The Ishikawa Index (AI) values (%) in the Izok Lake study area

Easting	Northing	AI (%)	Easting	Northing	AI (%)
413900	7278674	94	414474	7279602	42
413903	7278634	89	414647	7279304	78
414087	7279258	53	414778	7279242	76
414105	7279359	81	414786	7279148	69
414062	7278886	84	414895	7279020	87
414069	7278976	83	415026	7279188	72
412508	7278686	50	415094	7279174	77
412515	7278627	24	415026	7279262	83
412586	7278578	87	414958	7279351	76
412655	7278497	38	414865	7279416	69
412685	7278431	68	414608	7279571	80
412755	7278487	93	414708	7279403	37
412782	7278705	60	414981	7279428	30
412940	7278662	73	415033	7279485	55
412982	7278593	38	415123	7279385	88
413097	7278591	52	415223	7279172	55
413114	7278848	52	415310	7279149	66
413195	7278761	79	415280	7279258	70
413506	7279272	77	415259	7279304	55
414245	7278862	50	415257	7279433	34
414262	7278715	85	415261	7279511	32
414638	7278890	95	415147	7279503	73
414614	7278944	97	415187	7279595	74
414507	7279195	59	415317	7279568	49
414390	7279434	71	415371	7279451	56

APPENDIX A: The Ishikawa Index (AI) values (%) in the Izok Lake study area

Easting	Northing	AI (%)	Easting	Northing	AI (%)
415386	7279340	64	415674	7278675	90
415407	7279305	81	415725	7278577	87
415521	7279179	94	415697	7278451	68
415438	7279566	90	415800	7278350	97
415501	7279496	75	415811	7278287	98
415526	7279421	45	415871	7278191	79
415562	7279360	83	415997	7278005	78
415637	7279234	50	416018	7277913	90
415723	7279194	97	416045	7277882	40
415683	7279051	93	416138	7277810	55
415721	7279001	98	416142	7277722	91
415749	7278933	97	416128	7277644	86
415820	7278983	93	416203	7277579	47
415591	7278961	97	416203	7277579	91
415761	7277902	76	416637	7277974	86
416050	7284864	41	416583	7278115	84
415962	7284889	15	416576	7278143	84
415961	7284892	28	416373	7278341	70
416080	7285082	69	416300	7278400	52
415935	7284944	29	416296	7278484	56
415936	7284969	30	416257	7278585	49
415921	7284928	29	416208	7278649	63
415980	7284881	42	416174	7278680	24
416022	7284742	22	416148	7278818	91
415660	7278854	90	416128	7278920	70

APPENDIX A: The Ishikawa Index (AI) values (%) in the Izok Lake study area

Easting	Northing	AI (%)	Easting	Northing	AI (%)
415934	7278946	98	414909	7277630	73
415872	7278990	96	414823	7277596	62
415776	7279073	96	414836	7277646	78
415732	7279204	98	415047	7277344	73
415839	7279430	98	415328	7277246	97
415925	7279507	99	418601	7278473	86
415976	7279559	96	418439	7278526	69
416301	7279285	85	418198	7278122	37
416318	7279214	95	417913	7278203	92
416260	7279080	87	417879	7278376	88
416373	7278990	58	418714	7278679	68
416459	7278892	35	418677	7278601	81
416479	7278776	69	418544	7278718	76
416495	7281712	84	418591	7278874	55
416475	7281792	92	417995	7278623	63
416546	7281799	67	417939	7278550	65
416648	7281751	94	417954	7278530	46
415614	7277939	94	418063	7278413	95
415573	7278036	54	418004	7278392	97
415557	7278060	78	418268	7278646	90
415611	7278124	77	418420	7278690	72
415033	7277402	53	417836	7278774	94
415015	7277432	76	417804	7278675	68
414961	7277421	53	417772	7278851	72
414928	7277595	30	417834	7278831	95

APPENDIX A: The Ishikawa Index (AI) values (%) in the Izok Lake study area

Easting	Northing	AI (%)	Easting	Northing	AI (%)
417651	7278606	32	417918	7279507	47
418127	7279146	82	417740	7279641	43
418241	7279201	70	417902	7279799	49
418235	7279263	97	417797	7279803	72
418274	7279114	82	418215	7280609	86
418308	7279172	76	416596	7279619	86
418258	7279157	89	416531	7279675	68
418341	7279017	89	417312	7281229	93
418400	7279195	52	417308	7281177	88
418591	7279043	74	415579	7280179	85
418523	7279182	77	415656	7280145	4
418490	7279381	97	415759	7280004	82
418507	7279299	95	415766	7280025	90
418491	7279230	55	416682	7279079	86
418363	7279403	90	416928	7278763	90
418379	7279501	97	417179	7278761	32
418252	7279328	78	417494	7279189	4
418161	7279356	95	417500	7279281	95
418168	7279537	88	417932	7279977	65
418139	7279527	46	414890	7278783	98
418070	7279551	64	415600	7278819	86
418157	7279708	93	417562	7278338	74
418076	7279804	91	417969	7279784	78
418063	7279893	68	418039	7279728	52
417935	7279638	91	418020	7279704	73

APPENDIX A: The Ishikawa Index (AI) values (%) in the Izok Lake study area

Easting	Northing	AI (%)	Easting	Northing	AI (%)
418198	7278051	54	412637	7276765	45
417760	7279656	86	413154	7277116	41
418077	7279807	92	412960	7277361	19
411638	7276500	32	412890	7277379	35
411634	7276655	38	412919	7277429	32
411701	7276781	93	412895	7277429	74
411760	7276737	22	412747	7277680	64
411843	7276637	30	412639	7277698	90
411890	7276735	47	413151	7277363	46
412162	7276536	69	413183	7277389	59
411988	7276936	42	413844	7277757	71
411949	7277207	25	414226	7277317	66
411906	7277571	91	414430	7277309	61
411977	7277594	39	414384	7277734	76
412021	7277612	13	414589	7277816	81
412196	7276984	35	414593	7277523	58
412523	7276692	63	414725	7277586	42
412463	7276880	25	414695	7277324	65
412457	7277059	38	414735	7277236	93
412388	7277392	74	414907	7277324	58
412323	7277597	73	415797	7277780	77
412391	7277570	43	414779	7277590	84
412498	7277556	58	414873	7277626	62
412636	7277128	39	414908	7277609	48
412706	7276785	58	414974	7277605	49

APPENDIX A: The Ishikawa Index (AI) values (%) in the Izok Lake study area

Easting	Northing	AI (%)	Easting	Northing	AI (%)
415029	7277398	63	416230	7277666	83
415084	7277473	91	416195	7277704	72
415044	7277336	82	416163	7277799	76
415084	7277295	81	416252	7277895	90
415284	7277284	71	416387	7277744	88
415382	7277811	72	416494	7277632	68
415390	7277731	38	416421	7277886	91
415643	7277620	92	416358	7277981	53
415576	7277724	58	416286	7278104	62
415561	7277811	67	416251	7278206	77
415606	7277936	95	416178	7278268	88
415754	7277884	98	416234	7278323	90
415761	7277835	93	416243	7278387	79
415799	7277784	70	416205	7278529	68
415858	7277717	67	416124	7278648	46
415829	7277680	93	416011	7278709	75
415968	7277568	95	416001	7278530	89
415907	7277827	94	416016	7278474	81
415981	7277770	85	415814	7278847	98
416013	7277717	74	415906	7278859	98
416047	7277667	93	415975	7278898	98
416023	7277626	34	416070	7278927	92
416201	7277571	72	416029	7278814	91
416209	7277476	86	416109	7278402	81
416260	7277619	87	416127	7278340	76

APPENDIX A: The Ishikawa Index (AI) values (%) in the Izok Lake study area

Easting	Northing	AI (%)	Easting	Northing	AI (%)
416082	7278278	54	415521	7278452	77
415993	7278292	73	415567	7278215	58
416113	7278130	65	415667	7278198	82
416207	7278087	61	415797	7278139	72
416108	7278008	64	415784	7277950	71
415912	7277965	37	415564	7277954	75
415918	7278067	79	415551	7278032	81
415828	7278213	86	415427	7278390	92
415859	7278296	92	415270	7278785	98
415836	7278351	75	415231	7278690	97
415881	7278429	55	415268	7278619	94
415789	7278475	76	415314	7278566	79
415772	7278640	88	415259	7278507	85
415743	7278724	87	415348	7278478	91
415726	7278817	98	415368	7278414	54
415660	7278894	92	415463	7277533	95
415593	7278957	97	415507	7277444	66
415457	7278840	96	415447	7277386	78
415391	7278815	98	415279	7277500	64
415369	7278750	98	415254	7277579	51
415537	7278731	98	415140	7278697	96
415525	7278650	97	415204	7278821	97
415478	7278585	97	415138	7278794	98
415651	7278557	95	415004	7278718	96
415555	7278539	96	414934	7278777	97

APPENDIX A: The Ishikawa Index (AI) values (%) in the Izok Lake study area

Easting	Northing	AI (%)	Easting	Northing	AI (%)
414983	7278822	98	414979	7278380	98
415075	7278825	98	415012	7278165	79
415004	7278671	99	414976	7278086	43
415096	7278618	97	414908	7278086	75
415176	7278616	98	414913	7278173	95
415110	7278469	97	414877	7278267	89
415210	7278383	95	414832	7278326	98
415234	7278315	81	414748	7278586	90
415310	7278362	67	414766	7278521	76
415306	7278295	81	414651	7278454	79
415156	7278262	69	414701	7278191	96
415181	7278177	86	414681	7278117	90
415087	7278153	91	414682	7278124	97
415039	7278264	79	414697	7278081	99
415078	7278389	90	414694	7278007	96
415016	7278976	87	414664	7277919	75
415043	7278862	97	414710	7277903	55
414873	7278762	97	414076	7278297	69
414875	7278712	96	414056	7278207	54
414962	7278673	84	414227	7277857	91
414976	7278584	94	416476	7277682	89
414896	7278578	93	417088	7278016	85
414829	7278615	82	416145	7278808	84
414834	7278491	95	416993	7278316	79
414814	7278388	96	416542	7278093	74

APPENDIX A: The Ishikawa Index (AI) values (%) in the Izok Lake study area

Easting	Northing	AI (%)	Easting	Northing	AI (%)
417032	7278716	74	416988	7278318	62
416186	7277489	91	417008	7278345	84
416641	7278241	36	417070	7278441	79
414207	7287414	97	417022	7278315	32
414179	7287421	98	416560	7278807	74
414100	7287455	94	416546	7278867	46
414196	7287400	79	416556	7279074	85
416766	7278206	69	416521	7279056	87
416737	7278177	67	416587	7279025	52
416707	7278270	41	416507	7279004	58
416638	7278247	66	416469	7278829	93
416659	7278180	56	415596	7280219	62
416576	7278166	34	415674	7280191	4
416576	7278145	78	415603	7280144	55
416511	7278163	69	415602	7280016	84
416511	7278165	49	415662	7279990	48
416488	7278258	39	415705	7279989	88
416505	7278334	57	415629	7280327	74
416581	7278347	35	415732	7280039	94
416781	7278660	37	415760	7280054	82
416963	7278643	90	415723	7279916	85
417073	7278618	88	415793	7279935	68
417076	7278555	91	415958	7279807	78
417001	7278474	82	415996	7279871	79
417031	7278482	75	415921	7279508	98

APPENDIX A: The Ishikawa Index (AI) values (%) in the Izok Lake study area

Easting	Northing	AI (%)	Easting	Northing	AI (%)
415859	7279501	97	415489	7279269	66
415758	7279522	98	415522	7279248	89
415842	7279430	99	415523	7279191	86
415880	7279374	94	415547	7279146	98
415890	7279334	71	415664	7279057	96
415877	7279330	96	415883	7278774	99
415570	7279694	91	415739	7278818	97
415633	7279617	52	415649	7278780	98
415625	7279567	86	415757	7278755	97
415681	7279552	80	415536	7278735	98
415773	7279429	67	415524	7278650	97
415643	7279480	86	415605	7278614	85
415538	7279550	69	415822	7279565	99
415596	7279551	75	415936	7279549	97
415665	7279438	93	415999	7279639	55
415578	7279582	36	416026	7279574	98
415559	7279478	86	415979	7279551	97
415572	7279358	79	416357	7279286	49
415772	7279392	94	416304	7279237	84
415797	7279383	99	416335	7279073	78
415789	7279289	93	416162	7279022	84
415858	7279226	98	415997	7278815	96
415750	7279285	86	416083	7278787	76
415749	7279360	92	415970	7279224	97
415648	7279275	89	416042	7279079	97

APPENDIX A: The Ishikawa Index (AI) values (%) in the Izok Lake study area

Easting	Northing	AI (%)	Easting	Northing	AI (%)
415936	7278949	99	416343	7278865	83
415953	7278868	98	415557	7278541	95
415804	7278840	98	415513	7278453	90
415761	7278914	98	415647	7278558	82
415612	7278746	99	415774	7278646	89
415701	7279011	98	415697	7278537	57
415661	7278962	97	415956	7278241	74
416219	7278536	66	415816	7278282	97
416248	7278394	55	415838	7278353	82
416280	7278356	70	415773	7278387	34
416282	7278426	79	415730	7278396	93
416252	7278472	66	415558	7277960	35
416373	7278473	67	415521	7277867	41
416055	7278272	88	417914	7279928	75
416158	7278130	90	417940	7279736	74
416193	7278135	37	417910	7279665	85
416210	7278095	40	417980	7279585	95
415774	7279149	99	417981	7279582	29
415802	7279115	96	418049	7279547	94
415834	7279059	94	418084	7279571	72
415914	7279093	97	418111	7279586	73
415999	7279076	98	418134	7279586	96
416101	7279040	99	418204	7279459	63
416122	7278980	91	418145	7279377	94
416175	7278957	83	418323	7279354	92

APPENDIX A: The Ishikawa Index (AI) values (%) in the Izok Lake study area

Easting	Northing	AI (%)	Easting	Northing	AI (%)
415591	7278961	97	416148	7278818	91
415660	7278854	90	416128	7278920	70
415674	7278675	90	415934	7278946	98
415725	7278577	87	415872	7278990	96
415697	7278451	68	415776	7279073	96
415800	7278350	97	415732	7279204	98
415811	7278287	98	415839	7279430	98
415871	7278191	79	415925	7279507	99
415997	7278005	78	415976	7279559	96
416018	7277913	90	416301	7279285	85
416045	7277882	40	416318	7279214	95
416138	7277810	55	416260	7279080	87
416142	7277722	91	416373	7278990	58
416128	7277644	86	416459	7278892	35
416203	7277579	47	416479	7278776	69
416203	7277579	91	416495	7281712	84
416637	7277974	86	416475	7281792	92
416583	7278115	84	416546	7281799	67
416576	7278143	84	416648	7281751	94
416373	7278341	70	415614	7277939	94
416300	7278400	52	415573	7278036	54
416296	7278484	56	415557	7278060	78
416257	7278585	49	415611	7278124	77
416208	7278649	63	415033	7277402	53
416174	7278680	24	415015	7277432	76

APPENDIX A: The Ishikawa Index (AI) values (%) in the Izok Lake study area

Easting	Northing	AI (%)	Easting	Northing	AI (%)
414961	7277421	53	417772	7278851	72
414928	7277595	30	417834	7278831	95
414909	7277630	73	417651	7278606	32
414823	7277596	62	418127	7279146	82
414836	7277646	78	418241	7279201	70
415047	7277344	73	418235	7279263	97
415328	7277246	97	418274	7279114	82
418601	7278473	86	418308	7279172	76
418439	7278526	69	418258	7279157	89
418198	7278122	37	418341	7279017	89
417913	7278203	92	418400	7279195	52
417879	7278376	88	418591	7279043	74
418714	7278679	68	418523	7279182	77
418677	7278601	81	418490	7279381	97
418544	7278718	76	418507	7279299	95
418591	7278874	55	418491	7279230	55
417995	7278623	63	418363	7279403	90
417939	7278550	65	418379	7279501	97
417954	7278530	46	418252	7279328	78
418063	7278413	95	418161	7279356	95
418004	7278392	97	418168	7279537	88
418268	7278646	90	418139	7279527	46
418420	7278690	72	418070	7279551	64
417836	7278774	94	418157	7279708	93
417804	7278675	68	418076	7279804	91

APPENDIX A: The Ishikawa Index (AI) values (%) in the Izok Lake study area

Easting	Northing	AI (%)	Easting	Northing	AI (%)
418063	7279893	68	416943	7278152	84
417935	7279638	91	416638	7278247	62
417918	7279507	47	417916	7279805	89
417740	7279641	43	417992	7279673	87
417902	7279799	49	417429	7279259	88
417797	7279803	72	417433	7279336	92
417615	7278268	69	417388	7279205	88
417645	7278217	34	417326	7279326	16
417538	7278251	87	417399	7279374	90
417521	7278153	60	417387	7279382	46
417532	7278230	50	417437	7279413	82
417564	7278272	35	417295	7279561	92
417449	7278254	71	417245	7279522	87
417363	7278012	93	417253	7279571	97
417362	7278004	90	417209	7279542	91
417281	7278043	92	417169	7279518	97
416799	7277994	85	417166	7279535	97
416778	7277989	91	416461	7279641	89
416676	7277908	40	416442	7279628	84
416640	7277971	91	416585	7279716	86
416619	7278025	30	416626	7279492	22
416542	7278093	78	416676	7279609	95
416586	7278107	51	416665	7279215	79
416746	7278151	54	416775	7279087	81
416799	7278158	91	416775	7279087	53

APPENDIX A: The Ishikawa Index (AI) values (%) in the Izok Lake study area

Easting	Northing	AI (%)	Easting	Northing	AI (%)
416723	7279114	80	417128	7279378	83
416662	7279033	59	417115	7279589	96
416622	7279110	66	417186	7279589	95
416578	7279039	76	417079	7279632	92
416568	7279159	85	416852	7279650	92
416623	7279255	76	416999	7279459	88
417029	7278714	70	416936	7279456	96
417058	7278782	75	416901	7279467	95
416858	7278811	73	416959	7279489	90
416901	7278798	88	416776	7279455	98
416946	7278744	72	417244	7278943	52
417011	7278747	88	417264	7278977	90
417044	7278807	34	417313	7278952	94
417983	7279835	83	417364	7278963	91
417429	7279177	30	417125	7278716	83
417486	7279172	89	417738	7278836	88
417420	7279149	89	416460	7279242	98
417435	7279114	40	416472	7279212	97
417259	7279120	32	416522	7279166	83
417330	7279075	87	416364	7278880	89
417082	7279269	82	416126	7278621	36
417471	7279394	53	416085	7278641	33
417370	7279505	95	418012	7279708	89
417337	7279541	86	418036	7279730	67
417153	7279486	88	418159	7279622	95

APPENDIX A: The Ishikawa Index (AI) values (%) in the Izok Lake study area

Easting	Northing	AI (%)	Easting	Northing	AI (%)
418181	7279561	51	417296	7279117	94
418207	7279526	96	417411	7278269	78
418264	7279469	97	416414	7277764	84
418325	7279419	94	418215	7280609	86
418440	7279442	87	416596	7279619	86
418428	7279304	78	416531	7279675	68
418334	7279076	59	417312	7281229	93
418289	7279403	80	417308	7281177	88
417713	7278757	93	415579	7280179	85
417426	7278562	64	415656	7280145	4
417611	7278512	81	415759	7280004	82
417687	7278456	96	415766	7280025	90
417577	7278391	95	416682	7279079	86
417312	7278248	96	416928	7278763	90
417009	7277806	33	417179	7278761	32
417021	7277831	84	417494	7279189	4
417090	7278015	81	417500	7279281	95
417083	7277812	84	417932	7279977	65
417052	7277993	55	414890	7278783	98
417009	7277977	78	417562	7278338	74
416852	7277787	36	417969	7279784	78
416642	7277758	34	418039	7279728	52
416839	7277781	37	418020	7279704	73
416550	7277726	83	418198	7278051	54
416472	7277680	70	417760	7279656	86

APPENDIX A: The Ishikawa Index (AI) values (%) in the Izok Lake study area

Easting	Northing	AI (%)	Easting	Northing	AI (%)
418077	7279807	92	416480	7278643	35
416392	7277935	82	416494	7278651	96
416386	7277872	86	416426	7278585	91
416232	7277893	73	416292	7278661	35
416395	7277997	27	416394	7278702	85
416326	7277958	64	416034	7280193	76
416235	7277775	95	416016	7280248	83
416148	7277727	96	415951	7280099	88
416165	7277799	64	415950	7280015	91
416156	7277905	73	415780	7280076	85
416448	7278286	76	415611	7279809	86
416436	7278192	71	415532	7279904	41
416417	7278113	51	415480	7279836	83
416688	7278594	75	415519	7279798	63
416704	7278474	93	415686	7279805	60
416680	7278407	55	415643	7279860	96
416541	7278531	68			
416616	7278520	39			
416611	7278553	39			
416584	7278424	88			
416500	7278479	47			
416470	7278561	7			
416466	7278354	52			
416393	7278349	73			
416448	7278437	69			

Easting and northing in UTM, NAD 83 12N.